Temperature and Pressure Induced Lattice Dynamics in Endohedral and Exohedral Fullerenes

A Thesis Submitted

To

Sikkim University

In Partial Fulfillment of the Requirement for the
Degree of Doctor of Philosophy in Physics

By

Trisha Mondal
Department of Physics
School of Physical Sciences
Sikkim University
July 2019

Dedication

To my parents
Mr. Sudeb Mondal
Mrs. Rita Mondal
for their pragmatic support, encouragement and inspiration.

To my beloved brother
Mr. Anish Mondal
for his love, encouragement and trust.

Acknowledgement

First of all, I would like to express my gratitude to my supervisor, Dr. Archana Tiwari for her invaluable guidance, her patience and constant support throughout my Ph.D course.

I would like to sincerely and wholeheartedly thank Dr. Amitabha Bhattacharyya, Associate Professor, for his constant support and valuable discussions. Sincere thanks to Dr. Dhurba Rai for his excellent assistance in performing DFT calculations. The faculty members, Professor A. K. Pathak, Dr. Subir Mukhopadhyaya, Dr. Ajay Tripathi and Dr. Hemam Dinesh Singh for their valuable discussion and insightful comments during this work, so my heartfelt gratitude to all of them.

I thankfully acknowledge the laboratory, workshop facilities and the financial support provied by UGC-DAE Indore for my work.

I would like to acknowledge our project collaborator, Nagoya University, Japan for the preparation and purification of sample.

I am deeply obliged to Professor T. Shreepathi, UGC-DAE-CSR Indore, for his courteous assistance, valuable discussion and insightful comments in performing experiments in Indore. I would like to aknowledge Dr. V. Sathe, UGC-DAE-CSR Indore, for granting permission to perform the temperature dependent Raman spectroscopy experiments in his laboratory.

I would like to acknowledge HoD of Geology, Dr. Rakesh Kumar Ranjan for granting permission to use the Leica microscope for loading sample in DAC. I thankfully acknowledge the HoD of Horticulture, Dr. Laxuman Sharma, for granting permission to perform UV-Vis experiments in his Department. I wish to acknowledge the Department Of Microbiology for accessing the sonicator for sample preparation.

I would like to thank the laboratory assistants of the Department of Physics, Mr. Bikram Thapa, Department of Chemistry, Mr. Binod Chettri, Department of Geology Mr. Bhanu Mangar and Department of Microbiology, Mrs. Radha Basnett for their help.

I am indebted to Mr. Sayak Das for his constant help, support and encouragement.

I wish to acknowledge Mr. Prajwal Chettri for his assistance in laboratory. I would like to express my thanks to Mrs. Ambika Pradhan and Ms. Laden Sherpa for their encouragement, support in all the moments of ups and downs. I am thankful to Mr. Rajesh Rawat, Mr. Yam Prasad Rai and Mr. Umesh Dhakal for their help, support and encouragement. I am also thankful to all my friends for their support all along the work.

Last but not the least, I pay my special gratitude to my parents, my brother and sister for their ceaseless love and perpetual encouragement.

Many remain unthanked by name, a heartfelt gratitude to all those who have helped me during this years.

Trisha Mondal
July 2019

Abstract

Fullerene and its derivatives are potential candidates for thermoelectric applications due to their low thermal conductivity. This work proposes to utilize the concept of phonon lattice vibrations of doped fullerenes and fullerene oxides under thermal and mechanical stress that qualitatively alters the heat conduction and the thermoelectric figure-of-merit.

This work presents temperature, laser power and pressure dependent Raman spectral analysis of endohedral metallofulleres (M@C_{82}, M=Gd,Dy) and fullerene oxides ($C_{60}O$, $C_{70}O$) to understand their lattice dynamics and thermodynamic stability. The first order temperature and laser power coefficients of Raman frequencies are evaluated and are utilized to evaluate room and high temperature thermal conductivity. Thermal conductivity of fullerene oxides are smaller the that of M@ C_{82}. Blue-shifts in the Raman frequencies while decreasing the temperature in metal-cage, C-O and cage internal vibrations of endohedral and exohedral describe thermal contraction in the molecules. Temperature independent linewidth of cage internal vibrations shows minimal anharmonic interaction; whereas, strong temperature dependence metal-cage vibration linewidths are governed by phonon-phonon and electron-phonon coupling.

The density functional measurement has been performed to examine contraction in the C–O bond length of $C_{60}O$. C-O bond contraction has been corroborated with the experimental Raman shifts at different temperatures and pressures to evaluate the linear expansion coefficient and linear compressibility of $C_{60}O$. Isobaric mode and isothermal mode Grüneisen parameter are used to explain the thermodynamic stability of $C_{60}O$ at low temperature and high pressure. The correlation between Grüneisen parameter and thermal conductivity provides an insight into pressure induced thermal conductance which in turn may affects their thermoelectric efficiency.

List of Publications

- Mondal, T., Tripathi, A., Zhang, J., Sathe, V., Shripathi, T., Shinohara, H. and Tiwari, A. (2015) Temperature-Dependent Raman Study of Gd@C82, *Journal of Physical Chemistry C*, 119, 1269812702

- Mondal, T., Tripathi, A., Zhang, J., Shripathi, T., Shinohara, H. and Tiwari, A. (2017) Thermal conductivity of M@C82 [M= Gd, Dy] thin films *Journal of Physical Chemistry C*, 121, 3642-3647.

- Mondal, T., Tripathi, A., Zhang, J., Shripathi, T., Shinohara, H. and Tiwari, A. (2018) Temperature and pressure induced Raman studies of C60 oxide *Journal of Applied Physics*, 124, 195105.

This document was typeset in LaTeX software.

Graphs were generated using OriginLab software version 8.1.

Contents

List of Figures

List of Tables

Abbreviations

- TE: Thermoelectric Efficiency
- TC: Thermal Conductivity
- EMF: Endohedral Metallofullerene
- HOMO: Highest Occupied Molecular Orbital
- LUMO: Lowest Unoccupied Molecular Orbital
- HCP: Hexagonal Close Packed
- SC: Simple Cubic
- FCC: Face Centered Cubic
- HPLC: High Performance Liquid Chromatography
- UV-vis: UV-Visible Spectroscopy
- DAC: Diamond Anvil Cell
- PTM: Pressure Transmitting Medium

List of symbol

- ZT Figure of merit
- S Seebeck coefficient
- σ Electrical conductivity
- κ Thermal conductivity
- γ_{iT} isothermal mode Grüneisen parameter
- γ_{iP} isobaric mode Grüneisen parameter
- B_T Bulk modulus
- K_a Linear compressibility
- α_T Linear thermal expansion coefficient
- ν Frequency
- λ Wavelength
- Γ Linewidth
- k Force constant
- T Temperature
- L Laser power
- P Pressure
- χ_T Temperature coefficient
- χ_L Power coefficient
- χ_P Pressure coefficient

- d_0 $1/e^2$ beam width
- t Sample thickness
- M_s Saturation magnetization
- J Total angular momentum
- $B_J(x)$ Brillouin function
- M Magnetization
- χ Magnetic susceptibility
- H Magnetic field
- μ Magnetic moment
- μ_B Bohr magnetron

Part I

INTRODUCTION

Chapter 1

Introduction

Modern technology has offered conveniences relying on electricity where increase in energy generation and consumption reduction are perhaps one of the major challenges. The ability to improve efficiency of power consumption and management is of vital need. Thermoelectric (TE) materials have grabbed attention due to their potential applications in electronic cooling and waste heat harvesting. Thermoelectric material converts thermal energy into electricity. The performance of thermoelectric material is determined by the dimensionless figure of merit ZT, which is related to Seebeck coefficient S, electrical conductivity, σ and thermal conductivity, κ [9, 10]:

$$ZT = S^2\sigma T/\kappa \tag{1.1}$$

The Seebeck coefficient(S) is the measure of thermal diffusivity carried by electrons due to thermal gradient. Temperature difference between two dissimilar electrical conductors or semiconductors connected together at two junctions induce Seebeck voltage(V). This voltage is related to the difference in temperature (ΔT) between the heated junctions and the Seebeck coefficient(S). S is determined by the scattering rate and the density of the conduction electrons. The schematic diagram of Seebeck effect is shown in Figure 1.1 Electrical

conductivity(σ) is a measure of the rate at which an electric current can pass through a material. Large Seebeck coefficient leads to improved thermoelectric performance. In addition, large electrical conductivity(σ) helps to improve ZT by increasing electron mobility and offers less resistance for the flow path of electrons. Low thermal conductivity can be attributed to an increase in the phonon scattering that leads to higher temperature gradient and hence improved ZT.

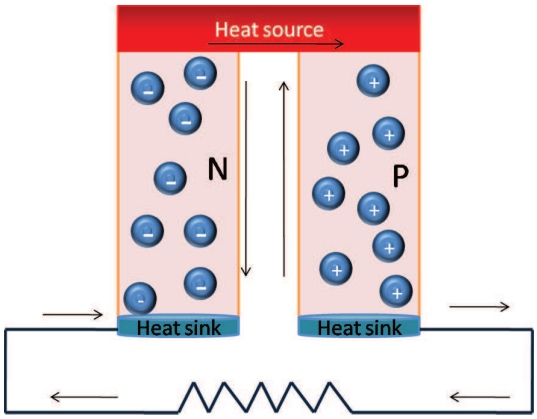

Figure 1.1: Illustration of Seebeck effect.

Designing efficient thermoelectric materials requires tuning between electronic transport which is determined by power factor($S^2\sigma$) and thermal transport which is determined by thermal conductivity (κ). The way to optimize TE materials are to increase the power factor and to reduce the lattice thermal conductivity. To reduce κ, phonon scattering is increased by incorporating random defects or impurities into the material. This also leads to an increase in electron scattering which compromises with carrier mobility and hence, electrical conductivity reduces. σ can be increased by increasing carrier concentration. However, presence of more electrons saturates the material which reduces electron diffusion rate and hence, hinders S. As a result, power factor falls down rapidly. Thus, The quantities S, σ and κ are interlinked in such a way that it is very difficult to control these variables independently and improve ZT. To overcome this conflict, Hicks and Dresselhaus suggested that S, σ and κ can be controlled independently to improve figure of merit by using low dimensional

materials[11]. The incorporation of lower-dimensional structures enhances electronic density of state (DOS) near Fermi level via quantum confinement [12, 13]. As a result, asymmetry in electron transport is increased that attributes to a large average transport energy and a large number of carriers moving in the material. This leads to enhancement of Seebeck coefficient and reduction in thermal conductivity. It is found that incorporating nanostructures embedded in bulk material scatter phonons more effectively than electrons which attracted interest in reducing the TC without compromising electrical conductivity to improve ZT [14].

Previous reports have illustrated that introducing nano-scale dopant into the composite is a widely used method to reduce the thermal conductivity further [15, 16, 17]. When nanoparticles are dispersed homogeneously within the grains, significant decrease in lattice thermal conductivity is observed with negligible degradation in the electrical conductivity. In recent studies, C_{60} fullerenes and its derivatives have grabbed attention to enhance ZT of thermoelectric composites [16, 17, 15, 18]. Having ultrahigh elastic molecule, C_{60} offers an effective phonon scattering which reduces the lattice thermal conductivity [17]. To understand the role of C_{60} in thermoelectric composites, a comprehensive understanding of thermal transport property of C_{60} is needed.

Lattice thermal conductivity depends on phonon group velocity (v_g) and phonon relaxation time (τ), which are strongly connected to the dispersion of phonons [19]. Having low velocities, optical phonons have negligible contribution to lattice thermal conductivity. In large primitive cells, population of acoustic phonons are reduced which is the dominant factor in thermal conductivity [19]. However, heat transport property in low-dimension structures may differ significantly from that in the bulk structure. When structure dimensions are similar to the phonon mean free path, classical laws are no longer valid. In nanostructure, the phonon dispersion relation could be significantly modified

due to confinement.

FCC C_{60} crystal consists of 60 carbon atoms and there are 180 branches of dispersion curves [1]. Figure 1.2 shows the phonon dispersion curves of FCC C_{60} where 6 inter-molecular phonon (acoustic) branches and 174 intra-molecular phonon (optical) branches are present. The frequency-dependent distribution of phonon modes can be described by Vibrational Density of state(VDOS). VDOS are occupied by modes that arise due to intermolecular vibrations, and intra-molecular vibrations. The VDOS of C_{60} in the low frequency regime is dominated by the inter-molecular interaction. The intermolecular VDOS shows strong features around 2.3 and 3.7 meV. Vibrational frequencies of C_{60} below 3 THz posses higher group velocities as compared to high frequency intra-molecular phonons. Therefore, thermal conductivity is associated with phonon frequencies lower than 3 THz. Less population of long wavelength phonon in VDOS results in low to ultralow thermal conductivity (0.4-0.075 W $m^{-1}K^{-1}$) of C_{60} and its derivatives. [1, 20].

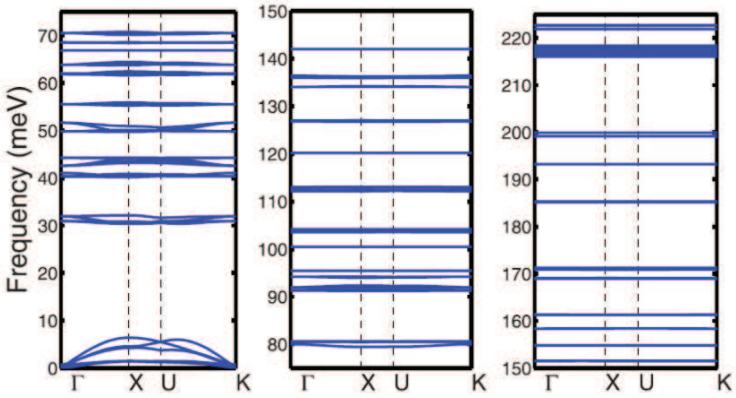

Figure 1.2: Lattice dynamics calculations of phonon dispersion curves of FCC C_{60}.(reprinted from Ref [1])

Possessing high Seebeck coefficients and low thermal conductivities, fullerene molecules have the potential to enhance the figure of merit [10, 21].

As most thermoelectric materials are imperiled to high temperatures due to

their applications, long-term constancy in performance is desired. Under thermal and mechanical stress, change in inter-molecular and intra-molecular bond vibration of the crystal may modify their phonon velocities and density of states; hence heat conduction and thermoelectric efficiency are expected to be altered. This thesis aims to find potential material for thermoelectric applications under extreme conditions. The prime goal is to examine the effects of thermal and mechanical stress on the heat conduction properties of doped fullerenes. The main objectives of this thesis are as follows:

- Temperature effect on lattice dynamics of Gd@C_{82}, Dy@C_{82},C_{60}O and C_{70}O: To understand the effect of temperature in lattice dynamics, temperature dependent Raman line shifts and linewidth variation were analyzed. Temperature dependent force constants of metal-cage(for Gd@C_{82}, Dy@C_{82}) and Oxygen-cage(C_{60}O and C_{70}O) vibrations were evaluated. Temperature coefficients and Grüneisen parameters were determined for different Raman vibration modes.

- Determination of thermal conductivity of Gd@C_{82}, Dy@C_{82},C_{60}O and C_{70}O: Raman thermometry method was used to determine thermal conductivity where both temperature and laser-power dependent Raman studies were performed.

- Pressure effect on lattice dynamics: To understand effect of mechanical stress in lattice dynamics, pressure coefficients and Grüneisen parameters were determined for different Raman vibration modes. From the study, an overview of thermoelastice property such as linear compressibility and thermal expansion coefficient of material was obtained.

1.1 Outline of the Thesis

The work presented in this thesis delivers a pathway for the use of doped fullerenes as a dopant in thermoelectric composites by studying their thermal conductivity to improve figure of merit. In this work, thermal conductivity was determined using spectroscopic investigation. Optical and vibrational properties of endohedral fullerenes and fullerene oxides have been examined under low temperature and high pressure. The thesis is structured as follows:

Chapter 2 includes a review of endohedral metallofullerenes (EMFs) and fullerene oxides. This section is focused on the electronic structure, lattice dynamics and thermodynamic properties including thermal conductivity of the materials. In addition, this section also explains how temperature and pressure can affect thermal conductivity.

Chapter 3 provides the details of the materials used to study in this research work and experimental techniques used to achieve the objectives. This chapter includes details of the synthesis and characterization of materials which are studied. Raman spectroscopic technique was used with a cooling setup to observe the thermal effects on Raman spectra. Diamond anvil cell (DAC) was used to generate high pressure.

Chapter 4 describes the temperature effect on lattice vibration of two EMFs, $Gd@C_{82}$ and $Dy@C_{82}$ film. In this section magnetometry study of these materials is discussed by using the Brillouin function approach and temperature dependent oxidation states are examined by estimating temperature dependent total angular momentum (J). It corroborates with the temperature and power dependent Raman spectra. On the basis of these results, the spectroscopic investigation of TC is examined at the end of this chapter.

Chapter 5 describes the temperature effect on magnetic and vibrational property of two fullerenes oxides, $C_{60}O$ and $C_{70}O$. Temperature and power dependent Raman spectra are analyzed to understand lattice dynamics and to

estimate TC of these two materials. In addition, DFT calculation is performed on optimized $C_{60}O$ molecule to understand thermal effect on C–O bond and to estimate thermal expansion coefficient. Grüneisen parameter are evaluated from the temperature dependent Raman shifts.

In Chapter 6, the effect of pressure on vibrational property of $C_{60}O$ is decribed along with pressure dependent Raman measurements. Mode dependent Grüneisen parameter is evaluated. Linear compressibility is also examined from the pressure induced bond contraction. This section highlights the contribution of mechanical stress of $C_{60}O$ cluster in its thermal conductivity and hence its thermoelectric properties.

In chapter 7, the work of the thesis is concluded and the potential opportunities for further work are presented.

Chapter 2

Literature review

In search of potential material for thermoelectric applications, this work is focused on the investigation of thermal conductivity of doped fullerenes under extreme condition(low temperature, high pressure). In this chapter,we introduce the fullerene and its derivatives which are associated with this work. Reviews comprising of various studies on the structural, optical and magnetic properties of endohedral metallofullerenes (EMFs) and fullerene oxides are included. This section also explains how temperature and pressure can affect the lattice dynamics and heat conduction properties of the materials.

2.1 Fullerene

Fullerene consists of carbon atoms connected by bonds to form a hollow cage like structure. Fullerenes were discovered experimentally for the first time in September 1985 by a group of scientists including Robert F. Curl Jr., Harold W. Kroto and Richard E. Smalley with co-workers [22]. The shape of the fullerene depends on the number of carbon atoms present in the molecule. Euler's theorem suggests that each fullerene C_n consists of 12 pentagonal rings and m hexagonal rings where m=(C_n-20)/2 [23]. C_{60} is the most abundant fullerene that have buckyball shape. C_{60} is formed by 12 pentagonal and 20

hexagonal rings of carbon atoms. C–C bond belonging to pentagons are single bonds, and the bonds attached between two hexagons are double bonds. All the pentagons are surrounded and isolated by the hexagons and that makes C_{60} most stable [24, 25]. Within a fullerene molecule, carbon bonds are sp^2 and sp^3 hybridized. The distortion of the bonding character in the direction of sp^3 type hybridization is responsible for the curvature of the fullerene surface. C_{70}

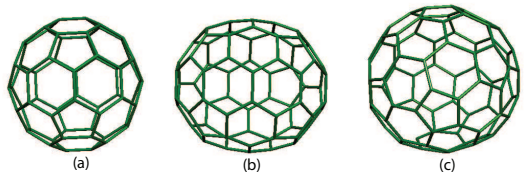

Figure 2.1: Structure of (a)$C_{60}(I_h)$, (b)$C_{70}(D_{5h})$ and (c)$C_{82}(C_2)$

is the second abundant fullerene. The structure of fullerene C_{70} consists of 12 pentagons and 25 hexagons of carbon atoms. The presence of extra 5 hexagons elongated the buckyball shape into a rugby ball in shape. A higher fullerene, C_{82} consists of 12 pentagons and 31 hexagons. The structures of C_{60}, C_{70} and C_{82} are shown in Figure 2.1. Due to the reduced symmetry and elongated form, physical properties of C_{70} and C_{82} are different from the properties of C_{60} [26].

2.1.1 Structural and electronic properties

Structural studies of crystalline C_{60} show that under ambient conditions the crystal has a face-centered cubic (FCC) configuration of C_{60} spheres with lattice parameter a_0=14.2 $\mathring{A}$[27, 28, 29]. The lattice structure of the C_{60} molecule is shown in Figure 2.2. The most stable crystal faces are the close-packed (111) and (100) planes. In normal condition, C_{60} clusters are freely rotating. Upon lowering the temperature, application of hydrostatic pressure or intercalation, the free rotation of fullerene molecules is hindered. Below 260 K, two rotational degrees of freedom freeze and the molecules can only rotate about fixed direction. Therefore, below 260 K C_{60} crystals experience a phase transition

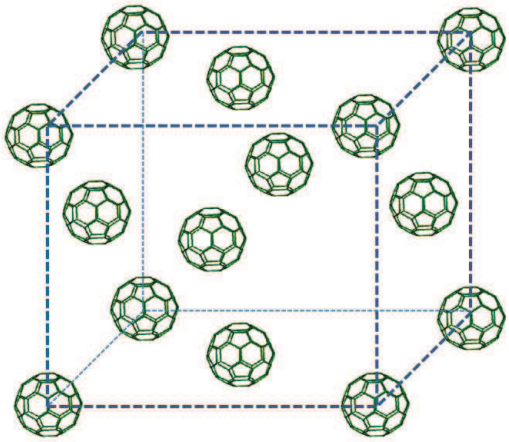

Figure 2.2: Schematic representation of FCC arrangement of C_{60} molecule at ambient condition.

from FCC to a simple cubic (SC) lattice [29]. Below 90K, SC structure transits to a glassy state where all the orientational rotations are frozen [30]. When fullerenes are subjected to high pressure at high temperature, intermolecular bonds are formed which follows the creation of fullerene dimers, chains, planes, or three-dimensional structures [31].

At ambient condition, C_{70} molecules are arranged in an isotropic FCC structure with an inter-molecular distance of 10.51 $\mathring{A}$. Fleming *et al.* suggested that solvent free C_{70} has FCC structure with a small amount of a hexagonal close-packed (HCP) lattice structure at room temperature [32]. Upon lowering temperature the free rotation hinders but rotation around the long axis of the molecules persists. During cooling orientational freezing takes place in two stages. Between 295 and 345 K, the lattice experiences a rhombohedral (RH) distortion. Below 295 K, the RH lattice undergoes a further transformation into the monoclinic structure [33]. At 1.2 GPa FCC-to-RH phase transition has been observed from pressure dependent X-ray diffraction pattern that persists up to 6 GPa [34, 35]. X-ray diffraction showed that solvent free C_{82} structure prepared by sublimation have FCC structure whereas the crystal grown in toluene and CS_2 has monoclinic and cubic structure [36, 37].

According to Frontier orbital theory, the highest occupied molecular orbital

(HOMO) and the lowest unoccupied molecular orbital (LUMO) play an important role in reactivity of fullerenes. The HOMO-LUMO gap represents the chemical hardness of the molecule [38]. The high electron affinity in fullerenes due to the presence of low lying LUMO orbital makes them reactive. With the increase in the molecular size, HOMO-LUMO energy gap decreases. When HOMO-LUMO gap is small, it is energetically favorable to add electrons to a stabilized LUMO, and/or to extract electrons from a destabilized HOMO [39]. As a result, higher fullerenes are found to be more chemically reactive [40, 41]. Possible reactions of C_{60} and C_{70} includes [23]:

- addition
- polymerization
- nucleophilic/electrophilic substitution
- intercalation/doping

In doping reaction, transition metal of rare earth metals are doped inside the fullerene cage. Being a cage-like structure, the fullerene molecule has an internal hollow space that allows encapsulating one or more atoms inside the molecules. These molecules are called as endohedral fullerenes. In the later section, details of endohedral fullerenes are reviewed.

In addition reaction, functionalization of fullerenes are formed where molecules or functional groups are attached with the fullerene cage. Such kind of fullerenes are known as exohedral fullerene. This work focuses on fullerene oxides which is a kind of exohedral fullerene. In the later section, the formation of fullerene oxides and their properties are discussed.

2.2 Fullerene oxide

Because of electron affinity, fullerene C_{60} and C_{70} readily react with atmospheric oxygen and forms oxides($C_{60}O_n$,$C_{70}O_n$ where n=1,2,3). Fullerene oxide $C_{60}O$ is among the first fullerene derivatives reported where the oxygen atom is attached to the exterior of the cage [42]. In subsequent investigations, C_{60} and C_{70} were synthesized by photo-oxygenation, ozonization and ultrasonification and then the structural assignments were obtained through the interpretation of UV-vis and ^{13}C and ^{3}He NMR spectra [42, 43, 44, 45]. Heymann provided a thorough review of fullerene oxides and ozonides where structures, stabilities, and the formation of $C_{60}O$ and $C_{70}O$ were explained[46]. The photo-induced oxidation process in fullerene is initialized by excitation of electrons beyond its HOMO-LUMO gap. In C_{60}, the HOMO-LUMO gap is about 1.5-1.7 eV; whereas, in C_{70}, HOMO-LUMO gap is 1.76 eV [47]. An incoming photon with energy 1.8 eV, stimulate an electron from the ground state ($^1C_{60}$) to the first excited state ($^1C_{60}$*). This transition is due to internal conversion(IC) and inter-system crossing (ISC) to form a triplet excited state that decays in the presence of oxygen molecules. The presence of triplet excited state C_{60} and singlet oxygen produces fullerene oxide via triplet energy transfer(TET) [2, 45]. Figure 2.3 shows Energy level diagram for C_{60} oxidation mechanism. Raghavachari reported Semi-empirical ab initio calculations on stable structure of $C_{70}O$ where oxygen is bridging an equatorial C-C bond[48].

There are two stable oxygen containing fullerene isomers:

1. epoxy like structure (with a single C–C bond) where oxygen is bridging over a [6,6] bond

2. annulene like structure (with a broken C–C bond) where oxygen is bridging over a [6,5] bond

The structure of C_{60} epoxide and oxidoannulene are shown in Figure 2.4. The

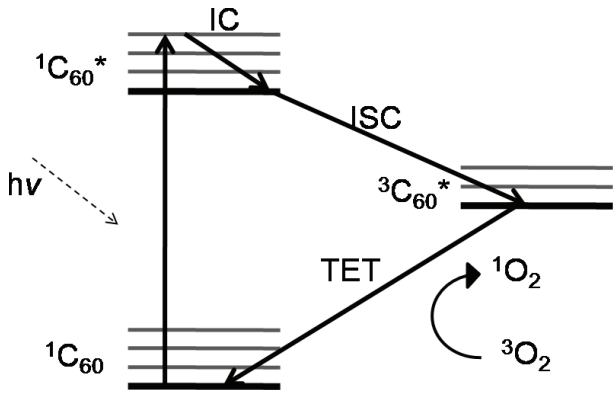

Figure 2.3: Energy level diagram illustrating the mechanism for C_{60} oxidation (adapted from Ref. [2]).

theoretical calculations suggests that oxidoannulene is more stable than epoxide [49]. However, the experimental findings does not agree with the theoretical studies and indicate that epoxides are more stable [45]. C_{60} and C_{70} isomers

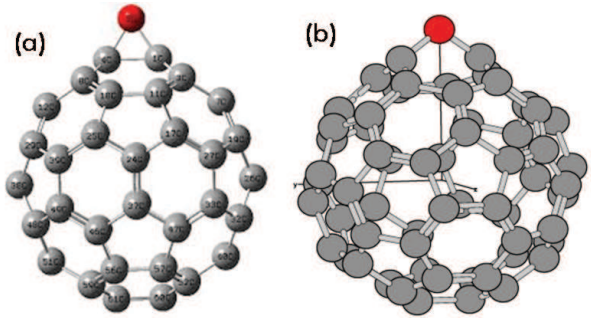

Figure 2.4: Structure of C_{60} isomers (a) epoxide and (b) oxidoannulene.

have I_h and D_{5h} symmetry respectively. $C_{60}O$ with the oxygen atom bridging the carbon atoms common to two hexagonal rings belongs to the C_{2v} point group [5, 50]. Stable structure of $C_{70}O$ with the oxygen bridging over [6,6] bond has C_{2v} symmetry[48].

2.2.1 Optical and magnetic properties

Raman and UV-vis spectra of $C_{60}O$ contain a number of unique features that explain its optical and vibrational character. The UV-vis absorption for $C_{60}O$ in toluene are quite similar to C_{60} except for a slight difference in the 400-

700 nm region. Absorption band at 408 nm of pristine C_{60} is absent in $C_{60}O$ and a new band at 424 nm is observed which is the signature band of epoxide $C_{60}O$ [42]. In comparison to C_{60}, $C_{60}O$ has stronger absorption at 496 nm and weaker absorptions at 540 and 600 nm. In pristine C_{70}, absorption bands are reported at 382.7 nm, 472.6 nm, 550 nm and 640 nm. Unlike $C_{60}O$, no new band is reported in the absorption spectra of all $C_{70}O$ isomers. Only the existing bands of C_{70} in the region 400-700 nm is observed to be shifted and broadened in $C_{70}O$[51].

Vibrational frequencies of a molecule are associated with its structure and symmetry. Normal vibrations of C_{60} with corresponding symmetries are expressed as:

$$\Omega = 2A_g + 3F_{1g} + 4F_{2g} + 6G_g + 8H_g + A_u + 4F_{1u} + 5F_{2u} + 6G_u + 7H_u \quad (2.1)$$

There are ten Raman active modes ($2A_g + 8H_g$) and four F_{1u} infrared active modes. Three significant vibrational modes are $H_g(1)$, $A_g(1)$ and $A_g(2)$. $H_g(1)$ mode is "cage squashing mode" where the molecule is deformed into a rugby ball shape and back to the spherical form. It is a low frequency mode and possible five-fold degeneracy of $H_g(1)$ mode can be observed due to perturbation. The $A_g(1)$ mode is known as "radial breathing" mode that describes expanding and contracting of the whole cage. The $A_g(2)$ mode is "pentagonal pinch" mode which is caused by contracting and extending all the double bonds on the C_{60} [52].

In comparison to C_{60}, vibrational assignments of C_{70} cluster is more complicated. The free C_{70} cluster belongs to the D_{5h} symmetry group and the 204 normal vibrations classify as [53]:

$$\Omega = 12A_1' + 9A_2' + 21E_1' + 22E_2' + 9A_1'' + 10A_2'' + 19E_1'' + 20E_2'' \quad (2.2)$$

The E_1' and A_2' modes are infrared active whereas the A_1', E_2' and E_1'' are Raman active. The $'$ vibrations indicate symmetric and the $''$ vibrations indicate antisymmetric with respect to the equatorial symmetry plane. Schettino *et al.* correlated the vibrations of C_{70} with C_{60} where $A_g \leftrightarrow A_1'$ and $H_g \leftrightarrow A_1'+E_1'+E_1''$ [53]. With the increase of molecular size, symmetry is reduced that results in the increased number of vibrational frequencies.

When oxygen atom is attached to fullerenes, vibrational symmetry is reduced and degeneracy in vibrational frequencies is removed. Vibrational modes of $C_{60}O$ can be explained by the removal of degeneracy and the vibrational coupling between the C_{60} cages [54]. Both experimental and theoretical calculation showed an increase number of Raman peaks in C_{60} oxide [48, 54]. The correlation between the symmetry of the normal modes in C_{60} and $C_{60}O$ is reported in Table 2.1.

Table 2.1: Normal vibrations in C_{60} and $C_{60}0$ [5]

C_{60}	$C_{60}O$
A_g	A_1
T_{1g}	A_2,B_1,B_2
T_{2g}	A_2,B_1,B_2
G_g	A_1,A_2,B_1,B_2
H_g	$2A_1$,A_2,B_1,B_2
A_u	A_2
T_{1u}	A_1,B_1,B_2
T_{2u}	A_1,B_1,B_2
G_u	A_1,A_2,B_1,B_2
H_u	A_1,$2A_2$,B_1,B_2

Raman study of C_{60} reported $H_g(1)$, $A_g(1)$ and $A_g(2)$ peaks at 270 cm^{-1}, 493 cm^{-1} and 1467 cm^{-1} [52, 55]. Krause *et. al.* predicted the vibrational spectra of $C_{60}O$, $C_{120}O$ and $C_{120}O_2$ where vibrational modes are found to be splitted and shifted [54]. In his work, five-fold degeneracy in $H_g(1)$ mode of $C_{60}O$ was predicted. Rao *et al.* reported the splits at 271 cm^{-1} and 258 cm^{-1} for $C_{60}O$ due to the reduced symmetry of C_{60} in the presence of oxygen [43]. In the Raman spectrum, the epoxy group vibrations were expected near 1265

and between 800 and 900 cm^{-1} [54]. The shift in the $A_g(1)$ and $A_g(2)$ modes were also observed. The shift in $A_g(2)$ mode can be considered as the photo-polymerization of C_{60} [43].

Due to the presence of π-electron ring current, pristine C_{60} and C_{70} show purely diamagnetic behaviour and their susceptibilities are independent of temperature [56]. In fact C_{70} possess higher diamagnetic property than C_{60}. The larger number of hexagonal ring present in C_{70} contribute more π-electron rings current which results in higher diamagnetic susceptibility of C_{70}. Experimental study reports magnetic susceptibility (χ_M) of C_{60} to be -3.5×10^{-7} emu/g whereas C_{70} has magnetic susceptibility -5.9×10^{-7} emu/g [57, 58]. When the C_{60} crystals were exposed to UV light in oxygen, they showed strong evidences of ferromagnetism [59]. Room temperature ferromagnetism in fullerene treated by ultraviolet and heavy-ion irradiation are reported [59, 60, 61, 62]. When the oxygen molecule reacts with fullerene by light irradiation, a pair of $C–O^-$ is formed which has each an unpaired electron. The interaction between these spins on neighboring C_{60} cages is considered as the origin of ferromagnetism in the molecule. Although oxygen containing C_{60} was studied, magnetic property of $C_{70}O$ are yet to be explored.

2.3 Endohedral fullerenes

When atoms or clusters are encapsulated in the hollow space of fullerenes is referred to as endohedral fullerenes [63, 64]. 'Endohedral fullerene' concept was first proposed by Heath *et al.* in 1985 when they observed magic number feature m/z = 859 in the mass spectra of $LaCl_3$ impregnated graphite rod and concluded that a La atom was encapsulated within the soccer ball-shaped C_{60} [65]. Till

now four kinds of endohedral metallofullerenes (EMFs) are classified: (1) mono-metallofullerenes; (2) di-metallofullerenes; (3) nitride cluster-fullerenes, and (4) carbide cluster-fullerenes. In mono-metalofullerenes, only one metal atom(M) is encaged inside the fullerene and are usually written as M@C_{2n}(2n=80-92). Atoms listed to the left of the @ symbol are encaged in the fullerenes. These metal atoms can be encaged by higher fullerenes such as C_{72}, C_{74}, C_{80}, C_{80} and C_{84}. As the present work is focused on the EMF M@C_{82}, further discussion will be done according to that.

The first stable mono-metallofullerene isolated in considerable amounts was La@C_{82} [66]. Later, other EMFs M@C_{82} (M = Ce, Pr, Nd, Sm, Eu, Gd,Tb, Dy, Ho, Er, Yb and Lu) were prepared using carbon-arc evaporation techniques[67]. Laser photo-fragmentation studies provide strong evidences that metals are inside the carbon cage in metallofullerenes[68]. The synchrotron XRD study of Y@C_{82} confirmed that the structure of hollow C_{82} changes when atom(M) is inserted[69]. Theoretical calculations suggest that the M atom is mostly encapsulated inside the C_{82} isomer with C_{2v} symmetry [70]. Solvent free La@C_{82} and Dy@C_{82} crystal showed a fcc structure with a lattice constant a of 15.78 $\mathring{A}$ and 15.86 $\mathring{A}$ at 300 K [71, 72]. On the other hand, Eu@C_{82} and Gd@C_{82} are observed to be an anomalous endohedral structure in which the metal atom is located near the C–C double bond on the opposite side of the $C_{82}(C_{2v})$ cage along the C_2 axis [73, 74].

2.3.1 Electronic, optical and magnetic properties

When metal ion is inserted in fullerene cage, their isomeric structure becomes different from those of the corresponding empty fullerene. Electron transfers from a encaged metal atom to the carbon cage may alter the stability of the fullerene. ESR spectroscopy provides information on the electronic structures of the metallofullerenes. ESR spectra of La@C_{82}, Y@C_{82}, Ho@C_{82}, and Tm@C_{82}

showed low resolved but split hyperfine structure, indicating that the metal atoms exist in ionic form in the fullerene cage[75, 76, 77]. The nature of the metal-cage bonding was first observed in La@C_{82}[66]. High electron affinity of fullerenes results a formal charge state of $M^{3+}@C_{82}^{3-}$ where the metal cation is encapsulated in the negatively charged carbon cage. Within this model, the metal-cage bonding is purely ionic. Experimental X-ray diffraction studies and theoretical calculation confirm the most stable position of metal ion where the minimum of the electrostatic potential in C_{82}^{3-} is found [78, 79]. The concept of the ionic metal-cage bonding was further understood by theoretical calculations where it is suggested that the relative stability of the cage isomers drastically change upon inserting trivalent metal ions[70]. Although, the C_2 isomer is most stable for empty C_{82}, it becomes unstable when C_{82}^{3-} is formed. C_{2v} isomer is found to be most stable for C_{82}^{3-}. Ionic interactions play a vital role both in stabilizing the endohedral structures and in determining the positions of metal. DFT and Ab-initio calculation confirm that the La and Gd ion is located at an off-centered position of C_{82}[70, 80].

DFT calculation on Gd@C_{82} confirmed that the addition of Gd into C_{82} slightly lengthens the proximal C-C bond as well as the neighboring C-C bonds [81]. This deformation results in an energy difference between the $C_{82}(C_{2v})$ symmetry structure. Three electrons of Gd($4f^7 5d^1 6s^2$) is transferred into the LUMO and LUMO+1 of C_{82}. LUMO and LUMO+1 of C_{82} become doubly and singly occupied by the transfer of three electrons. Electron transfer between a Gd atom and C_{82} is shown in Figure 2.5.

In EMFs, the metal ions positioned off-center within the cage exhibits strong metal-cage vibrations. Information of vibrational structures of several metallofullerenes can be unveiled by IR and Raman spectroscopy [82, 83]. In the vibrational studies of endohedral fullerenes two major types of interactions can be distinguished: (i) cage internal vibrations (ii) metal-cage vibrations. Lebed-

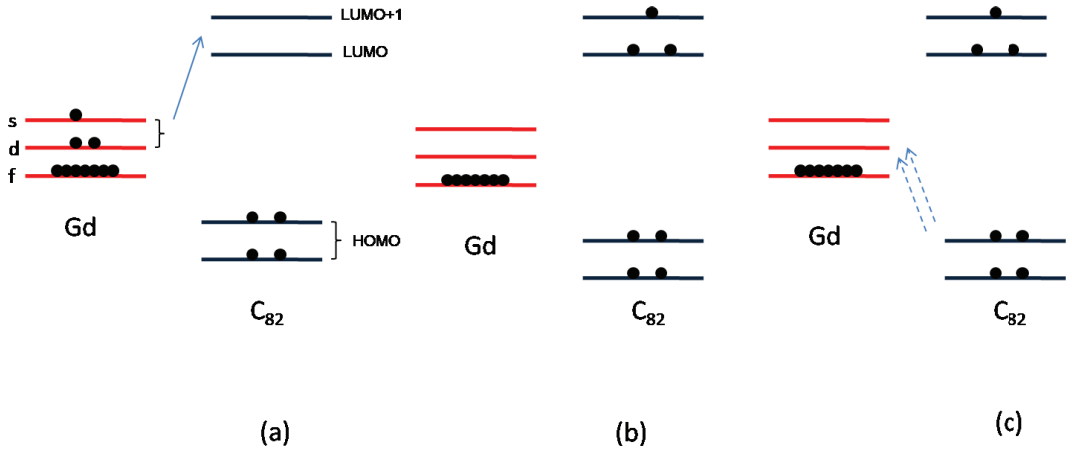

Figure 2.5: Charge transfer between Gd and C_{82}

kin *et al.* and Krause *et al.* reported vibrations due to the encapsulated metal ions in the cage for M@C_{82} (M = La, Y, Ce, Gd, Tm) based on IR and Raman measurements, where the EMFs show a metal-cage stretching vibration between 100-200 cm^{-1}. This region in IR and Raman spectra can be regarded as a "metal–fingerprint" range of M@C_{82}. Large atomic masses of the metal ions in the cage often lead to low-frequency metal–cage Raman vibrations. In the low frequency range, metal–dependent modes at 183 cm^{-1}(Y), 163 cm^{-1} (La), 162 cm^{-1}(Ce), 155 cm^{-1} (Gd) and 151 cm^{-1} (Dy) were observed. Theoretical calculation for carbon-metal interactions suggests two main vibrational features of the encaged ion between 40 and 150 cm^{-1}, shifting with the metal atom mass [82]. The higher frequency mode corresponds to 'longitudinal' vibrations (stretching) of the metal atom, whereas 'lateral' motion (movements parallel to the cage wall) is assigned by lower frequency vibration. Calculated vibrational frequencies of La@C_{82} below 200 cm^{-1} were reported at 159 cm^{-1}, 30 cm^{-1} and 27 cm^{-1} [84]. The longitudinal mode at 159 cm^{-1} represents the displacement of the La cation along the C_2 axis while the lateral modes at 27 and 30 cm^{-1} correspond to La displacements along the C_{82} cage in the right-left and out-of-plane directions. Similar method has been used to calculate the vibrational frequencies of Ca@C_{82}, Sc@C_{82}, and Y@C_{82} which are consistent with

the experimental measurements [82]. Longitudinal metal–cage vibration obeys

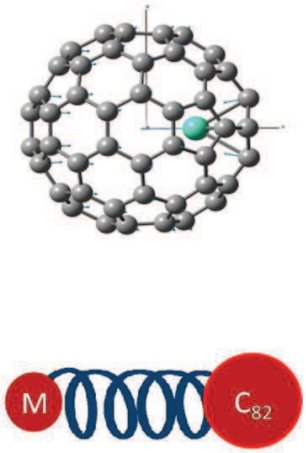

Figure 2.6: The structure of M@C_{82}(M=Gd) and linear oscillator model of M-C_{82} vibration.

simple harmonic oscillator model (Figure 2.6) and the vibrational frequency can be calculated as:

$$\nu(cm^{-1}) = 1302.1(k/\mu)^{1/2} \tag{2.3}$$

where k is the force constant (N cm^{-1}) and μ is the reduced mass of M-C_{82}. k value is strongly determined by the extent of the charge transfer from the metal to the cage. The position of encaged ion are extensively related to the valency of ion and the charge transfer between metal and cage. Thus, the frequency of the metal-cage stretching vibration may serve as a probe of the metal oxidation state.

Endohedral fullerenes have attracted broad interests due to the magnetic anisotropy of lanthanide ions. Magnetic property of mono-metallofullerenes M@C_{82} have been studied by Funasaka *et al.* and Huang *et al.*[85, 86]. Their study revealed that the magnetic moment of encaged ion was reduced in comparison to the corresponding free M^{3+} ions. This is because the carbon cage crystal field and orbital hybridization between metal and cage may partially quench the orbital angular momentum of the entrapped metal ion. The amount

of reduction in effective magnetic moment in $M@C_{82}$ depend on the orbital angular momentum (L) of the metal ion. As orbital angular momentum increases, electron orbital of M^{3+} becomes more anisotrpic; hence the quenching effect will be large. The isothermal magnetization and temperature dependence of a Curie–Weiss law at low temperature of $La@C_{82}$, $Ho@C_{82}$ showed paramagnetic behaviour [85, 86].

The properties of fullerenes and its derivatives are found to be modified when pressure and temperature are varied. To understand the structural deformation and phase transition in the crystal, lattice dynamics of solid under thermal and mechanical stress are discussed in the next section.

2.4 Raman spectroscopy at high pressure and low temperature

Pressure and temperature are the fundamental thermodynamic variables. Under mechanical and thermal stress, the equilibrium positions of the atoms in the lattice are displaced; which results in overall volumetric expansion or contraction of the lattice and change in interatomic forces. The changes in the interatomic forces modify the phonon vibrational frequencies which can be observed using Raman spectroscopy. The relation between the volume of lattice and its phonon frequency(ν_i) are expressed as [87]

$$\frac{\nu_i}{\nu_{i0}} = \left(\frac{V}{V_0}\right)^{\gamma} \tag{2.4}$$

where ν_{i0} is the frequency of the i^{th} phonon for the initial volume V_0. V is the volume of the solid after expansion or contraction. The Grüneisen parameter γ is used to investigate the relationship between thermal and elastic properties of

a solid. The dependence of the phonon frequency on pressure can be expressed as isothermal mode Grüneisen parameter (γ_{iT}):

$$\gamma_{iT} = \left(\frac{\partial ln\nu_i}{\partial lnV}\right)_T = \frac{1}{\beta\nu_i}\left(\frac{\partial \nu_i}{\partial P}\right)_T \tag{2.5}$$

Volume compressibility (β) is defined as

$$\beta = -\frac{1}{V_0}\left(\frac{\partial V}{\partial P}\right)_T \tag{2.6}$$

γ_{iT} can also be described in terms of bulk modulus (B_T):

$$\gamma_{iT} = \frac{B_T}{\nu_i}\left(\frac{\partial \nu_i}{\partial P}\right)_T \tag{2.7}$$

$$B_T = -V_0\left(\frac{\partial P}{\partial V}\right)_T \tag{2.8}$$

The dependence of the phonon frequency on temperature can be described by isobaric mode Grüneisen parameter(γ_{iP}):

$$\gamma_{iP} = \left(\frac{\partial ln\nu_i}{\partial lnV}\right)_P = \frac{1}{\alpha\nu_i}\left(\frac{\partial \nu_i}{\partial T}\right)_P \tag{2.9}$$

where linear thermal expansion coefficient(α) is expressed as:

$$\alpha = \frac{1}{a}\left(\frac{\partial a}{\partial T}\right)_P \tag{2.10}$$

Under harmonic approximation, $\gamma_{iP} = \gamma_{iT}$. In reality, phonon frequency shift is directly related to the thermal population of non-equidistant vibrational energy levels [88]. Thus temperature and pressure can be attributed to the anharmonic effect which changes phonon self vibrational potential energy. The temperature behaviour of the Raman frequency $\nu_i(T)$ at constant pressure can be expressed

as [88, 89]:

$$\nu_i(T) = \nu_0 + \Delta\nu^V(T) + \Delta\nu^{An}(T) \tag{2.11}$$

where ν_0 is the temperature independent harmonic frequency. $\Delta\nu^V(T)$ is the frequency shift due to the thermal expansion of the lattice and $\Delta\nu^{An}(T)$ corresponds to anharmonic phonon-phonon coupling. The contribution of thermal expansion in the frequency shift is expressed as [89]:

$$\Delta\nu^V(T) = \nu_0[exp(-\gamma_{iT}\int_0^T 3\alpha_T dT) - 1] \tag{2.12}$$

In anharmonic phonon-phonon interaction, a phonon with frequency ν decays into two (ν_m, m = 1, 2) and three (ν_n, n = 1, 2, 3) phonons which are known as three-phonon (cubic) and four-phonon (quartic) processes. Considering cubic and quartic decay contribution, $\Delta\nu^{An}(T)$ can be expressed as:

$$\begin{aligned}\Delta\nu^{An}(T) = A\left[1 + \Sigma\frac{1}{\exp(\frac{\hbar\nu_l}{k_BT}) - 1}\right] \\ + B\left[1 + \Sigma\frac{1}{\exp(\frac{\hbar\nu_m}{k_BT}) - 1} + \Sigma\frac{1}{(\exp(\frac{\hbar\nu_m}{k_BT}) - 1)^2}\right]\end{aligned} \tag{2.13}$$

where A and B are the cubic and quartic anharmonic constants. ν_l and ν_m are the frequencies of the phonons involved in the decay channels with energy conservation of $\nu_l = \nu_1 + \nu_2$ and $\nu_m = \nu_1 + \nu_2 + \nu_3$. ν_l of the phonons involved in the decay process can be determined by the phonon dispersion curves and phonon density of states with the constraint to conserve both energy and momentum in the decay. The Klemens model assumes a symmetric decay of one optical phonon into acoustic overtones with frequencies $\nu_1 = \nu_2 = \nu_o/2$ and $\nu_1 = \nu_2 = \nu_3 = \nu_o/3$ on the same branch for the cubic and quartic processes [90].

Raman linewidth is related to the inverse of phonon lifetime. Dependence of phonon linewidth with temperature can be explained by considering cubic

and quartic anharmonicity which can be expressed as [88, 89, 90]:

$$\Gamma^{ph-ph}(T) = \Gamma_0^{ph-ph} + C\left[1 + \Sigma\frac{1}{\exp(\frac{\hbar\nu}{k_BT}) - 1}\right] + D\left[1 + \Sigma\frac{1}{\exp(\frac{\hbar\nu}{k_BT}) - 1} + \Sigma\frac{1}{(\exp(\frac{\hbar\nu}{k_BT}) - 1)^2}\right] \tag{2.14}$$

where Γ_0^{ph-ph} is the temperature independent harmonic linewidth, and the factors C and D are the line broadening constants which arises from the three and four-phonon processes, respectively. Thus the temperature dependence of $\Gamma^{ph-ph}(T)$ is governed by non-equilibrium phonon occupation. The broadening of Raman linewidth due to high pressure involves anharmonic process such as the presence of a pressure gradient, amorphization and creation of defects. Under the applied pressure, the phonon dispersion influences on the decay process due to the changes in phonon frequencies throughout the Brillouin zone.

Temperature dependence of the anharmonic decay rate of optical phonons in both single-walled carbon nanotubes and graphite were reported by Chatzakis *et al.* using time-resolved anti-Stokes Raman spectroscopy. For both materials, the decay rate increased with temperature [91]. Thermal effect on Raman frequencies were also reported in $Sc_2@C_{84}$ and $C_2@Sc_2C_{84}$ [92]. In $Sc_2@C_{84}$, with a decrease in temperature, both blue-shifts and red-shifts in the cage vibration frequencies were observed, however, linewidth was not reported. In $C_2@Sc_2C_{84}$ both moderate peak broadening and temperature-induced peak shift were reported. The pressure dependence of the linewidths of III–V semiconductors was reported which was attributed to the corresponding change in the two-phonon density of states which affects the anharmonic interaction [93]. Effect of high pressure on the transformations of ferrocene-filled single walled carbon nanotubes (FC@SWCNTs) by Raman spectroscopy was reported where the distortion in nanotubes was explained by the different charge distribution on the nanotubes due to charge transfer and the effect from host–guest interac-

tions [94]. Pressure and temperature dependent shift in vibrational frequencies of C_{60} was studied by Tolbert *et al.* [95]. Below 250 K, the orientation of C_{60} changes and freezing of cage is observed; whereas due to high pressure, intermolecular interaction increases that results polymerization of C_{60}. Thus accurate measurements of the vibrational frequencies under pressure and temperature provide the required information on bonding properties and intrinsic anharmonic effects.

2.5 Temperature effect on thermal conductivity

Heat conduction is the transfer of heat from higher temperature region to lower temperature of a body resulting in equalizing of temperature. The basic law of thermal conduction states that the heat flux density Φ is proportional to the temperature gradient ΔT in an isotropic body:

$$\Phi = -\kappa \Delta T \tag{2.15}$$

where κ is the proportionality constant which is known as the thermal conductivity(TC) and is a characteristic of the material. The minus sign signifies that the temperature decreases in the direction of heat conduction. When 1-D heat flow is considered along the x direction in the plane, Eq. 2.15 becomes

$$\phi = \frac{\kappa A}{dx}(T_2 - T_1) \tag{2.16}$$

where $\phi = \Phi/A$, dx is the thickness, and T_1 and T_2 are the temperatures at two ends of the body.

The heat transport in solids at high temperatures depends on two mechanisms: the phonon and radiative mechanisms. The first one arises due to the

vibration of atoms in the crystalline lattice; the second one is due to the electron transitions between the energy levels in these atoms. In the thermal conduction of nonmetals, phonon mechanism is dominant. Thermal conductivity is described as

$$\kappa \propto C_k v_k^2 \tau_k \tag{2.17}$$

where C_k, v_k and τ_k are the specific heat, group velocity and phonon lifetime, respectively, of the phonon mode k [96]. At high temperature, anharmonic scattering increases that decrease the phonon lifetime. Reduction in phonon group velocity and the phonon lifetime due to strong phonon-phonon scattering at high temperature results in the thermal conductivity reduction. For bulk crystalline or amorphous materials $\kappa \propto 1/T$. However,the temperature-dependent TC of nanostructures are different from bulk materials. Temperature dependent TC of bulk diamond single crystals and ultra-nanocrystalline diamond (UNCD) was reported [97]. It is found that, unlike bulk diamond single crystals, the TC of UNCD increases with temperature. High temperature phonon transport in nanostructures can be determined by considering two mechanisms: scattering at the grain boundaries and the phonon-phonon interaction. L. Braginsky considered a model to explain high temperature thermal transport in nanostructure where he showed that below Debye temperature, TC increases with temperature due to increase of the number of the phonons responsible for the heat transport; whereas, above Debye temperature, TC is constant [98]. Temperature-dependent TC of single–walled carbon nanotubes (SWCNTs) in the temperature range 8-350 K was reported where TC decreased with decrease in temperature [99]. Gao *et al.* showed that TC of C_{60} and $H_2O@C_{60}$ increases along temperature gradient. [100]. In addition, the TC of empty C_{60} was found to be reduced when water molecule is encapsulated in it, which suggested that the encapsulation ion or molecule in the fullerene suppresses the thermal transport through the non-bond interaction with carbon cage. The similar kind of

reduction in thermal conductivity has also been found in the carbon nanotube encapsulating with C_{60}, Gd@C_{82} and Er_2@C_{82} [101]. In this thesis, temperature dependence of thermal conductivity of some doped fullerenes have been studied (Gd@C_{82}, Dy@C_{82}, $C_{60}O$ and $C_{70}O$).

2.6 Pressure effect on thermal conductivity

Pressure dependence of TC has been observed in many materials although there is no direct relationship between TC and pressure. Hence, the effect of pressure on TC can be explained by considering the contribution of thermo-elastic Grüneisen parameter(γ) in thermal conductivity. For nonmetallic crystaline materials, acoustic phonons are mainly responsible for heat conduction. Lattice thermal conductivity due to phonon–phonon scattering was presented by Glen A. Slack where thermal conductivity was approximated as [102]

$$\kappa = A\frac{M_a \delta \Theta^3}{\gamma^2 n^{2/3} T} \tag{2.18}$$

where M_a is average mass of an atom in the crystal, n is the number of atoms per unit cell, δ^3 is average volume occupied by one atom of the crystal and Θ is the Debye temperature. A is a constant that depends on γ. On the basis of Eq. 2.18, the solid should have large number of atoms per unit cell and large Grüneisen parameter to possess a low TC. At high pressure, the phonon frequency shift is obtained due to the change in phonon self vibrational potential energy. Hence, the value of Grüneisen parameter is modified which in turn modifies the TC. The variation of the Grüneisen parameter with high pressure was reported for NaCl, Li, Na and K [103, 104, 105, 106]. ZH Fang established a relation for pressure dependent Grüneisen parameter [103]:

$$\gamma(P) = \gamma_0 \left(1 + \frac{\beta_0 P}{B_T}\right)^{-Q/\beta_0} \tag{2.19}$$

where B_T is isothermal bulk modulus and β_0 is the first-order pressure derivative of B_T at zero pressure. The second Grüneisen parameter Q is a pressure-independent parameter for a given temperature. Pressure dependence of the Grüneisen parameter in Li, Na, and K near room temperature was studied where decrease in Grüneisen parameter was reported with increasing pressure [106]. From the Eq.2.18 and Eq.2.19, one can predict an increase in TC when pressure is increased. Increase in TC of compressed C_{60} clusters was reported for pressure above 0.3 GPa [107]. When C_{60} is polymerized, new phonon modes appear which could contribute to heat transport. The compressed fullerene molecules inside the carbon nanotube peapod structures have been found to possess 35-55% reduction in their TC [101]. Thus, pressure influences heat conduction in the material and hence its thermoelectric property can be modulated.

2.7 Spectroscopic method for thermal conductivity evaluation

To determine the TC of bulk and thin film materials, the measuring techniques are generally categorized into two groups: steady state method and transient method [18]. Transient method usually measures the TC by considering time-dependent energy dissipation process in a sample. 'Laser flash' technique, belongs to this group which measures the thermal diffusivity (D_T). By knowing the material density (ρ) and specific heat (C_p) from separate experiments, the TC can be obtained by using the equation $\kappa = D_T \rho C_p$. Another common transient method is 3ω technique which is extensively used to measure the TC of thin films. In this technique TC is determined from the temperature dependence of electrical conductivity [108].

In the steady state method, TC can be measured by establishing a tem-

perature difference which is independent of time. Raman thermography or opto-thermal Raman measurement technique is an example of the steady state method for thermal conductivity examination. In this technique, the laser acts as a heating source that heats the sample surface. Schematic representation of laser heating profile on the film is shown in Figure 2.7. The local temperature rise in the surface is deduced from the Raman peak shift method. Being non-destructive and non-contact method, Raman spectroscopy is a popular technique to evaluate thermal properties of nanomaterials and thin films [109, 110, 111]. Perichon *et al.* in 1999 measured the thermal conductivity(κ) of porous silicon using the micro-Raman method by combining the effect of the temperature-dependent Raman peak shift with the basic equation of the thermal scanning probe microscopic method [112]:

$$\kappa = \frac{2L}{\pi a \Delta T} \tag{2.20}$$

where a is the laser spot diameter, temperature rise ΔT is due to the heating effects by the laser power L.

Perichon *et al.* clubbed the micro-Raman technique with thermal scanning probe microscopic method proposed by Nonnenmacher and Wickramasinghe [113]. This combination produces a huge error in measurement as heat sources in the two methods are different. To reduce the error unsuitability of the equation, the heat source with Gaussian heat distribution profile was considered and a new basic equation was derived to establish the relationship between TC and the laser-induced local temperature rise. [114, 115, 116].

In Raman spectroscopy experiments, the temperature distribution is not homogeneous in the sample region as the excitation is caused by a Gaussian laser beam. The beam center on the sample is the hotter region and laser beam edge is the colder region of the sample. The intensity of the Gaussian laser

beam is described as

$$I(r) = \frac{P}{\pi\omega^2} e^{-\frac{2r^2}{\omega^2}} \tag{2.21}$$

ω is the radius at which the laser beam intensity is e^{-2} times of its maximum value and r is the radius from the center of the beam in z direction into the material. P is the total incident power.

When the film thickness is at least one order larger than the diameter of the laser source, the heat distribution is hemispherical through the film [112, 117]. For the steady-state heat conduction with constant thermal conductivity κ, the general heat transfer equation in cylindrical coordinates is:

$$\frac{1}{r}\frac{\partial}{\partial r}(\kappa r\frac{\partial T}{\partial r}) + \frac{1}{r^2}\frac{\partial}{\partial \theta}(\kappa\frac{\partial T}{\partial \theta}) + \frac{\partial}{\partial z}(\kappa\frac{\partial T}{\partial z}) = 0 \tag{2.22}$$

As we are considering a thin film, the temperature distribution is not changing in the θ direction. Hence, the variable θ can be eliminated from Eq.2.22. Hence the Eq.2.22 reduces to:

$$\kappa\frac{\partial^2 T}{\partial r^2} + \frac{\kappa}{r}\frac{\partial T}{\partial r} + \kappa\frac{\partial^2 T}{\partial z^2} = 0 \tag{2.23}$$

Now energy absorbed per unit volume per sec is

$$G(r, z) = \alpha e^{-\alpha z} f(r/\omega) \tag{2.24}$$

α is the attenuation constant of the beam in the solid. Using the notation $R = r/\omega, Z = z/\omega, W = \alpha\omega$ Eq. 2.24 becomes

$$G(r, z) = \frac{P\alpha}{\pi\omega^2} e^{-ZW} f(R) \tag{2.25}$$

For Gaussian beam we take

$$f(R) = exp(-R^2) \tag{2.26}$$

Temperature rise can be written as

$$T(R, Z, W) = T_{max} N(R, Z, W) \tag{2.27}$$

T_{max} is the maximum temperature rise at the beam center(R=0) on the surface(Z=0). N(R,Z,W) is the normalized temperature rise for a finite attenuation depth W. When $W \to \infty$,

$$N(R, Z, \infty) = \int_0^\infty e^{-\lambda Z} J_0(\lambda R) F(\lambda) d\lambda \tag{2.28}$$

For any λ, $J_0(\lambda R)$ is the Bessel function of first kind and zeroth order. F(λ) is the Bessel transformation of f(R) where

$$F(\lambda) = \int_0^\infty f(R) J_0(\lambda R) R dR \tag{2.29}$$

The complete solution of temperature rise is

$$T(R, Z, W) = B \int_0^\infty J_0(\lambda R) F(\lambda) \times \frac{W e^{-\lambda Z} - \lambda e^{-WZ}}{W^2 - \lambda^2} d\lambda \tag{2.30}$$

where $B = \alpha P / 2\pi\kappa F(0)$. Now the temperature rise at the beam center(R=0) at the surface(Z=0)

$$T(0, 0, W) = B \int_0^\infty \frac{F(\lambda)}{W + \lambda} d\lambda \tag{2.31}$$

when the beam attenuation is very large ($W \to \infty$), all the heat is generated

in a surface layer. Then

$$T(0,0,\infty) = B\int_0^\infty \frac{F(\lambda)}{W}d\lambda \tag{2.32}$$

$$= \frac{P}{2\pi\omega\kappa}\int_0^\infty f(R)dR \tag{2.33}$$

$$= \frac{P}{2\sqrt{\pi\omega\kappa}} \tag{2.34}$$

hence the thermal conductivity κ is obtained as:

$$\kappa = \frac{P}{2\sqrt{\pi\omega T_{rise}}} \tag{2.35}$$

This is the most conventional equation to calculate TC using spectroscopic

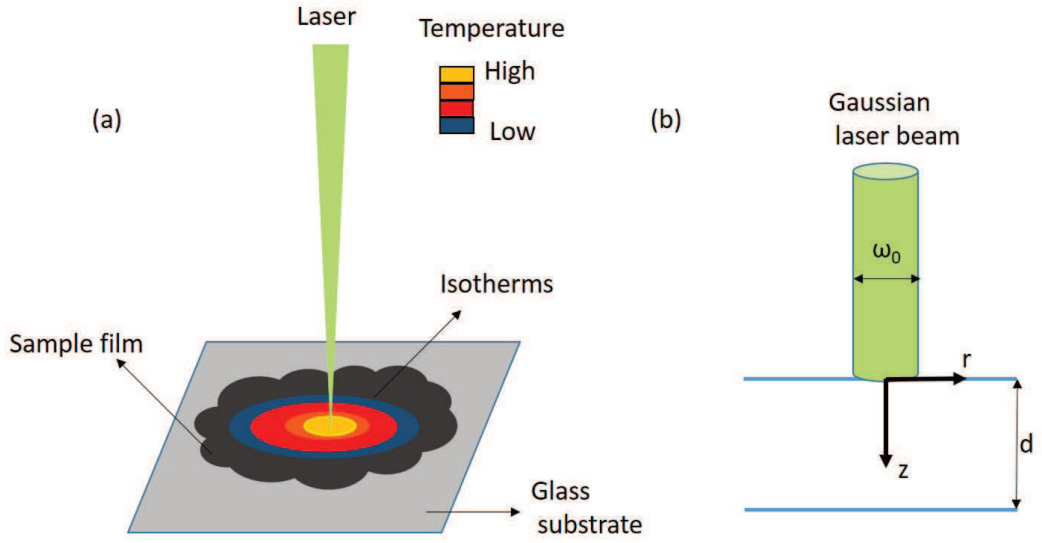

Figure 2.7: (a) Schematic representation of laser heating profile on the film. (b) Film in cylindrical coordinate system (r, z)

method. In this work, Eq.2.35 has been used to calculate the thermal conductivity which will be discussed later.

Part II

EXPERIMENTAL TECHNIQUES

Chapter 3

Materials and methods

In this chapter, the description of the materials used in this work are included and the details of the experimental techniques required for the measurements are presented. I begin with the synthesis and purification of fullerene derivatives used for further characterizations. Raman spectroscopy with cooling set up and with diamond anvil cell(DAC) are described extensively.

3.1 Materials

In this work two kinds of fullerenes derivatives were studied:

- Endohedral metallofullerenes (EMFs): Gd@C_{82} and Dy@C_{82}
- Exohedral fullerenes (oxides): $C_{60}O$ and $C_{70}O$

3.1.1 Dy@C_{82} and Gd@C_{82}: preparation

Our collaborators from Nagoya University, Japan, prepared two mono metallofullerenes Dy@C_{82} and Gd@C_{82}. Both samples were extracted from the soot obtained by DC arc discharge method [118, 119]. In the obtained soot, mixture of empty fulerenes along with the structural isomers were also generated. For the separation and purification of Dy@C_{82} and Gd@C_{82}, High Perfor-

mance Liquid Chromatography (HPLC) was performed. Dy@C_{82} and Gd@C_{82} were purified from various hollow (C_{60}–C_{110}) fullerenes by the two-stage HPLC method[120, 121]. Isolation of Dy@C_{82} isomer was also done by the same procedure. The obtained HPLC chromatograph of Dy@C_{82} and Gd@C_{82} are shown in Figure 3.1(a) and (c). To confirm the purified fractions of the met-

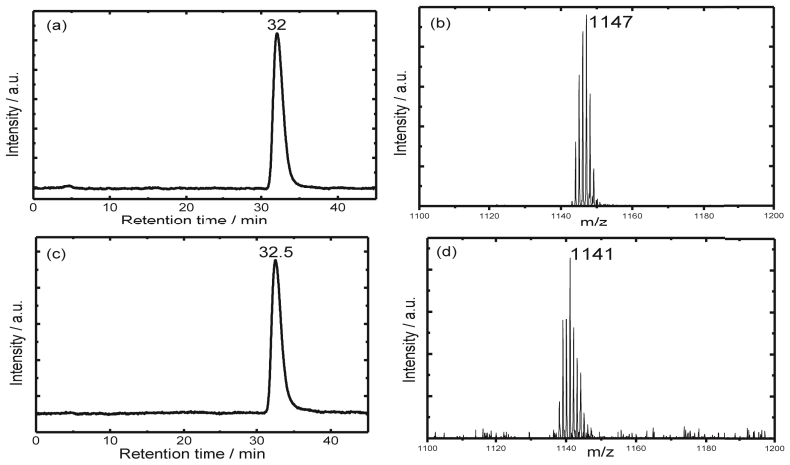

Figure 3.1: HPLC chromatograph of (a) Dy@C_{82} and (c) Gd@C_{82}. Positive mass spectrum of (b) Dy@C_{82} and (d) Gd@C_{82}.

allofullerenes, mass spectrometry was carried out on the major fractions, to measure the molecular weight of the fragments. The positive mass spectra for Dy@C_{82} and Gd@C_{82} are shown in Figure3.1(b) and (d). The expansion of the mass range centred at 1147 m/Z and 1141 m/Z is consistent with the predicted isotopic distribution for Dy@C_{82} and Gd@C_{82}[122, 123].

The purity of isomer specific Dy@C_{82} and Gd@C_{82} were obtained as >96.5% and >98.5% respectively which were used for further characterization.

3.1.2 $C_{60}O$: preparation

C_{60} of 99.5% purity was imported from SES Research. C_{60} was oxidized as per the method described by Heymann *et al.* [124]. Pristine C_{60} was dissolved in toluene in a round bottom glass flask. The solution was irradiated with

UV light using 100 W short arc Hg lamp and simultaneously oxygen gas was bubbled through the solution. The solution of C_{60} in toluene was exposed to UV irradiation for 3 hr. After photo-transformation, the precipitate was obtained. The solution was filtered using Whatmann filter paper no. 1 and dried in ambient condition for 10 days. The obtained product was labelled as $C_{60}O$. To avoid further oxidation, the obtained product was dissolved in CS_2 and was used for further characterization. The oxidation of C_{60} was confirmed by room temperature UV-Vis and Raman measurements which will be discussed Chapter 5.

3.1.3 $C_{70}O$: preparation

C_{70} of 99% purity was imported from Reinste NanoVentures. Synthesis of oxidized C_{70} was done by following the method reported by *Ko et. al.* where oxidising agent Chromium (VI) oxide (Cr_2O_3) reacts with pristine C_{70} [125]. Cr_2O_3 was kept dissolved in acetone for 5 hours and solution was labelled as solution A. As acyclic ketones are relatively stable to Cr(VI) oxidation, acetone is used as solvent for Cr(VI) oxidation [126]. Pristine C_{70} was dissolved in CS_2 labelled as solution B. After mixing both solution A and B, the resultant solution was ultrasonicated for 30 minutes using 180 W LABSONIC-M homogenizer with 24KHz frequency. The solution was filtered using Whatmann filter paper no. 1 and the precipitate was dried in ambient condition. The product was labelled as $C_{70}O$. To avoid further oxidation, the obtained product was dissolved in CS_2. The oxidation of C_{70} was confirmed by room temperature UV-Vis and Raman measurements which will be discussed in Chapter 5.

3.1.4 Thin film preparation and thickness measurement

All the samples were dissolved in CS_2 and were drop-casted into thin-films on the glass substrate for Raman measurements. The samples were dried on a

Figure 3.2: Ultrasoncation of C_{70} using LABSONIC-M homogenizer.

10 mm×10 mm glass slide by the drop-casting method to make a thin film.

The thickness of the thin films was determined by the 'fringing effect' of the FTIR spectrum [127, 128]. The fringing effect originates from constructive and destructive interference of the IR beam from the parallel surfaces of the sample. When constructive interference occurs, the condition for interference maxima can be written as:

$$2nt = k\lambda \tag{3.1}$$

Refractive index of the material is n, λ is the free space wavelength of the radiation being detected and k is an integer. There are only certain values of k for which constructive interference takes place. The difference between the two values of k and k_1 corresponding to two wavelengths λ and λ_1 is the number of cycles of maxima in the recorded spectrum. The difference between k and k_1 by counting cycles of maxima

$$k - k_1 = 2nt(\frac{1}{\lambda} - \frac{1}{\lambda_1}) = 2nt(\nu - \nu_1) \tag{3.2}$$

$k - k_1$=N is the number of fringes in the spectral range $\nu - \nu_1$. From this fringing effect, the thickness (t) of the film can be calculated using the following

equation:

$$t = \frac{1}{2n} \times \frac{N}{\nu - \nu_1} \tag{3.3}$$

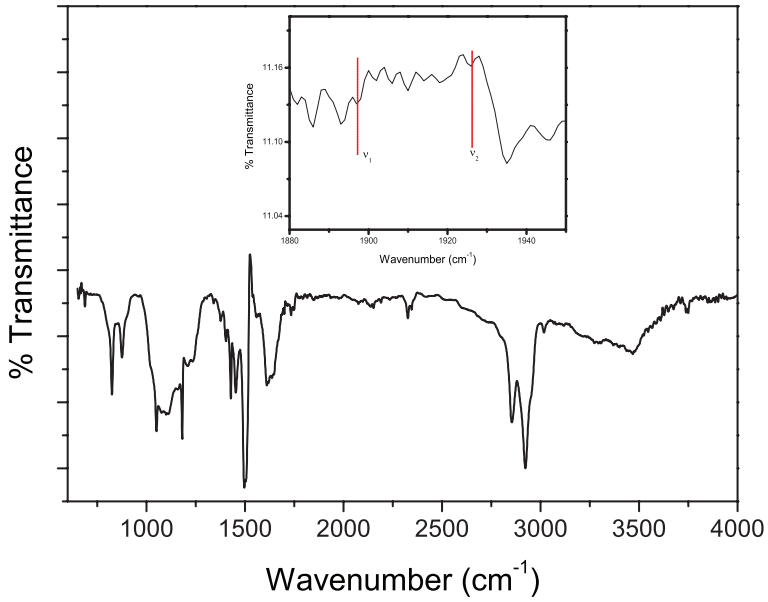

Figure 3.3: FTIR spectrum of C_{60} film by drop-casting method showing "fringing effect".

In the spectrum shown in Figure 3.3, we selected starting and ending points in the spectrum of 1893 and 1918.6 cm^{-1} and the number of fringes within this spectral region were 6. Refractive index of C_{60}=2.2 [129]. The thickness of the fullerene films for one drop prepared by drop casting method were calculated by ratiometric measurement. The thickness of $C_{60}O$ and $C_{70}O$ were found to be $\sim$ 0.32 mm; whereas the thickness of Gd@C_{82} and Dy@C_{82} was found to be $\sim$ 0.37 mm.

3.2 Experimental techniques

3.2.1 Raman spectroscopy

Raman scattering is a powerful tool that is sensitive to the vibrational features of nanostructures. This section delivers an overview to the basics of Raman

scattering and presents the theoretical considerations associated with instrument design.

Light scattering process is mainly categorized as elastic and inelastic scattering. When light scatters with the same energy as the incident wave, it is known as Rayleigh scattering. When the emitted photon has a different energy compared to the incident light, it is known as Raman scattering. In 1928, Dr. C V Raman observed a shift in frequency of the spectrum of scattered light compared to incident light during his experiment [130]. The frequency shift($\Delta\nu$) can be calculated as:

$$\Delta\nu(cm^{-1}) = (\frac{1}{\lambda_{ex}} - \frac{1}{\lambda_{Raman}}) \times 10^{-7} \tag{3.4}$$

wavelength of excitation source is λ_{ex} and λ_{Raman} is the wavelength of Raman scattering in nm.

In the classical theory of Raman Effect, the interaction of molecules under the incident radiation of electric field (E) is considered. When a beam of radiation described by an electric field E interacts with the sample, it induces electric dipole moment P = αE which deforms the molecules. Molecular deformation is determined by molecular polarizability (α). In presence of beam radiation, each molecule will suffer electric field as

$$E = E_0 \sin(2\pi\nu t) \tag{3.5}$$

where ν is the radiation frequency. Thus, induced electric dipole moment P = $\alpha E_0 \sin(2\pi\nu t)$. In order to be Raman-active, the molecule must possess a molecular bond with polarizability that varies as a function of interatomic distance. The variation of the polarizability during the vibrations of the molecule can be expressed as considering the first order Taylor expansion with respect

to the coordinate q_i of vibration:

$$\alpha = \alpha_0 + \frac{d\alpha}{dq_i} \tag{3.6}$$

coordinate q_i can be written as, $q_i = q_0 \sin(2\pi\nu_{vib}t)$. ν_{vib} is vibration of frequency which changes the polarizability. Then, the induced electric dipole moment becomes

$$P = \alpha E_0 \sin(2\pi\nu t) + \frac{d\alpha}{dq_i} E_0 q_0 \sin(2\pi\nu_{vib}t) \tag{3.7}$$

Using the trigonometric identity, Eq. 3.7 becomes

$$P = \alpha E_0 \sin(2\pi\nu t) + \frac{1}{2}\frac{d\alpha}{dq_i} E_0 q_0 \cos 2\pi(\nu - \nu_{vib})t - \frac{1}{2}\frac{d\alpha}{dq_i} E_0 q_0 \cos 2\pi(\nu + \nu_{vib})t \tag{3.8}$$

Eq. 3.8 indicates that induced dipole moment of the molecule oscillates with the frequency ν, $\nu - \nu_{vib}$ and $\nu + \nu_{vib}$. It is noted that if $\frac{d\alpha}{dq_i}$=0 then the dipole oscillates at incident radiation frequency only. Hence, in order to be Raman-active, change in molecular polarizability during the vibration is necessary.

The first term of Eq. 3.8 represents the Rayleigh scattering, whereas the second term with frequency $\nu - \nu_{vib}$ corresponds to Stokes Raman scattering and finally the third term with frequency $\nu + \nu_{vib}$ corresponds to anti-Stokes Raman scattering. Both the Stokes and anti-Stokes Raman scattering are inelastic scattering which can be explained in terms of energy transfer between incident radiation and scattering molecule. In case of Stokes scattering, molecular phonon gains energy during the interaction of incident photon whereas in anti-Stokes scattering molecular phonon loses energy during scattering. The energy loss or gain is equivalent to the energy difference (ΔE) between two involved energy states. When a molecule gains energy photons will be scattered with the frequency $\nu - \Delta E/\hbar$ and when the molecule loses energy, photons will be scattered with the frequency $\nu + \Delta E/\hbar$. A schematic representation of the

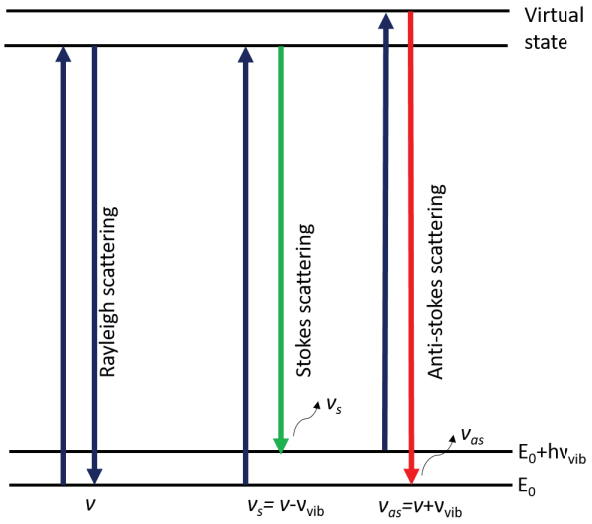

Figure 3.4: Schematic representation of energy diagram for the Raman scattering.

Raman effect is shown in Figure 3.4.

Stokes lines involve the transitions from lower to higher energy vibrational levels and therefore, Stokes lines are more intense than anti-Stokes lines and hence are measured in conventional Raman spectrometer [131, 132]. At room temperature, the ground state of the molecule is most populated. Hence, the intensity of Stokes scattering is expected to be large. When temperature increases, population in the excited state is higher than the ground state. Thus the intensity of anti-Stokes scattering increases with increasing sample temperature. The intensity ratio of the Stokes and anti-Stokes scattering was determined as [133]:

$$\frac{I_{stokes}}{I_{anti-Stokes}} = (\frac{\nu - \nu_{vib}}{\nu + \nu_{vib}})^4 e^{(h\nu_{vib}/k_B T)} \tag{3.9}$$

Spectrometer details

Micro-Raman spectrometer usually consists of:

- A monochromatic excitation source (laser)
- An arrangement for illuminating light on the sample and collecting the scattered light (optical microscope)

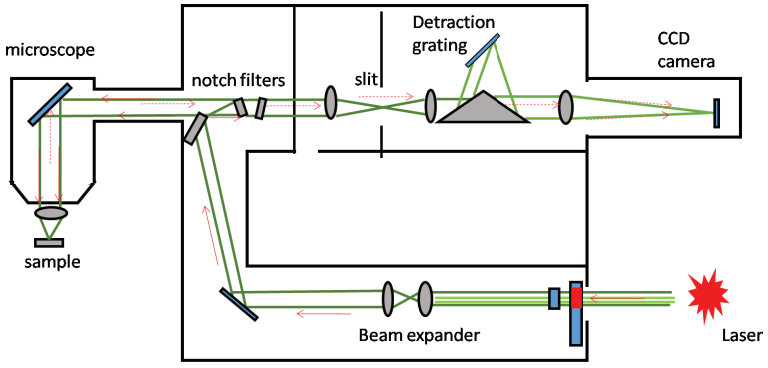

Figure 3.5: Schematic diagram of Raman experimental setup.

- An arrangement of filtering out strong Rayleigh light and allow the small fraction Raman scattered light to reach the detector (holographic 'notch' or dielectric 'edge' filters)
- Diffraction grating for splitting the Raman scattered light into different wavelengths
- A light-sensitive device for detecting the spectrum
- A computer to control the instrument and analyse and store the data

Figure 3.5 shows the layout of a Raman microscope and the schematic diagram of the instrument. Raman experiments described in this thesis were performed using a Renishaw inVia RM-2000 Spectrometer and Jobin Yvon Horibra LABRAM HR-800 spectrometer. Horibra LABRAM HR-800 spectrometer was used to perform low temperature Raman measurements; whereas, laser power and pressure induced Raman measurements were carried out by Renishaw inVia Spectrometer.

Two excitation sources of wavelength 514.5 nm (Ar ion laser) and 785 nm (He-Ne laser) were used in Renishaw inVia RM-2000 Spectrometer. For 514.5 nm excitation, 2400 l/mm grating was used and for 785 nm excitation, 1200 l/mm grating was assigned in the instrument setup [134]. In Horibra LABRAM

HR-800 spectrometer,two excitation sources wavelength 488 nm with 600 l/mm and 632.8 nm with 1800 l/mm grating were used for the measurements. For sample illumination and collection of scattered light, Leica optical microscope with 50X was used objective during all the measurements. The microscope objective plays a key role in increasing the spatial resolution, by focusing the laser to a small spot size and thus, maximizing the collection efficiency of the Raman scattered light. In order to obtain high signal-to-noise ratio in Raman measurements, it is necessary to block Rayleigh scattering from reaching the detector while transmitting the Raman signal. Raman notch filter is used in the optical path of scattered light to block the Rayleigh signal. The filtered Raman light is collimated by the collection mirror and directed towards the diffraction grating where the scattered light is split into different wavelengths. The efficiency of diffraction grating depends on the wavelength of light and diffraction order in which the grating is operated. The spread-out of the spectral domain across the focal field of the spectrometer is defined by linear dispersion [135]:

$$\frac{dx}{d\lambda} = \frac{knf}{\cos\beta} \tag{3.10}$$

where f is the focal length of focusing mirror, β is the angle of the diffracted light of wavelength λ, k is the diffraction order and n is groove density of the grating. The extent of wavelength domain of a spectrometer is inversely proportional to the dispersion of the grating due to its fixed geometry. The decrease in the groove density lowers the dispersion and increases wavelength coverage detector. However this leads to lower spectral resolution.

Raman scattering is very weak and therefore tends to require long integration times in order to collect enough photons to measure a discernible signal. Being photosensitive silicon device, Charged Coupled Device (CCD) is used as a detector to collect Raman signal. The selection of correct CCD strongly influences the performance of the instrument. CCD performance is represented

by quantum efficiency which is defined as the percentage of detected photons out of the total of incoming photons. The detector sensitivity can be enhanced when the Raman shift region overlaps with the region of maximum quantum efficiency of the CCD detector.

Laser and power specification for the instrument

Since Raman spectroscopy is based on the ability to measure a shift in frequency (or wavelength), it is essential that the laser frequency (or wavelength) is extremely stable and does not mode hop, since this will cause errors in the Raman shift. In pursuit of the ideal excitation wavelength (λ_{ex}) few factors should be taken into account. Excitation efficiency is one of the important factors to choose excitation wavelength. Raman scattering efficiency is inversely proportional to λ_{ex}^4 [136]. This is why shorter excitation wavelengths are preferable for Raman measurements. However, a drawback of using shorter wavelength excitation is it enhances florescence in the sample, particularly for organic samples or biomaterials. Fluorescence can be significantly reduced by using near infra-red (NIR) excitation, but this also reduces the Raman signal significantly. Being weak fluorescent, inorganic materials, carbon nanotubes and fullerenes are generally studied with 488-532 nm laser excitation.

Excitation wavelength and power play a significant role in sample degradation. Longer excitation wavelength heats the sample very fast that causes sample damage. Generally, during Raman measurements the laser beam causes local heating effect on the surface of the sample which increases the surface temperature. To avoid sample burning or degradation, Raman measurements were performed below 2 mW in this work.

Laser spot size measurement

In laser power dependent Raman experiment laser spot size plays as an important role in surface heat distribution. The size of the focused laser beam is limited by diffraction and dependent on the excitation wavelength. For uniform illumination of the lens, the laser beam spot has the Airy disc intensity profile. The ideal laser focused spot (Airy disk diameter) using any optics is determined by the following equation [136]:

$$a = 1.22 \times \lambda / NA \tag{3.11}$$

where λ is excitation wavelength and NA is effective numerical aperture of the objective. It is important to note that the objective used to deliver the laser light affects the laser energy density. The relative energy density and peak power for the 5X, 20X and 50X objectives are shown in Figure3.6. The peak energy density decreases by 50% for the 20X and 87% for the 5X objective [3].

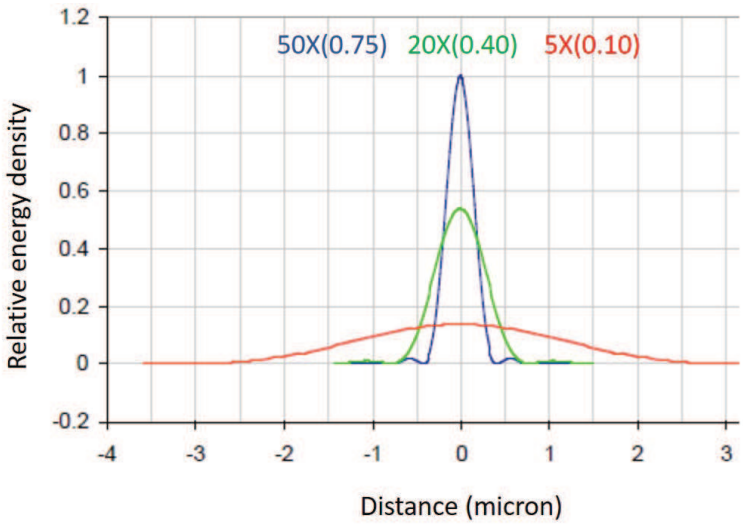

Figure 3.6: Diffraction limited focus for 5X, 20X and 50X objectives calculated for 514.5 nm excitation (reprinted from ref.[3])

The actual laser beam diameter depends upon the beam quality (M^2) and

alignment of the optics. M^2 parameter indicates how close the experimental laser beam is to the perfect Gaussian beam. When M^2 parameter is 1 for Gaussian beam and the aperture of the lens is illuminated more uniformly, the laser beam can be focused to the diffraction limit. In reality, M^2 parameter is generally > 1, thus minimum beam radius will be larger by the M^2 factor. Generally Gaussian beam diameter is measured at $1/e^2$ intensity point which is called the beam waist. M^2 can be determined as [137, 138]:

$$M^2 = \frac{d_{0R}\theta_R}{d_0\theta} \tag{3.12}$$

where d_{0R} and θ_R are the beam diameter at beam waist and far-field divergence of the real beam. d_{0R} is the theoretical Gaussian beam diameter and θ is theoretical diffraction–limited divergence. The excitation source used in the Raman spectroscopy is a Gaussian laser beam. In this work Gaussian beam diameter is evaluated from the image of the focused laser spot on the sample surface using a calibrated camera mounted on the microscope. The cross-sectional beam profile of 514.5 nm and 785 nm excitation laser spots were plotted using ImageJ software. After fitting with the Gaussian function, beam diameters at beam waist were determined for both the excitation source. Gaussian beam profile for 514.5 nm and 785 nm excitations are shown in Figure 3.7. Beam diameter d_0 was found to be 3.6μm and 7.7μm for 514.5 nm and 785 nm excitation respectively.

3.2.2 Raman spectroscopy with heating/cooling setup

Temperature dependent Raman experiments reported in this thesis were performed using a Micro Raman system from Jobin Yvon Horibra LABRAM-HR. 50X objective was used for low temperature measurements and the spectral resolution was of the order of 1 cm^{-1}. The Raman spectrometer with temper-

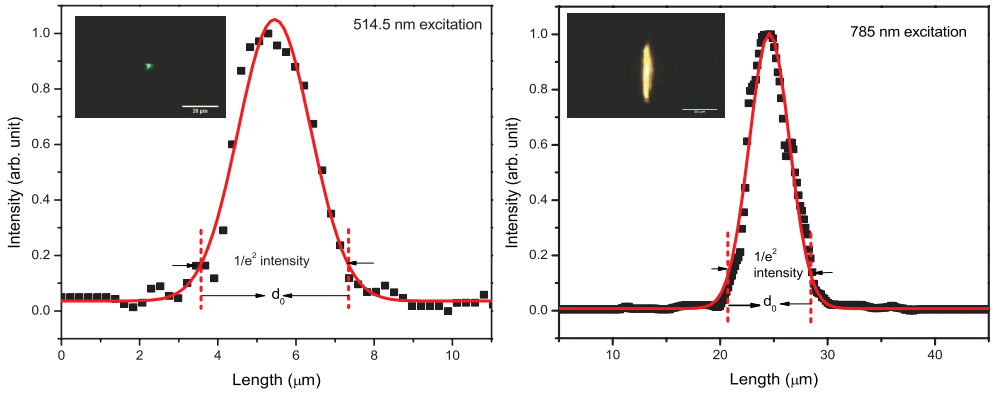

Figure 3.7: Gaussian beam profile of 514.5 nm and 785 nm excitation laser spots. The insets show the image of the respective laser spots acquired using 50 X objective on the Raman microscope.

ature control setup is shown in Figure 3.8. Linkam THMS 600 heating/cooling microscope stage (Figure 3.9) was used to vary the temperature of the sample during measurements. This temperature variable microscope stage allows a temperature range of 77 to 900 K. All temperature dependent Raman measurements were performed for this work by varying temperature from 300 K to 80 K.

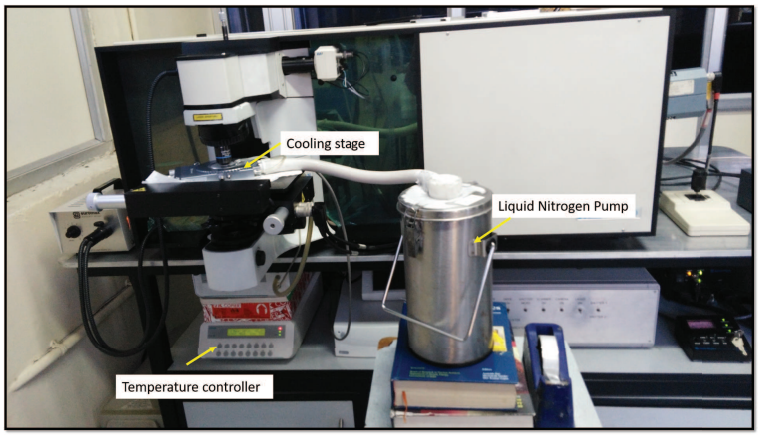

Figure 3.8: Temperature regulator system attached with Raman spectroscopy

To view the sample using transmitted light it requires a long working distance condenser lens. The objective lens working distance for the THMS600 stage was 4.8 mm [139]. Samples were loaded onto a 0.17 mm thick coverslip and were positioned on a highly polished pure silver heating element that helped

in excellent heat transfer and extremely sensitive temperature measurement. Pt100 platinum resistor sensor provided stable temperature signal with 0.01^0C accuracy. The sample cell on the stage was covered with quick-to-fit gas ports so that sample atmosphere can be controlled by gas flow and condensation was eliminated by dry nitrogen gas purge supplied by the LNP95 cooling pump.

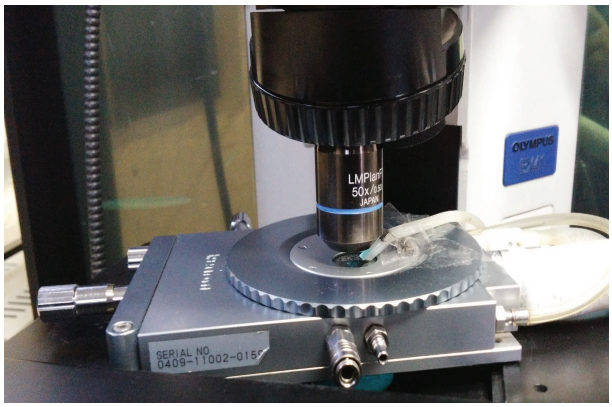

Figure 3.9: Linkam THMS 600 heating/cooling stage.

Figure 3.10: LNP95 liquid nitrogen cooling pump connected to THMS600 stage

The LNP95 cooling system shown in Figure 3.10, consisted of the 2 liter Dewar and a control unit housing the pump. The precise control of liquid nitrogen flow permits specific stages to be controlled at cooling rates from 0.01^0C/min to 100^0C/min. Recycled dry nitrogen gas was used to purge the sample chamber and clear the upper lid window surface of condensation. The thin silicon capillary tube should be kept pointing upwards as it carries exhaust nitrogen

gas and is used to prevent the blurring of the top of the window on the stage lid [139].

3.2.3 High pressure experiment

Under normal conditions, solids exhibit a particular crystal structure for which the total energy is minimum. However, on the application of high pressure the atomic arrangement in solid changes resulting in a change in interatomic distance and hence crystal structure is distorted.

Studies of materials under extreme pressure were made possible by the combination of the diamond anvil cell (DAC) technique and the pressure calibration based on ruby fluorescence method. The primary components of DAC are:

- Diamond anvil
- Gasket
- Pressure transmitting media
- Pressure calibrant

The basic principle of the DAC is shown in Figure 3.11. When pressure is applied by forcing the diamonds together, the gasket gets compressed between the anvils and very high pressure is formed on a sample loaded in the gasket hole filled with a pressure transmitting media.

Diamond anvil cell

There are two reasons to use diamond for anvils : (i) it is the hardest existing material and (ii) considerably transparent to electromagnetic radiation over IR, visible, UV and X-ray (above 10 keV). For Raman spectroscopy and other sensitive optical techniques, diamonds should be selected for low fluorescence.

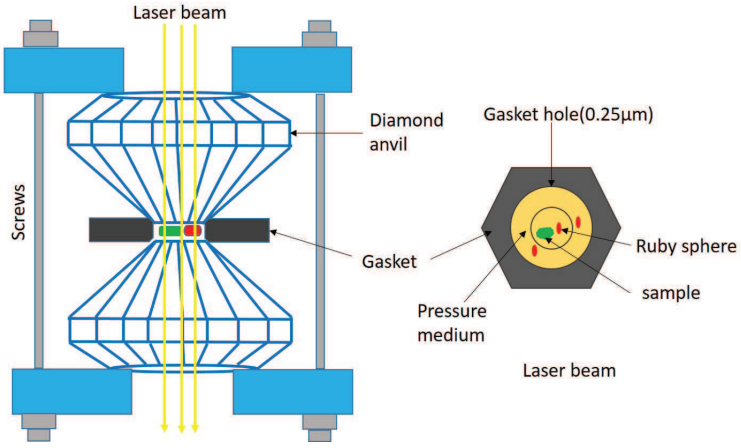

Figure 3.11: Schematic diagram of high-pressure Raman spectroscopy experimental setup.

For high-pressure experiments, diamonds with the brilliant cut (cut of a diamond represents the number and type of facets) have an enlarged culet surface. The maximum pressure is related to the culet diameter (Figure 3.12). The culet-pressure ratio can be calculated, knowing the mechanical properties of diamond and depending on the type of dislocations:

$$\bar{P_0} = 2/(1+2\nu)\sqrt{2\gamma E/\pi(1-\nu^2)c_f}$$

where, $\bar{P_0}$ represents the mean pressure under an indenter before the brittle fracture of diamond, ν is the Poisson ratio, E is the bulk elastic modulus, γ represents the surface energy and c_f is a characteristic size of defects developed [140, 141, 142].

Maintaining proper alignment of diamond anvils is very important to achieve the highest possible pressures. Both anvils must be 100% parallel and have equal coincident diameters. Possible misalignments in any DAC are (1) lateral misalignment (2) angular misalignment. Both of them are demonstrated in Figure 3.13. To adjust the positions of anvils, four screws with micrometer threading are provided in the platens. Therefore the coincidence between both anvils can be easily achieved by adjustment of these four screws [140]. Proper

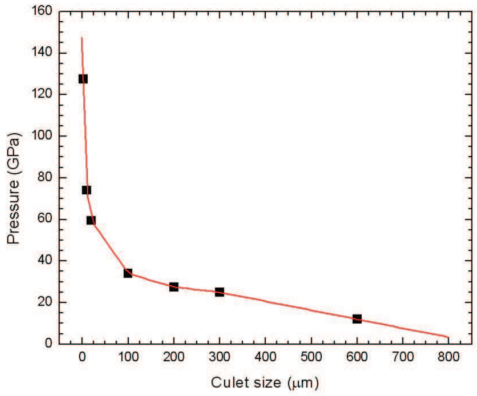

Figure 3.12: Pressure generated in the DAC as a function of culet diameter shows maximal working pressure achievable by respective culet diameters for brilliant cut diamonds(Reprinted from the ref. [4])

alignment checking of two diamond anvils in the cell has been done which is shown in Figure 3.14.

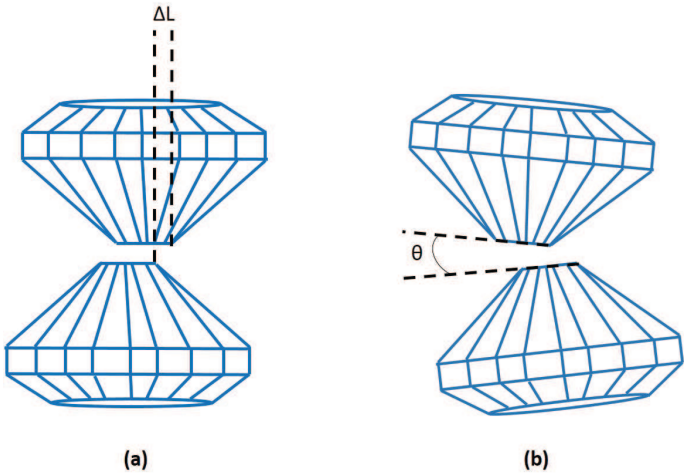

Figure 3.13: (a) Lateral misalignment, (b) Angular misalignment of diamond anvils

High-pressure measurements were performed with EasyLab Diacell Lever-DAC Maxi diamond anvil cell. In this cell high pressure was applied to a sample by forcing two diamond anvils together along the common axis. One diamond was mounted on a plate set into the base of cylinder. The opposing diamond was mounted on a hemisphere which was lapped into a piston. The piston was lapped into the cylinder, the complete assembly being called the “central

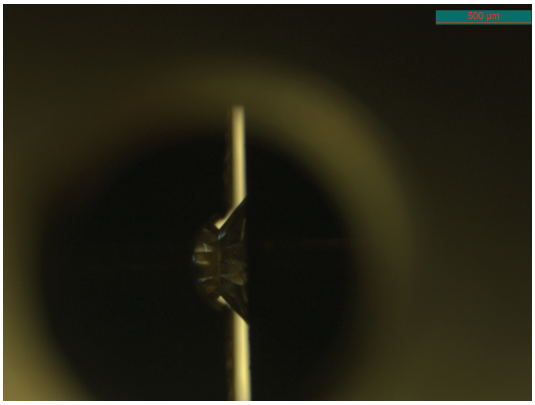

Figure 3.14: Alignment check of two diamond anvils in the cell

insert". The force is generated in the cell by the lever-arm mechanism. Figure 3.15 shows the DAC used for our high pressure investigations.

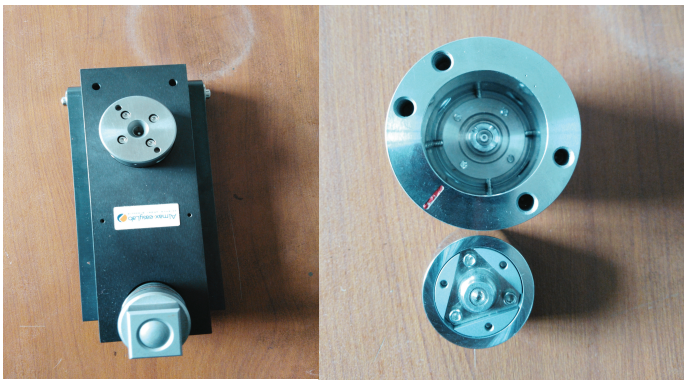

Figure 3.15: EasyLab Diacell LeverDAC Maxi diamond anvil cell

Gasket

The importance of using gasket is to offer an encapsulated chamber in which the pressure transmitting media is confined to apply hydrostatic pressure to the sample crystals. Moreover the gasket isolates two anvils from getting into direct contact during the experiment and prevents them from damage due to the enormous shear forces at the anvil tips. The gaskets are generally prepared from metal foil of thickness 250-300 μm. The materials most commonly used are stainless steel, Ni-Cr-Fe alloy, tungsten or rhenium. Stainless steel gaskets are readily available, cheap and easy to drill while rhenium and tungsten are

more robust and able to withstand experiments in the Mbar range, or high pressure/high temperature experiments. Typically, the initial thickness of the gasket is 200 to 300 μm.

In order to avoid deformation during the compression, gasket is pre-indented between the anvils. After pre-indentation, a hole is formed by drilling at the centre of indentation area and its diameter is chosen according to the culet size. The size of the hole depends on the size of the culets and the type of pressure-transmitting medium. On average, the diameter of the hole should not exceed 60% of the culet diameter. A perfect gasket hole improves the stability of the experiment.

Pressure calibration standard

The pressure measurement in the diamond anvil cell was done using the ruby fluorescence technique. Ruby is a variety of corundum (α–Al_2O_3) doped with trivalent chromium (Cr^{3+}). When corundum is doped with chromium, Cr^{3+} ions substitute Al^{3+}. Cr^{3+} has larger ionic radius than Al^{3+} that leads to a small expansion in the host lattice. Under laser excitation, strong luminescence in the shape of the doublet is observed as R_2 and R_1 lines with wavelengths at 694.25 nm and 692.74 nm respectively (at 300K). Fluorescence is emitted due to electronic transition between ground state $^4A_2$ metastable low energy ^2E excited state of Cr^{3+} in distorted lattice [143, 144].

Ruby does not undergo a phase transition under pressure and room temperature. Under pressure, the ruby doublet exhibits a red shift, which under hydrostatic conditions is linear up to 150 GPa [145]. Pressure can be determined from the wavelength of R_1 line, according to the recalibrated ruby pressure scale by Mao *et al.* (1986) [146]:

$$P = 1904((\lambda(p)/\lambda_0)^B - 1)1/B \tag{3.13}$$

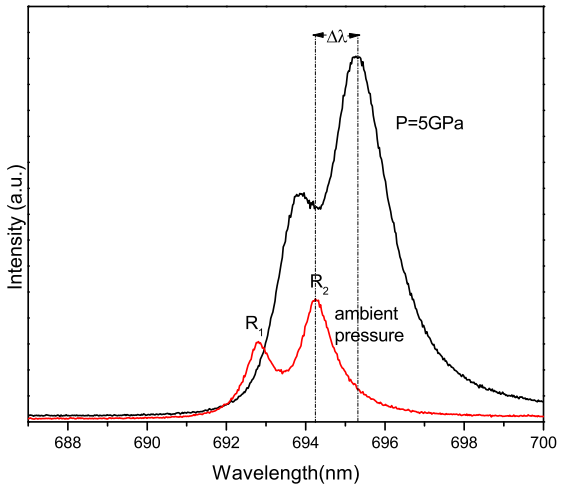

Figure 3.16: Spectrum of the ruby luminescence in the DAC . Ruby R_2-line shifting at high pressure

where λ is the measured R_2 wavelength at pressure P and λ_0 is the position of the R_2 line in ambient conditions, B is an empirically determined coefficient. For hydrostatic conditions B was found to be 7.59 $\pm$ 0.04 cm^{-1}/GPa by Piermarini *et al.* and corrected by Mao to 7.665 $\pm$ 0.04 cm^{-1}/GPa and for non-hydrostatic conditions B was 5 [147, 148]. The precision of the pressure measurement also depends on the size, shape and the degree of crystallinity of ruby crystals. The most commonly used micro-crystal chips have considerable internal elastic strain. The ruby fluorescence spectrum in the DAC at applied pressure is shown in Figure 3.16.

Pressure transmitting media

For high-pressure experiments it is essential to confirm that the force exerted to the sample is homogeneous and that the sample is free of any differential stress or shear strain. For homogenous distribution of pressure, the crystal within the pressure chamber should be immersed in a pressure transmitting medium (PTM) having hydrostatic behaviour. Nonhydrostatic stress leads to significant broadening and shifts in the position of the vibrational peaks from the sample

and can also promote or suppress phase transitions [149, 150].

PTM used for the high pressure experiments can be solid, liquid or gaseous but in any case, they must not react with the sample during the experiment. Usually, alkali-halides (e.g. NaCl) are used as solid pressure media. Hydrostatic pressure produced by this media is realized in a very small pressure region (1 GPa). One of the most commonly used pressure media for high pressure studies is 4:1 methanol:ethanol mixture. which is (quasi)hydrostatic up to 9.8 GPa [6]. When the media is diluted with distilled water so that the methanol : ethanol : water are in the 16 : 3 : 1 ratio, hydrostaticity is increased to 14.5 GPa [7]. Inert gases are reliable to produce good hydrostatic pressure at room temperature. The hydrostatic limit pressures at room temperature were determined to be 16, 2 and 70 GPa for neon, argon and helium, respectively [7]. The reported hydrostatic pressure limit of some commonly used pressure media are tabulated in Table 3.1. In this work the generated pressure was observed on ruby lumines-

Table 3.1: Maximum pressure limit of commonly used pressure media before shear stress overrides quasi-hydrostatic conditions[6, 7, 8]

Medium	Hydrostatic pressure limit (GPa)
Glycerol	1.4
silicon oil	<2.0
Argon	2.0
Water(distilled)	2.2
Nitrogen	3
Isopropanol	3.9
Glycerine: water (3:2)	5.3
Methanol	8.6
Methanol:ethanol (4:1)	9.8
Methanol:ethanol:water (16:3:1)	14.5
Neon	16
Xenon	55
Helium	70
Hydrogen	177

cence peaks using methanol:ethanol (4:1) and methanol:ethanol:water (16:3:1) solution to find suitable pressure media for further experiments (shown in Figure 3.17). When pressure was applied, the ruby immersed in methanol:ethanol

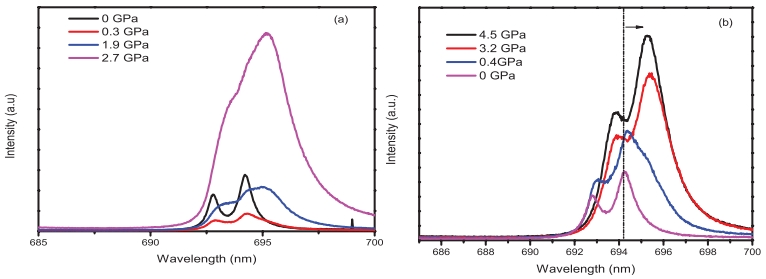

Figure 3.17: Ruby luminescence at different pressure at room temperature using (a) methanol:ethanol (4:1) and (b) methanol:ethanol:water (16:3:1) as pressure transmitting medium

media show R_1 and R_2 lines shifted with large broadening. The broadening of the ruby R_2 line reflects both the inhomogeneous pressure distribution and uniaxial stress pressure. When methanol:ethanol:water mixture was used, ruby R_2 peak shift was observed with very less broadening which signifies homogeneous pressure distribution. To achieve homogeneous pressure distribution in the sample, high pressure study was carried out using methanol:ethanol:water (16:3:1) pressure media.

Instrumentation and experimental conditions used in this study

The high-pressure Raman measurements were performed with the EastLab Diacell LeverDAC Maxi anvil cell equipped with 1 mm diameter culet and stainless steel gasket having 0.25 mm thickness and 0.5 mm diameter hole in it. A mixture of methanol:ethanol:water in the ratio 16 : 3 : 1 was used as the pressure-transmitting medium. Ruby chips were positioned next to the sample and the pressure was evaluated from the shift of the R_1 photoluminescence peak of ruby chips. High pressure Raman measurements were performed using 514.5 nm excitation source with 50X objective.

3.2.4 Ultra-Violet-visible (UV-vis) spectroscopy

Absorption of ultraviolet and visible radiation is related to the excitation of electron in atoms and molecules. When a molecule absorbs UV radiation of

frequency ν, the electron of the molecule transit from lower to higher energy level. When the energy matches the electronic transition within the molecule, a fraction of light energy is absorbed by the molecule and the electrons are promoted from HOMO to LUMO. This results in the absorbance of light. The spectrometer records the degree of absorption by the molecule and provides absorption spectra as a function of wavelength (λ). Absorption wavelength becomes larger when HOMO-LUMO gap is small and vice versa. The absorbance of light by the molecules in the solution is described by Beer-Lamberts law:

$$A = \epsilon bc \tag{3.14}$$

where ϵ is the molar absorbtivity, b is the path length of the sample and c is the concentration of the sample in solution. Molecules undergo four type of electronic transition

1. $\pi \Rightarrow \pi^*$
2. $n \Rightarrow \pi^*$
3. $n \Rightarrow \sigma^*$
4. $\sigma \Rightarrow \sigma^*$

only $\pi \Rightarrow \pi^*$ and $n \Rightarrow \pi^*$ transitions occur in the UV-vis spectral region. The transition between the electronic states is shown in Figure 3.18. UV-vis spectrometer usually consists of:

- Source: Spectrometer has the deuterium lamp and tungsten- halogen lamp as excitation sources. Deuterium lamp emit radiation in UV region while tungsten lamp is useful for visible and Near Infra Red (NIR) measurements.
- Monochromator: As the radiation source enters into the monochromator, the beam is focused onto the diffraction grating and collimated beam is

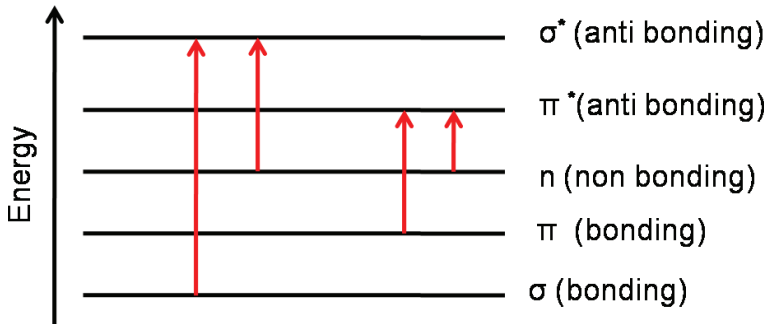

Figure 3.18: Schematic diagram of electronic transition states in a molecule

split into its component wavelengths. Radiation of one particular wavelength is allowed to pass through the slit and splits into two halves as it passes a set of mirrors.

- Sample: Transparent quartz cells are used to hold the sample solution and the reference solvent. After beam splitting,one half passes through the sample cell and the other through the reference cell.

- Detector: Photomultiplier tubes are generally used as UV-vis spectrometer detector where both the beams are fed.

- Computer: The detected information is analysed by the computer to get the output.

Perkin Elmer Lambda 750 spectrophotometer was used for the UV-vis measurements. The samples were prepared in CS_2. For the spectra analysis, absorption peaks were fitted with Gaussian peak profile.

Part III

RESULTS AND DISCUSSION

Chapter 4

Effect of temperature on $Gd@C_{82}$ and $Dy@C_{82}$

4.1 Introduction

In order to understand the metal-cage interactions in EMFs and their spectroscopic, magnetic, and structural properties, the knowledge of electron distribution in the fullerenes is important. When metal is encapsulated into the fullerene cage, charge transfer occurs between the inner species and the cage. Due to thermal stress, charge transfer from the encaged species to the fullerene cage may modify that leads to change in their molecular structure and properties. Temperature-dependent Raman frequencies in $Sc_2@C_{84}$ and $C_2@Sc_2C_{84}$ were done by some research group where moderate peak broadening and temperature-induced peak shifts were reported [92, 151]. It was also reported that in lanthanides (Ce, Yb) doped crystal, the valency of ion varies with temperature and magnetic field [152, 153, 154]. However, variations in intramolecular interactions and the oxidation state of the doped ions in $M@C_{82}$ with temperatures have not well established till date. Any change in the interaction between the metal ion and cage may affect the phonon frequencies, their

line widths, and the thermal conductivity of the fullerene.

In this chapter, the effect of temperature on magnetic and vibration properties of Gd@C_{82} and Dy@C_{82} have been discussed. In addition, we have also presented the thermal conductivity measurements of the thin films of Dy@C_{82} and Gd@C_{82} fullerenes using both temperature and laser-power dependent Raman spectroscopy.

4.2 Temperature effect on oxidation state

In ambient conditions, in Gd@C_{82}, Gd is found in its 3+ oxidation state, transferring three electrons to the C_{82} cage whereas Dy in Dy@C_{82} has the oxidation state between 2+ and 3+ [82, 155]. Gd^{3+} has a half-filled 4f orbital shell. The orbital contribution to the total magnetic moment of the ion is negligible due to zero orbital angular momentum L. On the other hand, Dy@C_{82}, having large orbital angular momentum (L=5) shows ferromagnetic interactions between the metal centers at low temperature. Magnetometry studies have been previously performed on Gd@C_{82} and Dy@C_{82} in the temperature range 2-300 K by other research groups [86, 156].

The magnetization (M) of the particles under the influence of an applied field H can be described by the equation:

$$M = M_s B_J(x) \tag{4.1}$$

where saturation magnetization, $M_s = ngJ\mu_B$. In this study, the experimental isothermal magnetization of Gd@C_{82} and Dy@C_{82}([86]) are fitted with the Brillouin function which is governed by J, total angular momentum, and g, Lande g-factor. The Brillouin function B_J(x) is defined by

$$B_J(x) = \frac{2J+1}{2J} coth[\frac{(2J+1)x}{2J}] - \frac{1}{2J} coth[\frac{x}{2J}] \tag{4.2}$$

n is the number of magnetic ions per unit volume and $x = g\mu_B H/(k_B T)$. The

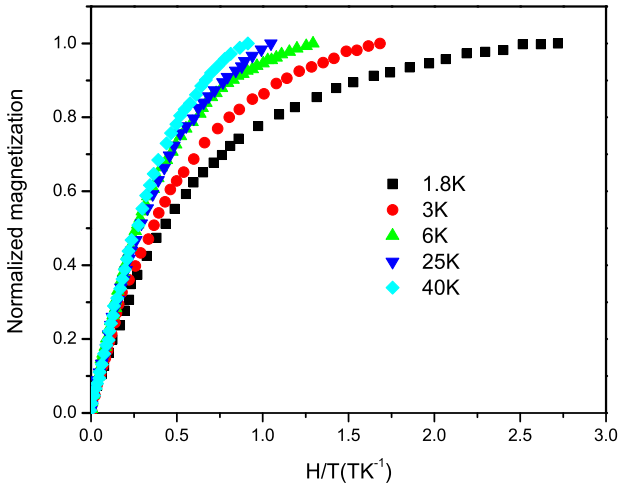

Figure 4.1: Isothermal magnetization as a function of H/T at different temperatures for Gd@C_{82}

normalized magnetization M/M_s as a function of H/T at different temperatures are shown in Figure 4.1 for Gd@C_{82}. In general, for an isotropic paramagnetic material like Gd@C_{82}, g=2 is considered. By fitting the isothermal magnetization data with the Brillouin function $B_J(x)$, total angular momentum J is obtained by using Eq. 4.1 and Eq. 4.2. The obtained J value are plotted at various temperatures(4–300 K) in Figure. It is marked from the Figure 4.2 that J is constant and equals to 3.5 above 15 K for Gd@C_{82} revealing that above 15 K, L=0 and J=S=7/2.

Similarly, isothermal magnetization data of Dy@C_{82} for different temperatures are shown in Figure 4.3 and fitted with Brillouin function B_J(x). The obtained J values for corresponding temperature is shown in Figure 4.4. It is found that J is constant (≈3.7) above 40 K for Dy@C_{82}. When the oxidation state of the ion and hence the charge transfer from the ion to cage changes,the orbital anular momentum (L) and spin angular momentum (S) also vary. This in turn varies the $J(J=L \pm S)$. As the J value is invariant above 15 K for Gd@C_{82} and 40 K for Dy@C_{82}, it indicates that the oxidation states of

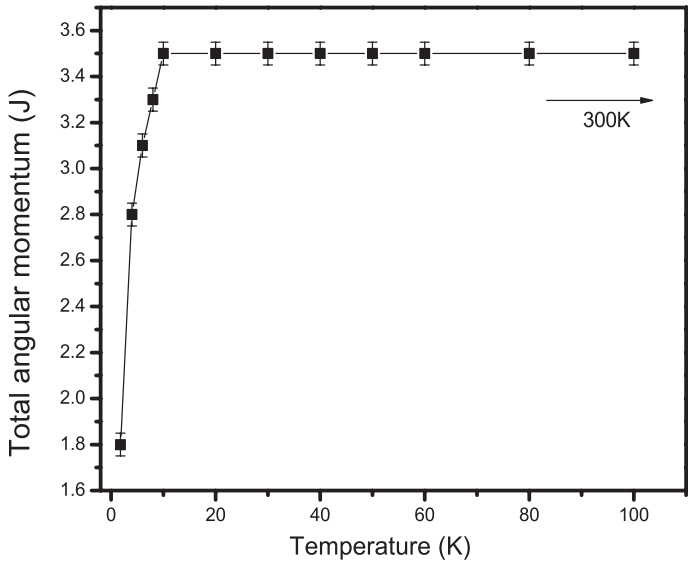

Figure 4.2: Dependence of total angular momentum J of Gd@C_{82} as a function of temperature.

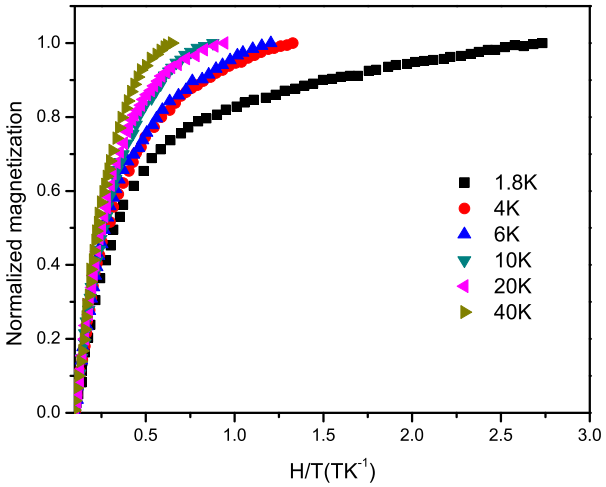

Figure 4.3: Isothermal magnetization as a function of H/T at different temperatures for Dy@C_{82}

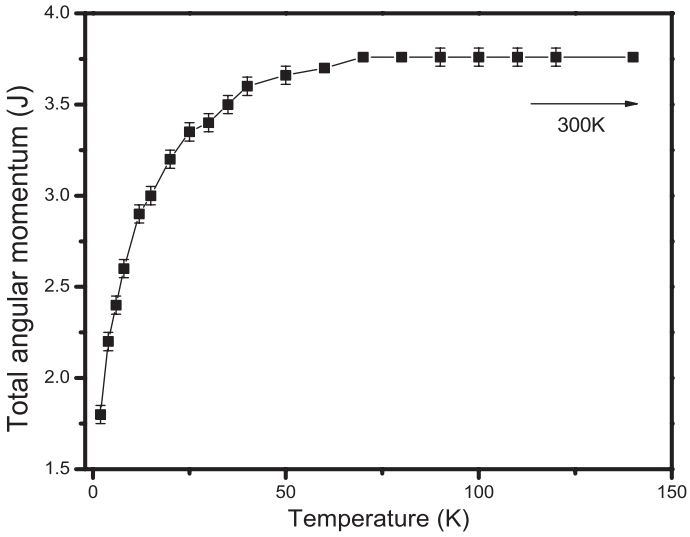

Figure 4.4: Dependence of total angular momentum J of Dy@C_{82} as a function of temperature.

the encaged ions are also invariant above these temperatures. Although the magnetometry studies show no variation in the oxidation states and hence in intra-molecular interactions in these EMFs above 40 K, the inter-molecular interaction is expected to vary under thermal effects. In the later section, thermal effect on inter as well as intra-molecular interactions of Gd@C_{82} and Dy@C_{82} were examined using Raman spectroscopy.

4.3 Thermal effects on Raman spectra

Raman spectroscopy is used to investigate the molecular vibrations by probing the transition between the ground state and the excited vibrational states. The frequency of a transition directly depends on the reduced mass of the atoms involved in the motion. Therefore, smaller the reduced masses leads to higher are the vibrational frequencies. The dependence of the energies of the vibrational states of molecules can be illustrated by the simple harmonic oscillator model [82]:

$$\nu(cm^{-1}) = \frac{1}{2\pi c}(\frac{k}{\mu})^{1/2} \tag{4.3}$$

where k is the force constant (N-cm^{-1}) and μ is the reduced mass of the atoms involved in the motion.

As mentioned before, two kinds of vibrations are reported in the EMFs (a) Raman shifts below 200 cm^{-1} attributed to metal-cage vibrations and (b) Raman shifts above 200 cm^{-1} assigned to the cage internal vibrations. Due to large atomic masses of the metal ions, metal-cage Raman vibrations are expected between 100 to 200 cm^{-1}. General temperature behavior of the Raman frequencies(ν) can be defined as [157, 158]

$$\nu(T) = \nu_0 + \chi_T T + \chi_2 T^2 \tag{4.4}$$

where ν_0 is the frequency at absolute zero and χ_T is the first order temperature coefficient containing thermal expansion and anharmonic contribution to the energy shifts. The higher order coefficients(χ_2) will neglected for the low temperatures thermal analysis as discussed in this work.

In order to understand the observed temperature dependencies of the Raman linewidth, it is necessary to consider the origin of the Raman scattering in terms of phonon-phonon and electron-phonon interactions which limit their lifetimes. In a perfect crystal, the linewidth, Γ, associated with phonon is determined by its interaction with other elementary excitations such as other phonons or electrons. The linewidth can be defined by

$$\Gamma = \Gamma^{ph-ph} + \Gamma^{el-ph} \tag{4.5}$$

where Γ^{ph-ph} is line broadening due to the interaction of the phonon with other phonons (anharmonic phonon–phonon coupling) and Γ^{el-ph} is the linewidth contribution due to with electron/hole (electron-phonon(el-ph) coupling).

Phonon lifetimes can be estimated using full width at half maximum (FWHM) of the Raman peak. Due to increased interaction of the phonons with the other

elementary excitations,the phonon lifetime decreases which results in an increase in FWHM values.

The lattice vibration characteristics of Gd@C_{82} and Dy@C_{82} films were studied by Raman scattering measurements in the temperature 80–300 K. Thermal variation of Raman shifts and the linewidths are examined in the following section.

4.3.1 Thermal effects on Raman spectra of Gd@C_{82}

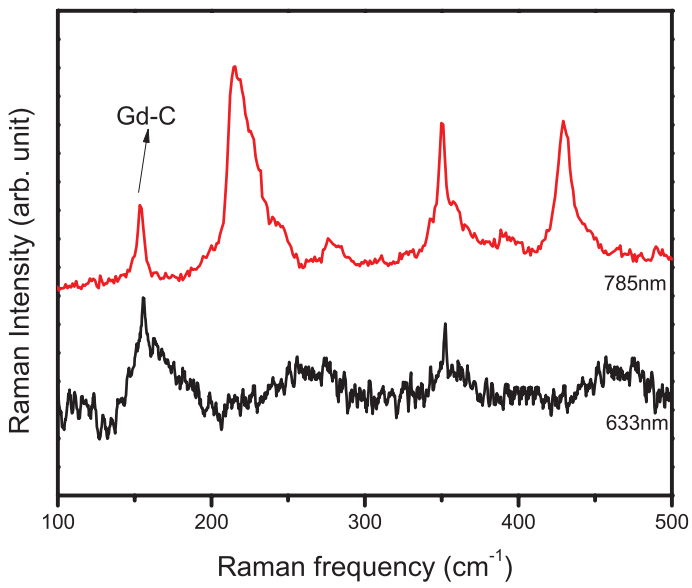

Figure 4.5: Room-temperature Raman spectra of Gd@C_{82} obtained with excitation wavelength 633 nm and 785 nm.

Room temperature Raman spectra of Gd@C_{82} are observed when excited with 633 nm and 785 nm laser. In Figure 4.5, the spectra are illustrated in the energy range 100 and 500 cm^{-1}. When 785 nm laser excitation was used, we obtained four distinct peaks at 154.4(1), 217.3(3), 350.5(1) and 429.7(1) cm^{-1}. Although only two distinct Raman peaks were visible at 155.4(2) and 352.2(1) cm^{-1} when 633 nm laser excitation was used. In both cases, metal-cage vibration of Gd@C_{82} was found near 155 cm^{-1} which is evident from the earlier report [82]. Above 200 cm^{-1} the observed peaks are attributed to cage internal vibrations

in Gd@C_{82}.

To understand thermal effects on metal-cage and C-C interactions in the cage, the temperature dependent Raman spectra of Gd@C_{82} are obtained using 633 nm laser excitation in the temperature range 80-300 K is shown in Figure 4.6. Upon lowering the temperature to 90 K, it was observed that both Raman peaks at 155.4 and 352.2 cm^{-1} were blue-shifted and observed at 163.6(0.5) and 354.8(0.1) cm^{-1}. At 80 K, 352.2 cm^{-1} peak became indistinct and 155.4 cm^{-1} was further blue-shifted to 163.7 cm^{-1}. The thermal variation of the peak positions at 155.4 and 352.2 cm^{-1} are illustrated in Figure 4.7. For 155.4 cm^{-1} peak, the shift in the peak position was approximately +8.3(0.5) cm^{-1} at 80 K whereas the peak at 352 cm^{-1} was shifted by +2.6(1) cm^{-1} at 90 K.

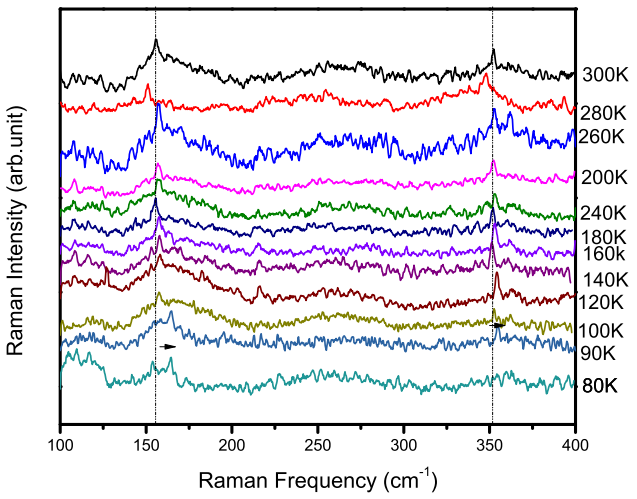

Figure 4.6: Temperature dependent Raman spectra of Gd@C_{82} obtained between 80 and 300 K with excitation wavelength 633 nm.

Low temperature behavior of the Raman frequencies(ν) can be modelled as

$$\nu(T) = \nu_0 + \chi_T T \tag{4.6}$$

The thermal variation of Raman peaks of Gd@C_{82} was fitted with the Eq. 4.6(as shown in Figure4.7) and the fitting parameters ν_0 and χ_T are evaluated

and tabulated in Table 4.1.

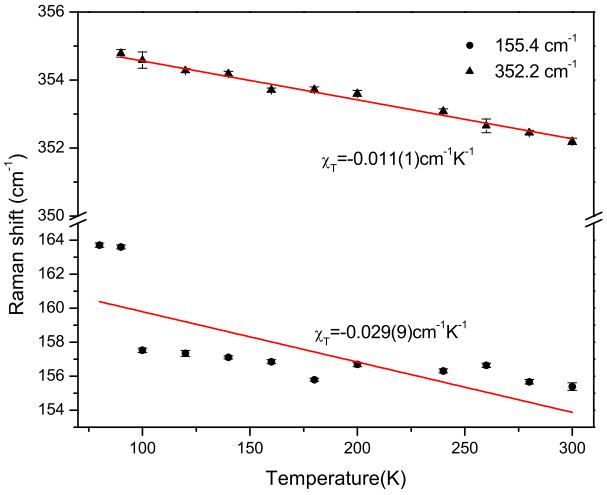

Figure 4.7: Temperature dependent Raman shifts observed at 155.4 cm^{-1} and 352.2 cm^{-1} due to Gd–C and C-C vibrational peaks respectively.

The amount of peak shift determines the energy of the phonon in the material. From Figure 4.7 it is observed that the phonon frequencies are blue-shifted when the temperature is lowered. Temperature affects the population of phonon in different energy levels for each normal mode. If the material lattice experiences compressed stress, blue-shift in Raman frequency is observed, whereas tensile stress red-shifts the Raman frequencies [159, 160]. Compression/expansion in lattice modifies the bond strength, hence force constant (k) changes. Considering a simple harmonic oscillator model for Gd–C_{82} , k is calculated using Eq.4.3 and plotted in Figure 4.8 as a function of temperature. The reduced mass of Gd@C_{82} is 135.6 a.m.u. At room temperature k for Gd–C_{82} is found to be 1.9 N-cm^{-1}. Upon lowering temperature to 90 K the k value increased to 2.1 N-cm^{-1}. The force constants signify the nature and strength of the metal-cage interaction, which depend on the oxidation state of the incarcerated ion and the charge transfer between the ion and cage [161]. Although in the observed temperature region no significant change was found in the oxidation state of encaged Gd ion (see Figure 4.2), increase in force

constant of Gd–C_{82} bond could be due to thermal effects. Hence, the observed blue-shifts in both metal-cage and cage internal peaks of vibration were credited to thermal contraction of the cage. Giefers *et al.* have also illustrated X-ray absorption analysis that in Gd@C_{82}, the metal-ion distance with temperature and distortion in the local environment of the Gd ion near carbon hexagons are observed at low temperatures [156].

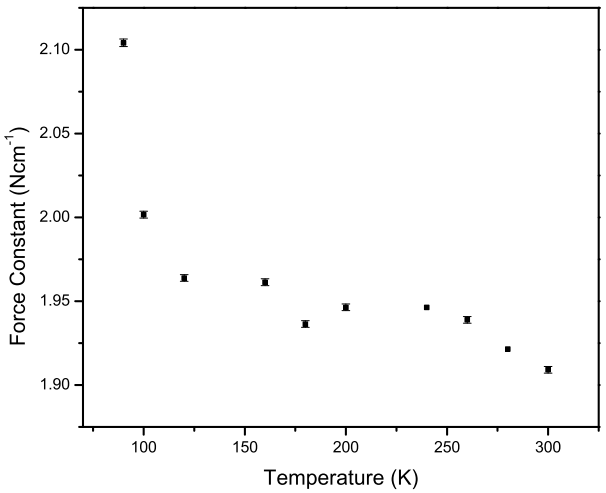

Figure 4.8: The force constants variation with temperature for Gd–C_{82} interaction.

The thermal interaction affects phonon mean free path and phonon decay lifetime which in turn affects the phonon energy and linewidth in the Raman spectra. As the experiment was performed at constant pressure, both anharmonic phonon contribution and crystal thermal expansion are considered to be responsible for the observed variation in phonon frequencies with temperature. Temperature dependent FWHM of Gd–C (155.4 cm^{-1}) and C-C (352.2 cm^{-1}) vibrational peaks in Gd@C_{82} are shown in Figure4.9(a). At room temperature, the linewidth of 352.2 cm^{-1} peak is observed to be 1.7(3) cm^{-1}. It is evident from the plot that the linewidth is nearly temperature independent whereas that of 155.4 cm^{-1} peak reduces with temperature. The corresponding Raman peaks were fitted with Lorentzian profile. The variation of linewidth $\Gamma(T)$ with

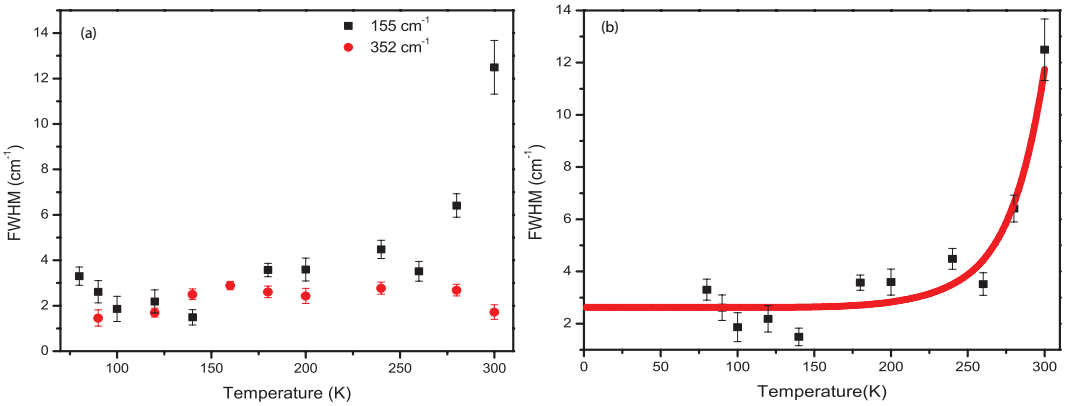

Figure 4.9: (a) Temperature dependent FWHM of 155, 352 cm^{-1} peak of $Gd@C_{82}$. (b) The temperature variation of FWHM of Gd–C vibrational peak (155 cm^{-1}) along with the fit of the data.

temperature can be governed by the anharmonic decay of phonons that was discussed in details in Chapter 2. The thermal variation in the linewidth of 155.4 cm^{-1} peak is fitted with the following equation [162]:

$$\Gamma^{ph-ph}(T) = \Gamma_0^{ph-ph} + C\left[1 + \frac{2}{\exp(\frac{\hbar\nu_0}{2k_BT}) - 1}\right] + D\left[1 + \frac{3}{\exp(\frac{\hbar\nu_0}{3k_BT}) - 1} + \frac{3}{(\exp(\frac{\hbar\nu_0}{3k_BT}) - 1)^2}\right] \tag{4.7}$$

where $\Gamma(0)$ is temperature-independent FWHM and C and D are the cubic and quartic anharmonic constants. The second and third terms of the Eq. 2.8 are the contribution of cubic and quartic anharmonicities, respectively. The observed linewidth $\Gamma(T)$ of 155.4 cm^{-1} as a function temperature is shown in Figure 4.9. When the FWHM as a function of temperature is extrapolated to absolute zero (T→0 K), it converges to 2.6(2) cm^{-1}($\Gamma(0)$). At higher temperatures, the FWHM increases with temperature. Only above 200 K, the anharmonic effects in peak broadening were evident. C and D are evaluated as 0.17(4) and 2.9(7) cm^{-1}, respectively. The reduced linewidth could be associated with the freezing of cage at low temperatures which in turn strengthens the interaction between the Gd ion and cage and also reduces the anharmonic

phonon decay.

4.3.2 Thermal effects on Raman spectra of Dy@C_{82}

Room temperature Raman spectra of Dy@C_{82} performed with 633 nm and 785 nm excitation sources are shown in Figure 4.10. Three distinct peaks are observed at 151.1(2), 216.7(2) and 471.3(5) cm^{-1} using 785 nm laser. While using 633 nm excitation, we observed the peaks at 151.5(1), 219.4(1), and 470.9(3) cm^{-1}. In addition to these, a weak peak at 215 cm^{-1} is also observed in Dy@C_{82}. The temperature dependent Raman spectra of Dy@C_{82} are studied

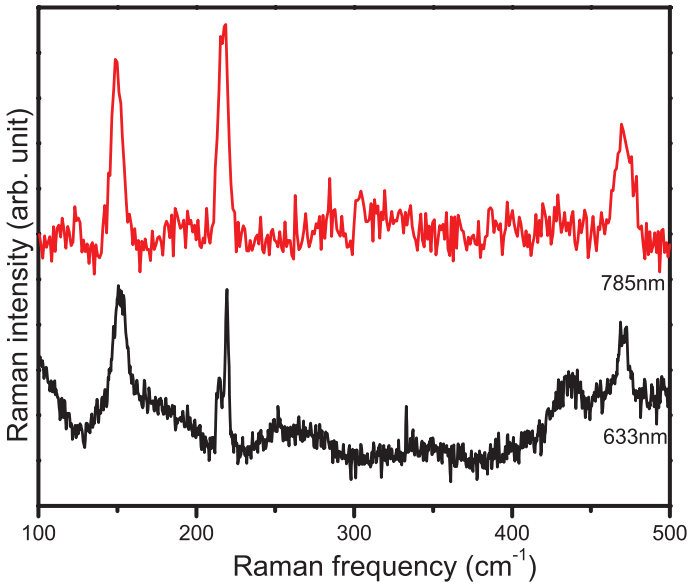

Figure 4.10: Room-temperature Raman spectra of Dy@C_{82} obtained with excitation wavelength 633 nm and 785 nm.

using 633 nm excitation source and in the temperature range 80-300 K is shown in Figure 4.11. While the temperature was decreased to 100 K, all Raman peaks of Dy@C_{82} are blue-shifted and were observed at 153.8(5), 220.6(1), and 473.0(4) cm^{-1}, respectively. At 80 K, only two peaks are continued to blue-shift at 154.5(8) and 220.6(3) cm^{-1}. At 80 K, 470.9 cm^{-1} peak became indistinct due to line broadening. The thermal variation of the peak positions at 151.5, 219.4, and 470.9 cm^{-1} are illustrated in Figure 4.12. For 151.5 cm^{-1} and 219.4 cm^{-1}

peak, the shift in the peak position is approximately +3.0 cm^{-1} and +1.2 cm^{-1} at 80 K; whereas the peak at 470.9 cm^{-1} is shifted by +2.1(1) cm^{-1} at 100 K. The thermal variation of Raman peaks of Dy@C_{82} is fitted by the Eq. 4.6 and the fitting parameters ν_0 and χ_T are tabulated in Table 4.1.

Considering a simple harmonic oscillator model for Dy–C_{82}, k was calculated using Eq. 4.3 and plotted in Figure 4.13 as a function of temperature.The reduced mass of Dy–C_{82} was 139.5 a.m.u. We obtained k of Dy–C_{82} as 1.88 N-cm^{-1} at room temperature whereas at 80 K, the k value increases to 1.95 N-cm^{-1}. Increase in force constant has increased at low temperature signifies thermal contraction in the molecule. Contraction of cage and distortion in the local environment of the Dy ion gave rise to blue-shifts in all resulting phonon frequencies.

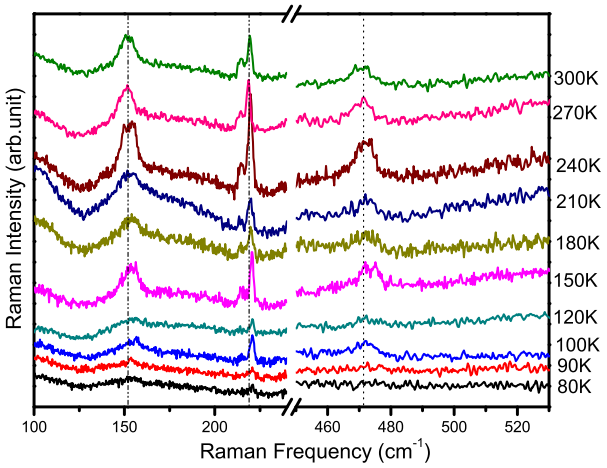

Figure 4.11: Temperature dependent Raman spectra of Dy@C_{82} obtained between 80 and 300 K with excitation wavelength 633 nm.

Temperature dependent FWHM of 151.5, 219.4, and 470.9 cm^{-1} peaks in Dy@C_{82} are shown in Figure 4.14(a). At room temperature, the linewidths are found to be 2.3(2) cm^{-1} and 6.2(4) cm^{-1} for 219.4 cm^{-1} and 470.9 cm^{-1} peaks, respectively. From Figure 4.14(a), it is evident that their linewidths are nearly temperature independent, whereas FWFM of 151.5 cm^{-1} peak increased when

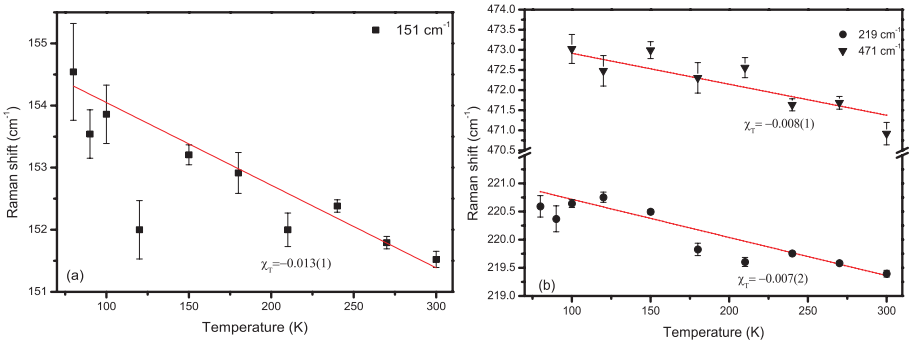

Figure 4.12: Temperature dependent Raman peak shifts observed at (a) 151 cm^{-1} and (b) 219 cm^{-1} and 471 cm^{-1} due to Dy–C and C-C vibrational peaks respectively.

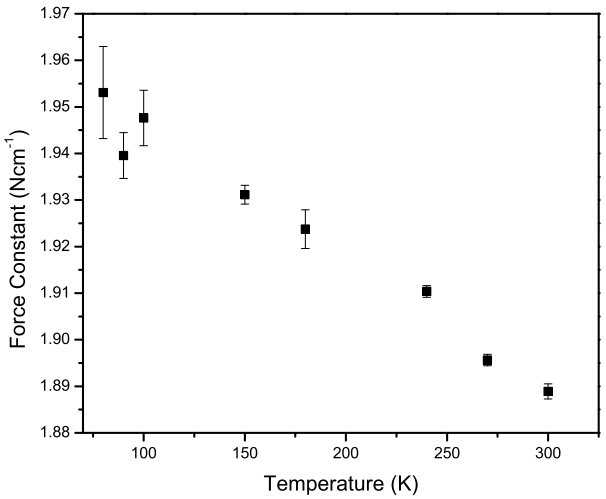

Figure 4.13: The force constants variation with temperature for Dy–C_{82} interaction.

the temperature is lowered. The linewidth of a phonon in a crystalline lattice is determined by its interaction with other elementary excitations. In most of the materials temperature dependent line-broadening occurs due to anharmonic effects and phonon–phonon interaction which can be written as[163, 164]:

$$\Gamma^{ph-ph}(T) = \Gamma_0^{ph-ph}[1 + \frac{2}{\exp(\frac{\hbar\nu_0}{2k_BT}) - 1}] \tag{4.8}$$

where Γ^{ph-ph}(T) is the temperature dependent linewidth arising due to anharmonic phonon–phonon coupling and Γ_0^{ph-ph} is the temperature independent

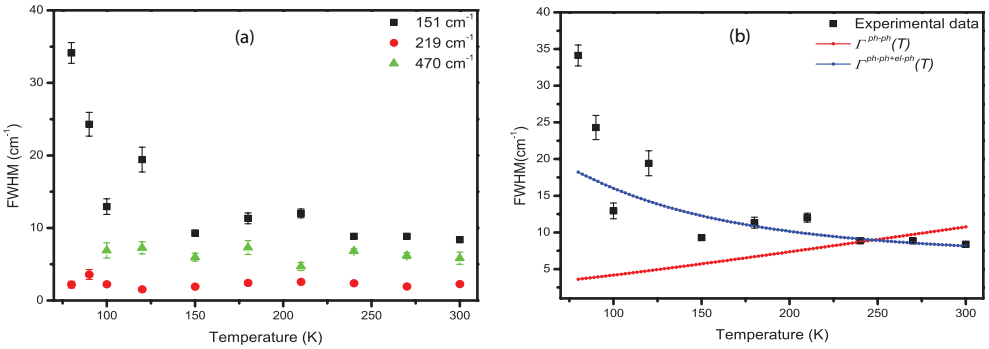

Figure 4.14: (a) Temperature dependent FWHM of 151.5, 219.4 and 470.9 cm^{-1} peak of $Dy@C_{82}$. (b) The temperature variation of FWHM of Dy–C vibrational peak (151.5 cm^{-1}) along with the fit of the data which includes both phonon-phonon and electron-phonon coupling in the line broadening.

linewidth. We attempted to fit the temperature dependent FWHM of 151 cm^{-1} peak considering anharmonic phonon–phonon coupling only which is shown in Figure 4.14(b). At low temperatures Γ^{ph-ph}(T) did not fit well with the experimental data revealing that other elementary excitations such as electrons, holes or electron-hole pairs might be interacting with the phonons. This is why we have redefined the thermal variation of FWHM by taking both phonon-phonon and electron-phonon contribution in the temperature dependent Dy-C Raman line broadening. The linewidth due to electron-phonon interaction ($\Gamma^{el-ph}(T)$) is given by [165, 166, 167, 168]

$$\Gamma^{el-ph} = \Gamma_0^{el-ph}[\frac{1}{\exp(-\frac{\hbar\nu_0}{2k_BT})+1} - \frac{1}{\exp(\frac{\hbar\nu_0}{2k_BT})+1}] \tag{4.9}$$

where Γ_0^{el-ph} is the linewidth due to electron-phonon coupling at 0 K. $\Gamma(T)$ is used to fit the experimental data and is shown in Figure 4.14b. The fitting parameters Γ_0^{ph-ph} and Γ_0^{el-ph} are found to be 0.5(3) cm^{-1} and 31(6) cm^{-1} respectively. Having $\Gamma_0^{el-ph} >> \Gamma_0^{ph-ph}$ revealed that at low temperatures electron-phonon coupling dominated over phonon-phonon coupling and thus broadens the peak attributed to Dy-C vibration. At low temperatures, the thermal excitation of the electrons is overpowered by the generation of electron-hole pairs

via phonon excitation. This in turn, decreases the phonon lifetime and results in line broadening [165, 169].

4.3.3 Discussion

Thermal variations in the Raman frequencies give negative temperature coefficients for both metal-cage and cage internal vibration in Gd@C_{82} and Dy@C_{82}. Negative χ_T arises due to the thermal expansion (pure volume) of the cage and anharmonicity(pure temperature) in the lattice forces as discussed in Chapter 2 [170, **?**]. Their contribution influences the bond length and the interatomic interaction upon thermal variation. From the Table 4.1 it is observed that χ_T

Table 4.1: Temperature dependent frequency coefficients(χ_T) of different peaks of EMFs

Sample	Raman position(cm^{-1})	χ_T ($cm^{-1}K^{-1}$)	ν_0 (cm^{-1})
Gd@C_{82}	155.4	-0.029(9)	162.7(1.1)
	352.2	-0.011(1)	355.7(1)
Dy@C_{82}	151.5	-0.013(1)	155.4(6)
	219.4	-0.007(2)	221.4(2)
	470.9	-0.008(1)	473.7(4)

for C_{82} cage vibrations (C–C) are similar irrespective of the encaged metal ion. To understand the temperature dependence of cage internal vibrations(C–C), χ_T of M@C_{82} are compared with other carbon nanostructures. χ_T of radial breathing modes of CNTs(0.006-0.13 cm^{-1}/K) are found to be similar to C_{82} cage internal vibration [157]. Due to the covalent bond between carbon atoms in carbon nanotube rings and fullerenes, bending strain energy is high which makes temperature induced softening of the C–C bond difficult. As the ionic interaction is exerted between encaged metal ion and the fullerene cage due to the charge transfer, χ_T of metal-cage vibration was found to be higher than that of cage internal vibrations. As the ionic radius of $Gd^{3+}(0.938\mathring{A})$ is larger than that of $Dy^{3+}(0.912\mathring{A})$, Gd–C suffers stronger compression than Dy–C in the rigid cage [171, 172, 173]. This is also visible from the force constant values.

Larger force constant of Gd-C_{82} is ascribed to more compression in Gd-C bond which results higher χ_T of Gd–C vibration than Dy–C mode.

The linewidth of C_{82} cage vibrations are nearly temperature independent, which suggests the presence of negligible anharmonic contributions in cage internal vibrations. Unlike C_{82}, the metal-cage vibration show temperature dependent linewidth variation suggesting presence of anharmonic contributions and interaction of phonon with other elimentary excitations Linewidth of Gd-cage vibration is the result of purely phonon-phonon interaction. Whereas, Dy-C line broadening is attributed to the contributions from both phonon-phonon and electron-phonon interactions. At low temperatures, electron–phonon coupling dominates over phonon–phonon coupling and influences the Dy–C line broadening.

4.4 Effect of laser power on Raman spectra

During Raman measurements, the sample absorbs some of the incident radiation and eventually heats up. The temperature rise depends on quantities such as the thermal conductivity of the material, laser power and irradiation time. Local heating effect of the sample due to the laser beam in Raman measurements encouraged us to perform laser-power-dependent Raman spectroscopy. The Raman frequencies are related to the laser power by the following equation[109]

$$\nu(L_2) - \nu(L_1) = \chi_L(L_2 - L_1) \tag{4.10}$$

where χ_L is the first order power coefficient. $\nu(L_1)$ and $\nu(L_2)$ are phonon frequencies at the applied power L_1 and L_2.

Laser power dependent Raman spectra of Dy@C_{82} and Gd@C_{82} have been obtained at room temperature using 785 nm excitation and are discussed in the following section.

4.4.1 Effect of laser power on Raman spectra of Gd@C_{82}

Raman spectra of Gd@C_{82} are also studied by varying power 0.15-15 mW. Power dependent Raman spectra are shown in Figure 4.15. At laser power of 0.15 mW, the Gd-cage vibration and C-C vibrations are observed at 154.4 cm^{-1}, 217.2 cm^{-1} and 350.5 cm^{-1}. When the laser power is increased to 3 mW, the peak at 154.4 cm^{-1} is linearly shifted to 153.6(1) cm^{-1}. Above 3 mW, nonlinear peak shift is observed in the metal–cage vibrational peaks. Upon increasing the laser power to 15 mW, 217.2 cm^{-1} and 350.5 cm^{-1} peaks shifted to 216.1(1) cm^{-1} and 348.9(4) cm^{-1}. Laser power leads to increase the sample temperature which affect in their vibrational frequency. Due to the presence of free charge distribution, metal-cage vibration are more sensitive to temperature. Thus, higher order temperature coefficient results in non-linear peak shift above 3 mW. The Raman shift with the laser power was fitted with Eq.4.10 and the respective χ_L is evaluated. The shift in the observed Raman frequencies as a function of laser power is shown in Figure 4.16. The fitting parameter χ_L for corresponding phonon frequencies are tabulated in Table 4.2.

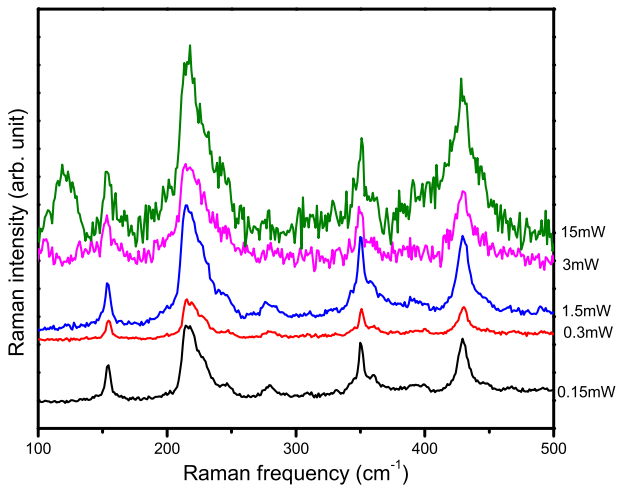

Figure 4.15: Laser power dependent Raman spectra of Gd@C_{82} using 785 nm excitation.

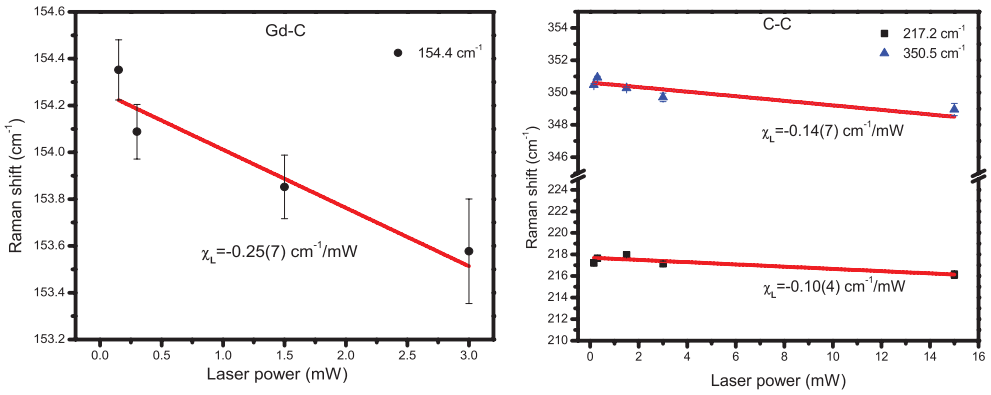

Figure 4.16: Laser power dependent Raman peak shift for Gd–C (154.4 cm^{-1}) and C–C peaks in Gd@C_{82}.

4.4.2 Effect of laser power on Raman spectra Dy@C_{82}

Raman spectra of Dy@C_{82} are studied by varying power 0.15-15 mW. Power dependent Raman spectra are shown in Figure 4.17. At laser power of 0.15mW, the metal-cage vibration and C-C vibration were observed at 151 cm^{-1}, 216.7 cm^{-1} and 471.3 cm^{-1}. When the laser power is increased to 3 mW, the peak at 151 cm^{-1} was linearly shifted to 150.6(2) cm^{-1}. Above 3 mW, nonlinear peak shift was observed in the metal–cage vibrational peaks. Upon increasing the laser power to 15 mW, the peak at 216.7 cm^{-1} and 471.3 cm^{-1} shifted to 215.1(2)cm^{-1} and 470.4(4) cm^{-1} respectively. The shift in the observed Raman frequencies as a function of laser power was fitted by Eq.4.10 and is shown in Figure 4.18. It is evident that the increase in the laser power locally heats the fullerenes that leads to red-shift in the observed frequencies. The fitting parameter χ_L for corresponding phonon frequencies are tabulated in Table 4.2.

As the laser power is associated to the heating effects of the excitation source, all Raman vibrations are observed to be red-shifted. For cage internal vibrations, similar χ_L are obtained for both EMFs that could be attributed to the presence of same fullerene cage C_{82}. like χ_T, χ_L of metal-cage vibration are found to be larger than the cage internal vibration. Non-linearity in metal-

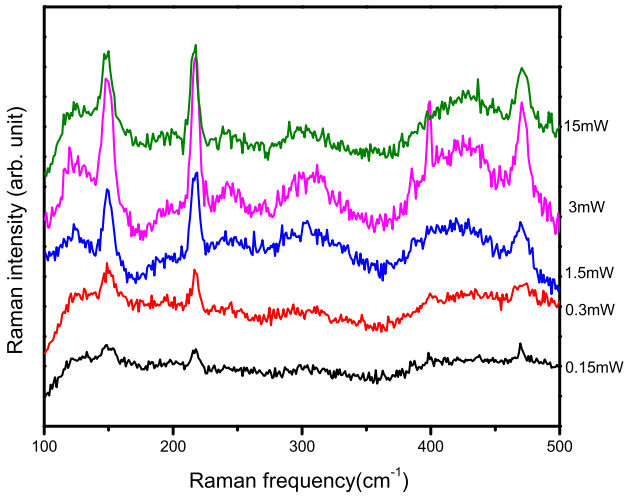

Figure 4.17: Laser power dependent Raman spectra of (a) Dy@C_{82} using 785 nm excitation.

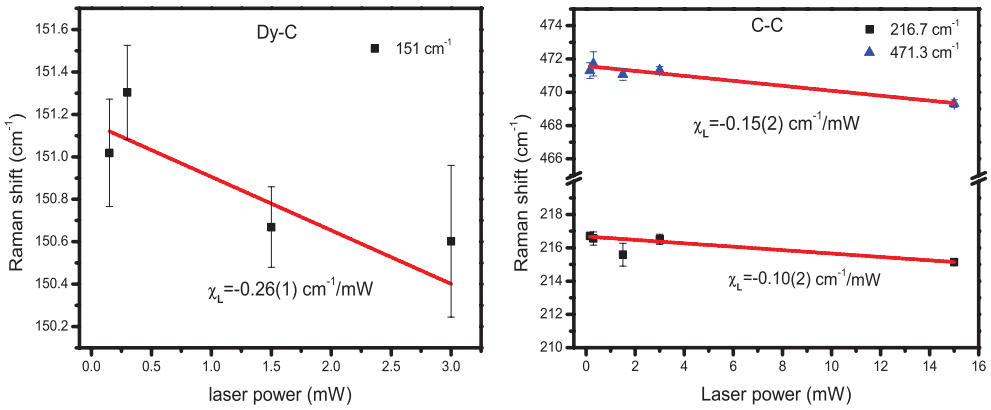

Figure 4.18: Laser power dependent Raman peak shift for Dy–C and C–C peaks in Dy@C_{82}.

cage peak shift above 3 mW indicates strong temperature dependency of the metal-cage vibration. χ_L of Gd–cage vibration was found to be similar to Dy–Cage vibration. This could be ascribed to the dominance of phonon–phonon interaction at high temperature in both EMFs.

Table 4.2: Power dependent frequency coefficients(χ_L) of different peaks of EMFs

Sample	Raman position(cm^{-1})	χ_L ($cm^{-1}mW^{-1}$)
Gd@C_{82}	154.4	-0.25(7)
	217.2	-0.10(4)
	350.5	-0.14(7)
Dy@C_{82}	151	-0.26(1)
	216.7	-0.10(2)
	471.3	-0.15(2)

4.5 Thermal conductivity

In this thesis, we considered steady state method to determine thermal conductivity where optothermal Raman measurement technique was used. Considering the temperature rise due to the absorbed energy at the laser spot on the sample, the thermal conductivity of the film can be derived with the heat transfer model. When the film thickness is at least one order larger than the laser diameter, hemispherical distribution of heat flow is followed. *Stobib et al.* considered the Gaussian heat distribution profile and used the following equation to estimate κ[115]:

$$\kappa = \frac{L}{\sqrt{\pi} d_0 \Delta T} \tag{4.11}$$

where a Gaussian profiled laser beam having d_0 as $1/e^2$ width is used to generate the heat flux. The Gaussian beam profile of 785 nm laser was shown in Chapter 3 where d_0 was obtained as 7.7 μm. Temperature rise $\Delta T = T_R - T_b$ is the difference between bulk sample temperature(T_b) and local temperature on the surface(T_R) due to the heating effects by the laser power L. The detailed derivation of the relationship between the measured temperature rise and the thermal conductivity was described in Chapter 2. In this work, we have estimated the thermal conductivity of Gd@C_{82} and Dy@C_{82} films by using Eq. 4.11.

Molecular dynamics simulations of C_{60} crystals suggested that the thermal conduction is mostly contributed by the low frequency acoustic phonons which arise due to intermolecular interaction [1]. However this frequency regime is considered below 100 cm^{-1}. The thermal conductivity of the thin-films was reported nearly independent of the carrier frequencies[174]. In order to examine the spectral contributions to the heat conduction hence thermal conductivity, all observed phonon frequencies of Gd@C_{82} and Dy@C_{82} were considered. Temperature rise was calculated from the first order temperature coefficient of phonon frequencies along with laser power dependent frequency shift of the corresponding peak. As the thermal variation in the Raman frequencies is linear, its slope χ_T and the laser-power dependent shifts in the Raman frequencies are utilized for evaluating ΔT of the samples. Temperature relation with Raman frequencies are given by [175]:

$$\Delta T = \frac{\nu(L_2) - \nu(L_1)}{\chi_T} \tag{4.12}$$

In Gd@C_{82}, κ near room temperature and ΔT were calculated for 155 cm^{-1} and 352 cm^{-1}. The estimated κ using Eq. 4.11 and are tabulated in Table 4.3. Similarly, κ near room temperature was determined for 151 cm^{-1} and 470 cm^{-1} peak in Dy@C_{82} and the corresponding values are reported in Table 4.3. Thermal conductivity was calculated at 1.5 mW, as we observed small temperature rise in the films and reported the values as near room temperature thermal conductivity. We have also observed the spectral contribution of thermal con-

Table 4.3: Thermal conductivity(κ)at their corresponding temperatures (T) of different peaks of EMFs

Sample	vibration	Raman position (cm^{-1})	T_R (K)	κ ($Wm^{-1}K^{-1}$)
Gd@C_{82}	Gd–C	154.4	315.7	4.8(5)
	C–C	350.5	311	1.8(4)
Dy@C_{82}	Dy–C	151	319.3	2.3(3)
	C–C	471.3	325.8	1.2(3)

ductivity of metal-cage and C-C vibration from both samples shown in Figure 4.19. The contribution of higher phonon frequencies was found smaller than the lower phonon frequencies for both the samples.

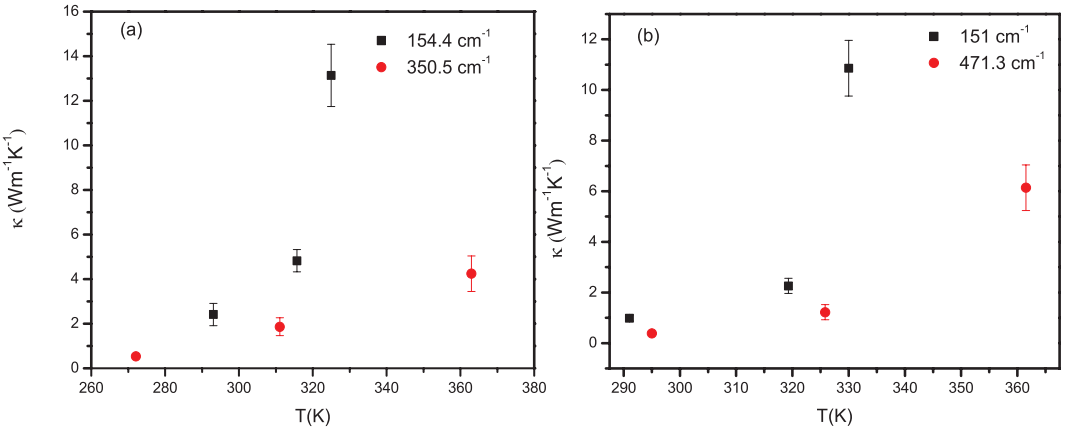

Figure 4.19: (a)Thermal conductivity at different temperatures for 154 cm^{-1} and 350 cm^{-1} peaks in Gd@C_{82}.(b)Thermal conductivity at different temperatures for 151 cm^{-1} and 471 cm^{-1} peaks in Dy@C_{82}.

In nanomaterials, the localization of vibrations and the reduced phonon mean free path contribute to low TC [176, 177, 178, 179]. It was observed that κ values of EMFs were higher than those reported for the thin films of C_{60}, C_{70}, carbon nanospheres and amorphous carbon(0.2-0.9 $Wm^{-1}K^{-1}$) [1, 180, 181, ?]. However, they are much smaller (nearly three orders of magnitude) as compared to that of graphene, graphite and carbon nanotubes [99, 170, 182]. In pristine fullerenes, κ has mostly phonon contributions where the heat conduction occurs via lattice vibrations of covalently bonded carbon atoms. However, fullerenes doped with lanthanides such as Dy@C_{82} and Gd@C_{82} may also have an additional electron contribution to κ due to the presence of free charge carriers which leads to their larger thermal conductivity.

4.6 Conclusion

In this chapter, the thermal effects on lattice vibration of EMF films is examined. The oxidation states of the encaged metal ion as a function of temperature

is observed from the magnetometry study and Brillouin function approach. No change in the oxidation state of Gd and Dy ion is observed above 15 K and 40 K respectively. Temperature dependent Raman spectra of Gd@C_{82} and Dy@C_{82} are performed to study their lattice dynamics. The observed blue-shifts in both metal-cage and cage internal vibrations while lowering the temperature show thermal expansion as well as anharmonic effects in the EMFs. Linewidth of Gd–cage vibration is the contribution from purely phonon-phonon interaction and decrease in linewidth at lower temperatures occurs due to reduced anharmonic effects. Raman peak broadening in Dy-cage vibration was assigned to the contributions from both phonon–phonon and electron–phonon interactions. At low temperatures, domination of electron–phonon coupling over phonon–phonon coupling leads to broadening in Dy–cage vibrational frequency. However, negligible anharmonic contribution was observed in linewidths of cage internal vibrations.

Thermal conductivity of Gd@C_{82} and Dy@C_{82} films are estimated by using the combinational effect of temperature and laser power on observed phonon frequencies. Thermal conductivity was observed to be dependent on phonon frequencies. For both metal–C and C–C vibrations, the contribution of higher phonon frequencies are less as compared to lower phonon frequencies. The thermal conduction in these rare earth doped fullerenes at room temperature and above is mainly attributed to the anharmonic coupling of lattice vibrations. Presence of free charge carriers and additional electron contribution leads to higher κ value of EMFs than those of empty fullerenes.

Chapter 5

Effect of temperature on $C_{60}O$ and $C_{70}O$

5.1 Introduction

Under thermal stress, fullerene conformation and its interaction with the neighboring molecules vary which can affect its lattice dynamics. C_{60} experiences first order orientational transition at 260 K where its fcc structure is transformed to sc structure [29]. From the reported temperature dependent FTIR and Raman spectra of C_{60} and C_{70}, vibrational linewidth was found to be proportional to temperature which arises due to the freezing out of rotational motion [183]. In fullerene oxides, addition of a single oxygen atom provides a small perturbation to the molecular structure which alters its molecular interaction. Similar to that of C_{60}, $C_{60}O$ showed an orientational transition at 278 K[184]. Although $C_{60}O$ has similar structure as that of C_{60}, a slight modified lattice dynamics is expected due to the presence of oxygen.

In Chapter 4, Raman spectroscopy was used to study the lattice dynamics of EMFs as a function of temperature. In this chapter we have discussed the thermal effects on the Raman vibrational frequencies for understanding the inter

and intra-molecular interactions in two exohedral fullerenes, photo-polymerized $C_{60}O$ and $C_{70}O$. Raman spectroscopic technique was also used to evaluate their thermal conductivities.

5.2 Optical property of photo-polymerized $C_{60}O$

5.2.1 UV-vis spectral analysis

UV-vis absorption spectra provide preliminary information about the nature of compounds present. The UV-vis absorption spectrum of pristine C_{60} and photo-polymerized $C_{60}O$ in CS_2 at room temperature are shown in Figure 5.1. The spectra are taken in the wavelength region 400-700 nm. In pristine C_{60}, absorption bands are observed at 410.1(2), 545.5(6) and 599.7(3) nm. In the photo-polymerized $C_{60}O$, a new weak absorption band is observed at 423.6(2) nm which signifies the presence of oxygen in C_{60} [42]. Due to some traces of C_{60}, we have also observed 410.6 nm absorption band. In addition, near 546.8 nm and 607.5 nm bands are observed in $C_{60}O$ which are red shifted by 1.3 nm and 7.8 nm from that of pristine C_{60}. Larger absorption wavelength in $C_{60}O$ suggests that band gap of C_{60} is reduced in presence of oxygen. As compared to C_{60}, $C_{60}O$ showed weaker absorption near 546.8 nm and 607.5 nm of $C_{60}O$ illustrating that the yield is less.

5.2.2 Raman spectral analysis

The room temperature Raman spectrum of photo-polymerized $C_{60}O$ is illustrated in Figure 5.2. In C_{60}, three Raman peaks at 273, 497 and 1469 cm^{-1} are previously assigned to H_g squashing mode, A_g breathing mode and A_g pentagonal pinch mode, respectively [52, 55]. The vibrational peaks of $C_{60}O$ are seen in the same characteristic regions as that of the pristine C_{60}, however the peaks are observed split as well as shifted due to the reduced symmetry of

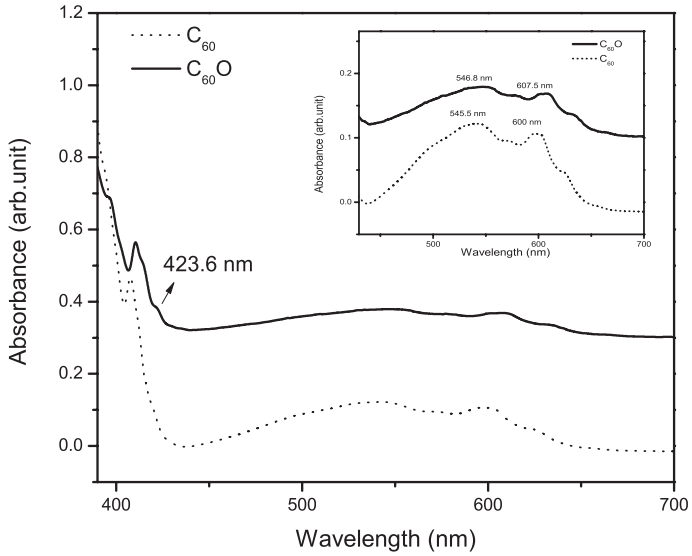

Figure 5.1: Room temperature UV-vis spectra of pristine C_{60} and photo-polymerized $C_{60}O$ dissolved in CS_2.

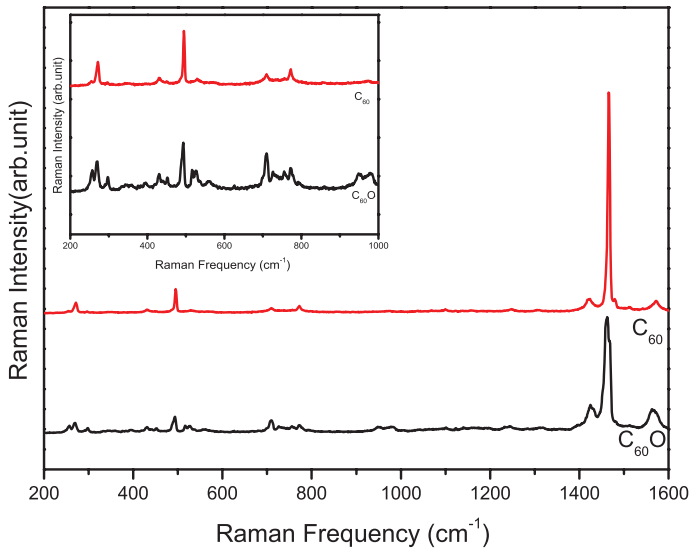

Figure 5.2: Room temperature Raman spectra of photo-polymerized $C_{60}O$ measured using 514 nm laser excitation.

C_{60} in the presence of an oxygen [54, 52]. Raman spectrum of $C_{60}O$ are taken in the frequency region 200-1600 cm^{-1}. In the lower-frequency region, the vibrational peak observed at 493.6(1) cm^{-1} in $C_{60}O$ is downshifted by 4 cm^{-1} from that of the A_g breathing mode of pristine C_{60}. The appearance of other peaks at 256.3(3) cm^{-1} and 270.5(1) cm^{-1} in $C_{60}O$ can be explained as the splits in H_g squashing mode of C_{60} where 256.3 cm^{-1} peak arises due to the translation of the bound oxygen atom. In the higher-frequency region, the peak at 1458.8(2) cm^{-1} is accompanied with a shoulder at 1468.4(2) cm^{-1} and are attributed to photo-polymerization of C_{60} [43, 185]. In this work, the thermal analysis is performed on 256.3 cm^{-1}, 270.5 cm^{-1}, 1458.8 and 1468.4 cm^{-1} peaks of $C_{60}O$.

The observed Room temperature UV-vis and Raman spectra analysis confirmed the formation of photo-polymerized $C_{60}O$ and it was used for the further experiments.

5.2.3 Thermal effects on Raman spectra

Temperature dependent Raman measurements are performed on the photo-polymerized $C_{60}O$ by lowering temperature from 300 K to 80 K to examine intra-cage and inter-cage interactions. Raman spectra of $C_{60}O$ in the temperature range 80-300 K at excitation wavelength 488 nm are shown in Figure 5.3. Raman spectrum of $C_{60}O$ are taken in two regions–i) 200-700 cm^{-1} and ii)1000-1600 cm^{-1}. Due to their strong intensities and characteristic contribution,thermal effect on 256.3 cm^{-1}, 270.5 cm^{-1}, 488.8 cm^{-1}, 1458.8 cm^{-1} and 1468.4 cm^{-1} peaks of $C_{60}O$ are examined further.

Upon decreasing the temperature to 80 K, all vibrational peaks get blue-shifted. At 80 K, the 256.3 cm^{-1}, 270.5 cm^{-1} and 488.8 cm^{-1} peaks are observed at 257.3(3), 271.6(1) cm^{-1} and 489.3 cm^{-1}, whereas, 1458.8 cm^{-1} and

1468.4 cm^{-1} peaks are seen at 1462.3(1) cm^{-1} and 1471.8(4) cm^{-1} respectively. The thermal variation of 256.3 cm^{-1}, 270.5 cm^{-1},1458.8 cm^{-1} and 1468.4 cm^{-1} peaks are illustrated in Figure 5.4. The thermal variation of the observed

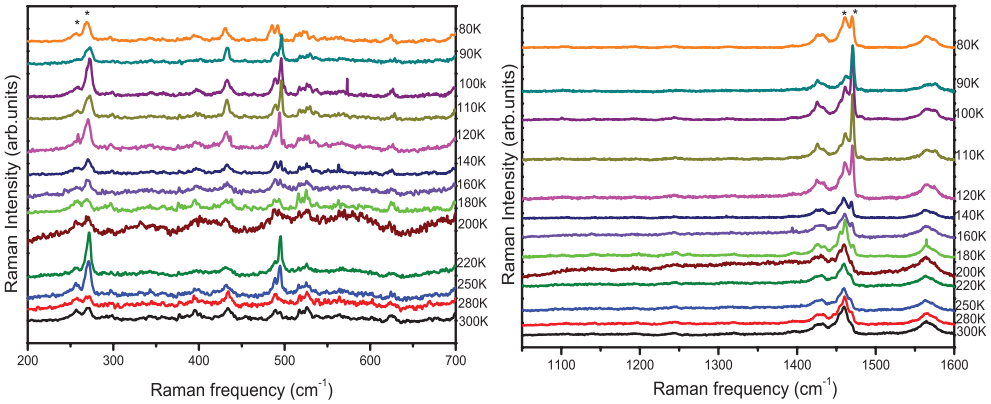

Figure 5.3: Temperature dependent Raman spectra of photo-polymerized $C_{60}O$ obtained between 80 and 300 K with excitation wavelength 488 nm.

Raman peaks are fitted by Eq.4.5 as mentioned in Chapter 4. The fitting parameters ν_0 and χ_T are evaluated and tabulated in Table 5.1. It can be obtained from the table that temperature coefficients (χ_T) of all observed phonon peaks in $C_{60}O$ are negative and is attributed to thermal contraction of the cage which influences their bond-lengths and the inter and intra-molecular interactions. χ_T of $C_{60}O$ are found to be analogous to that of pristine C_{60} which suggests that both molecules experience similar contraction with lowering of temperature [186]. In higher frequency region, χ_T of 1468 cm^{-1} peak of $C_{60}O$ are found to be comparable to the G-peak(1582 cm^{-1}) of single layered graphene [187]. The temperature coefficient for the highly oriented pyrolytic graphite (HOPG) was previously reported as -0.011 cm^{-1} /K for 1578 cm^{-1} which is comparable with our obtained χ_T of 1458.2 cm^{-1} peak which is attributed to the photo-polymerized $C_{60}O$[188].

Force constant (k) of C_{60}–O was evaluated using Eq.4.4 as mentioned in Chapter 4 and plotted in Figure 5.5 as a function of temperature. The reduced mass of $C_{60}O$ is 15.6 a.m.u. At room temperature k for C_{60}–O is found to be

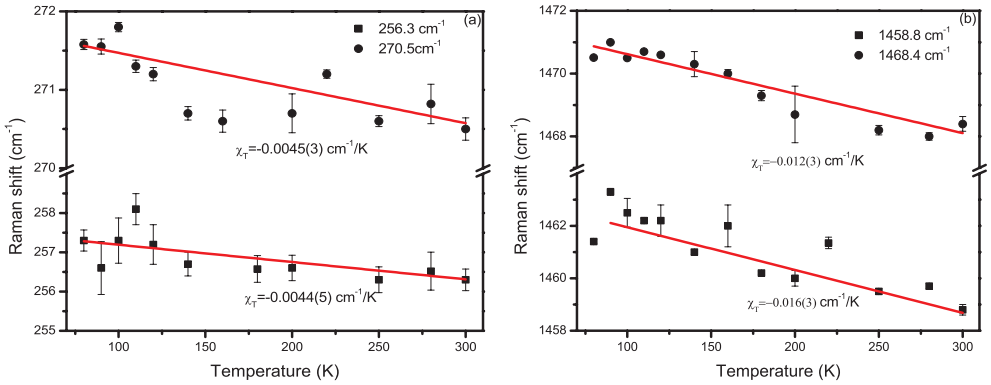

Figure 5.4: Temperature dependent Raman shifts observed at (a) 256.3 cm^{-1} and 270.5 cm^{-1} (b) 1458.8 and 1468.4 cm^{-1} peaks due to small local perturbation of oxygen in C_{60}

Table 5.1: Temperature dependent frequency coefficients(χ_T) of different peaks of photo-polymerized $C_{60}O$

Raman position(cm^{-1})	χ_T (cm^{-1}/K)	ν_0 (cm^{-1})
256.3	-(0.0044±0.0015)	257.6(3)
270.5	-(0.0045±0.0013)	271.9(2)
488.8	-(0.003±0.001)	489.3(1)
1458.8	-(0.016±0.003)	1463.6(5)
1468.4	-(0.012±0.003)	1471.9(3)

0.604 N cm^{-1}. Upon lowering temperature to 80 K the k value increases to 0.610 N cm^{-1}. Increase in force constant of C_{60}–O bond at low temperature signifies thermal contraction in the bond length. Cage contraction and distortion in the local environment of the oxygen ion gives rise to blue-shifts in all the resulting phonon frequencies. Inter-molecular interaction is also supported by low temperature magnetic hysteresis of $C_{60}O$ as mentioned in **Appendix** suggest weak long range ferromagnetic interactions between the molecules.

The thermal interaction affects phonon lifetime which causes change in the phonon line-width in the Raman spectra. Temperature dependent FWHM of 256.3 cm^{-1}, 270.5 cm^{-1}, 488.8 cm^{-1}, 1458.8 cm^{-1} and 1468.4 cm^{-1} vibrational peaks in $C_{60}O$ are shown in Figure 5.6(a). At room temperature, the line-width was found to be 12.2(9) cm^{-1}, 7.7(5) cm^{-1} and 5.9(7) cm^{-1} for 256.3 cm^{-1}, 270.5 cm^{-1} and 488.8 cm^{-1} peak, respectively. It is evident from the plot

that their line-widths are nearly temperature independent which is attributed to the presence of negligible anharmonic contributions in the lower phonon frequencies. FWHM of 1468.4 cm^{-1} peak decreases with decrease in temperature whereas,line broadening in 1458.8 cm^{-1} peak is observed upon lowering the temperature. The temperature dependent line-widths of higher frequency peaks of $C_{60}O$ shows presence of anharmonic contribution of phonons.

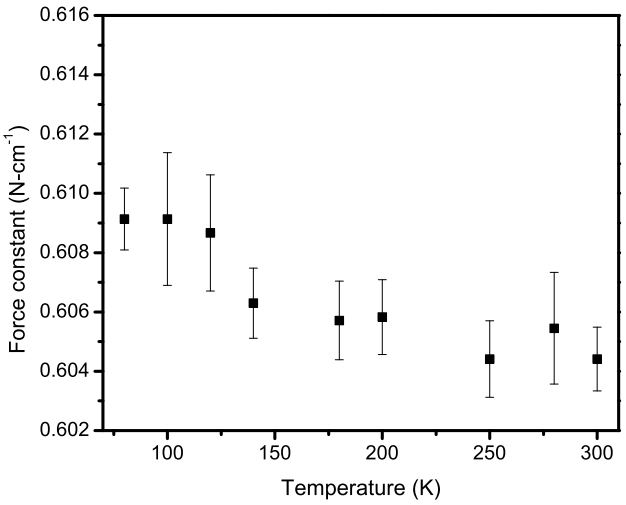

Figure 5.5: The force constants variation with temperature for C_{60}–O interaction.

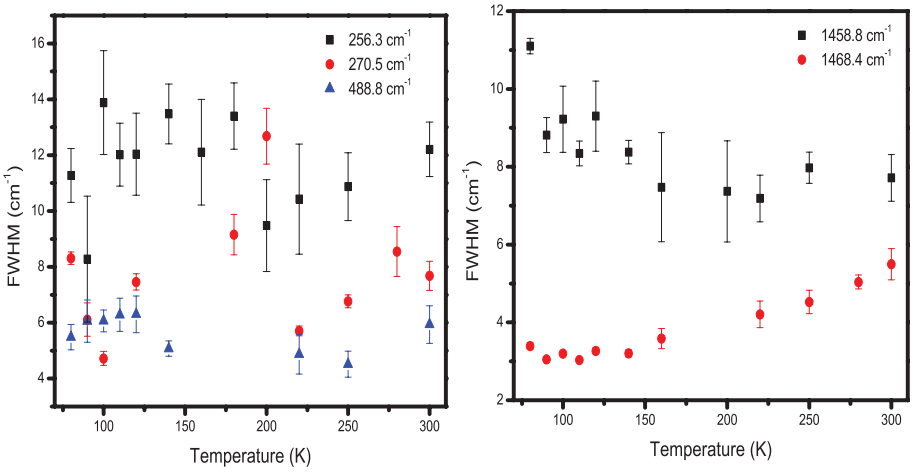

Figure 5.6: (a) Temperature dependent FWHM of (a)256.3, 270.5 and 488.8 cm^{-1} peak and (b) 1458.8 and 1468.4 cm^{-1} peak of $C_{60}O$.

In order to understand the dynamics of C–O bond in $C_{60}O$ under thermal stress, density functional theory (DFT) was carried out on the optimized structure of $C_{60}O$ by changing C–O bond length. $C_{60}O$ was optimized as both epoxide and annulene-like structure by using the density functional B3LYP method. 6-31G(d) basis set was used in annulene and 6-31+G(d) basis set was used in epoxide structure to calculate theoretical Raman vibrational spectra of $C_{60}O$ single molecule. In the procedure of optimization, an option SCF =Tight was used. Molecular modeling and vibrational spectral analysis were performed using Gaussian 9, GaussView 5.0 and OriginPro 8.1 software. Calculated Raman spectrum was compared with our experimental result in the frequency range 200-600 cm^{-1} as shown in Figure 5.7. The calculated Raman peaks for optimized annulene-like structure were obtained at 235.7, 242.6 and 272.9 cm^{-1} whereas for optimized epoxide structure, Raman peaks were obtained at 241.6 and 266.4 cm^{-1}. Experimentally the corresponding Raman peaks are observed at 249.3, 256.3 and 270.5 cm^{-1}. The experimental spectrum was obtained for $C_{60}O$ films, whereas the DFT calculation was performed on a single molecule and, due to this discrepancy, a small variation in the two results was perceived. It is observed from the Figure 5.7 that the calculated vibrational peaks of annulene-like structure resembles more to the experimental results. Based on the observation, further calculations were performed on the optimized $C_{60}O$ annulene-like structure.

In the optimized structure of $C_{60}O$, C–O bond length was obtained 1.398 $\mathring{A}$ that is consistent with the previous reports[48, 189]. To observe shifts in the Raman frequency, C–O bond length was deliberately changed by 0.7%. The obtained shift in 235.7 cm^{-1} peak as a function of C–O bond length is shown in Figure 5.8 and was fitted with an exponential decay function. No shift in the 273 cm^{-1} peak was found as C–C bond lengths was constrained to remain unchanged during the calculation. Both calculated and experimental

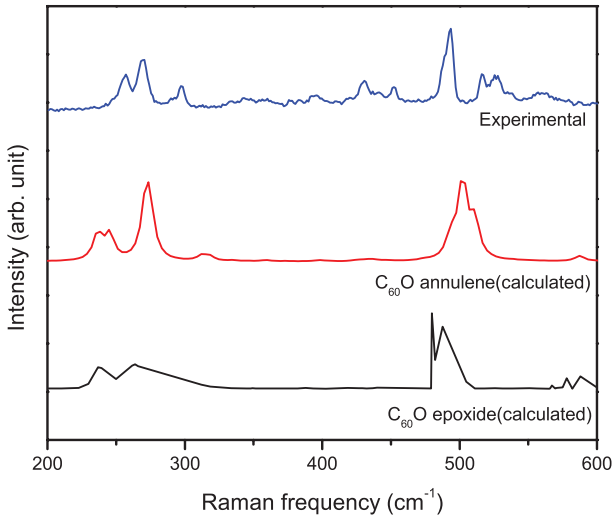

Figure 5.7: Experimental and calculated Raman spectra of $C_{60}O$ in the region 200-600 cm^{-1}.

results indicate thermal contraction in C–O bond that blue-shifts the Raman peak at 235.7 cm^{-1} with decrease in temperature. Experimentally, the shift in 256.5 cm^{-1} peak was about 1 cm^{-1} at 80 K as compared to that at room temperature which was attributed to thermal contraction in C–O bond by 0.009(2) $\AA$. Expansion or contraction of molecule is elucidated by its thermal expansion coefficient. Linear thermal expansion coefficient α_T which can be determined as:

$$\alpha_T = \frac{1}{l}\frac{dl}{dT} \tag{5.1}$$

where dl/l is the relative change in C–O bond length as a result of the thermal expansion due to temperature change dT. The linear thermal expansion coefficients of bulk and thin films of C_{60} were reported previously [190, 191]. Using Eq.5.1, α_T of $C_{60}O$ was found to be 30×10^{-6} K^{-1} at 80 K. The thermal expansion coefficient give further information about the temperature dependent thermoelastic behavior of materials which can be described by isobaric mode

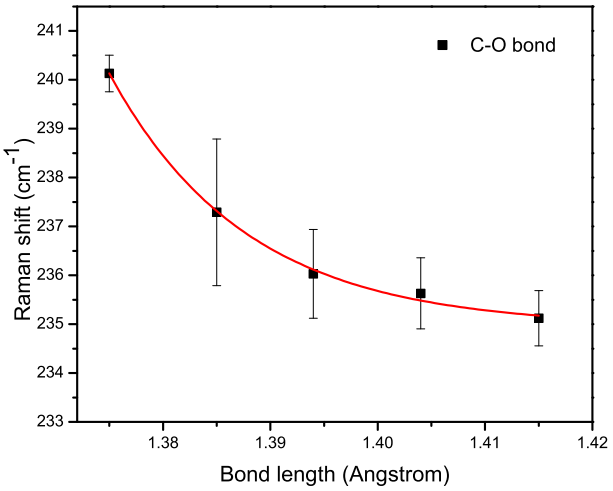

Figure 5.8: Raman shift in the 235.7 cm^{-1} peak as a function of C–O bond length.

Grüneisen parameter(γ_{iP}):

$$\begin{aligned} \gamma_{iP} &= \frac{1}{\alpha_T \nu_i} \left(\frac{\partial \nu_i}{\partial T} \right)_P \\ &= \frac{1}{\alpha_T \nu_i} \chi_T \end{aligned} \tag{5.2}$$

From Eq. 5.2, γ_{iP} was calculated by using the fitted χ_T of 256.3 cm^{-1} peak reported in Table 5.1. The estimated γ_{iP} for all the observed phonon peaks of $C_{60}O$ were presented in Table 5.2. At 80 K, Grüneisen parameter for all the observed phonon peaks are found to be positive.

Thermal expansion coefficient of $C_{60}O$ are found larger than that of pristine C_{60} [192]. Due to the presence of oxygen, the symmetry of the cage is reduced which results inter-atomic bonds weak in $C_{60}O$ and lead to increase in their expansivity as compared to the unoxidised C_{60}. The expansion or contraction of solid due to temperature depends on the balance between phonon modes with positive and negative Grüneisen parameter [193]. The positive low-temperature Grneisen gamma is reported for C_{60} down to 30 K [194]. Like C_{60}, Positive Grüneisen parameter suggests the volume expansion is positive at 80 K in

Table 5.2: Phonon frequencies, temperature coefficients, and the Grüneisen parameters for $C_{60}O$.

Raman position(cm^{-1})	χ_T (cm^{-1}/K)	γ_{iP}
256.3	-(0.0044±0.0015)	0.572
270.5	-(0.0045±0.0013)	0.554
1458.8	-(0.016±0.003)	0.365
1468.4	-(0.012±0.003)	0.272

$C_{60}O$.

5.3 Optical property of $C_{70}O$

5.3.1 UV-vis spectral analysis

UV-vis absorption spectra of pristine C_{70} and synthesized $C_{70}O$ in CS_2 at room temperature are shown in Figure 5.9. In pristine C_{70}, absorption bands are observed at 382.7 nm, 472.6 nm, 550 nm and 640 nm. The UV-vis spectra of C_{70} and $C_{70}O$ are similar to each other. The spectrum of $C_{70}O$ shows all absorption bands of pristine C_{70}, with slightly shifted and broadened. In $C_{70}O$, absorption bands are observed at 381.9 nm, 480 nm, 564 nm, 605.5 nm and 650.3 nm which correspond to reported absorption of $C_{70}O$ oxidoannulene [195, 51] . The $C_{70}O$ oxidoannulene is closely associated to C_{70}, as the oxygen atom seems to introduce only a minor perturbation in electronic and lattice structure [48].

5.3.2 Raman spectral analysis

Raman spectrum of $C_{70}O$ at room temperature is shown in Figure 5.10. In C_{70}, the Raman peaks are observed at 259 cm^{-1},1182 cm^{-1},1227 cm^{-1} and 1563 cm^{-1} and are in argument with the earlier reports [196]. The vibrational peaks of $C_{70}O$ are seen in the same characteristic regions as that of Pristine C_{70}. However, low frequency Raman peak 259 cm^{-1} are found to be partially split for $C_{70}O$ and is observed at 251.7 cm^{-1} and 258.3 cm^{-1}. The observed

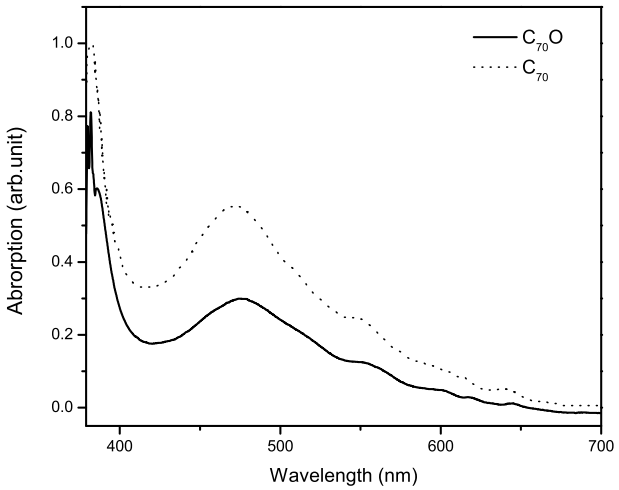

Figure 5.9: Room temperature UV-vis spectra of C_{70} and $C_{70}O$ dissolved in CS_2

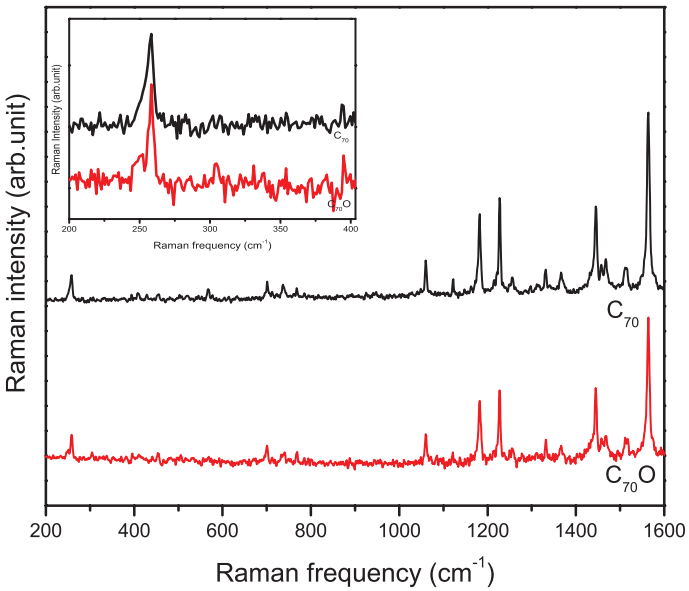

Figure 5.10: Room temperature Raman spectra of $C_{70}O$ measured using 514 nm laser excitation.

split in vibrational peak is due to the reduced symmetry of C_{70} in the presence of oxygen. However, no shift is observed in higher vibrational peaks which suggests no photo-polymerization has occurred in $C_{70}O$.

The observed Room temperature UV-vis and Raman spectra analysis confirm the formation of unpolymerized $C_{70}O$ which is used for the further experiments.

5.3.3 Thermal effects on Raman spectra

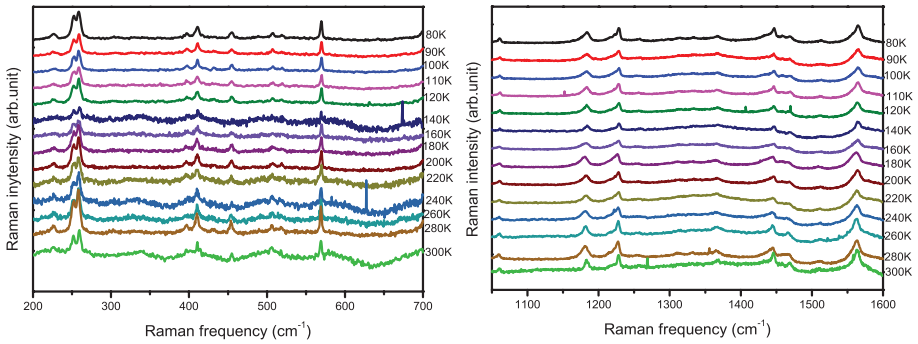

Figure 5.11: Temperature dependent Raman spectra of photo-polymerized $C_{70}O$ obtained between 80 and 300 K with excitation wavelength 488 nm.

Thermal effects on Raman spectra of $C_{70}O$ are observed using excitation wavelength 488 nm. Raman spectra are obtained in the temperature range 80-300 K and are shown in Figure 5.11. In this work, the thermal analysis is performed on 251.7 cm^{-1} and 258.3 cm^{-1} peaks of $C_{70}O$. Upon decreasing the temperature to 80 K, all Raman peaks of $C_{70}O$ are weakly blue-shifted. The thermal variation of the peak positions 251.7 cm^{-1} and 258.3 cm^{-1} are illustrated in Figure 5.12. The variation in 251.7 cm^{-1} and 258.3 cm^{-1} peaks are fitted with Eq.4.5(chapter 4) and the fitting parameters ν_0 and χ_T are tabulated in Table 5.3. Thermal variations in Raman frequencies give negative temperature coefficients for all observed Raman peaks in both $C_{60}O$ and $C_{70}O$. In low frequency region, χ_T of $C_{60}O$ and $C_{70}O$ are found to be smaller than that of $Gd@C_{82}$ and $Dy@C_{82}$ as reported in Chapter 4. This could be attributed to

the reduced symmetry of C_{82} as compared to that of C_{60} and C_{70} cage [26].

Table 5.3: Temperature dependent frequency coefficients(χ_T) of different peaks of $C_{70}O$

Raman position(cm^{-1})	χ_T (cm^{-1}/K)	ν_0 (cm^{-1})
251.7	-(0.0016±0.0003)	252.2(4)
258.3	-(0.0027±0.0003)	259.1(4)

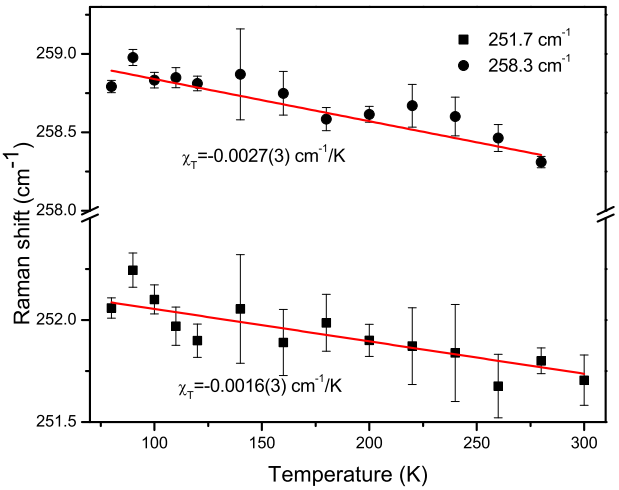

Figure 5.12: Temperature dependent Raman shifts observed at 251.7 cm^{-1} and 258.3 cm^{-1} of $C_{70}O$.

k value of C_{70}–O is estimated using Eq. 4.4 and plotted in Figure 5.13 as a function of temperature. The reduced mass of C_{70}–O is 15.7 a.m.u. We obtain k of C_{70}–O as 0.586 N-cm^{-1} at room temperature whereas at 80 K, k value increases to 0.590 N-cm^{-1}.

Increase in force constant with lowering temperature indicates thermal contraction in the bond length. Hence, the blue-shifts in all resulting phonon frequencies of $C_{60}O$ and $C_{70}O$ are attributed to the contraction of cage and distortion in oxygen bond which is exhohedrally attached to the cage. Temperature dependent FWHM of 251.7 and 258.3 cm^{-1} peaks in $C_{70}O$ are shown in Figure 5.14. At room temperature, the linewidths are found to be 4.5(3) cm^{-1} and 4.8(3) cm^{-1} for 251.7 and 258.3 cm^{-1} peaks, respectively. At 80 K, their FWHM

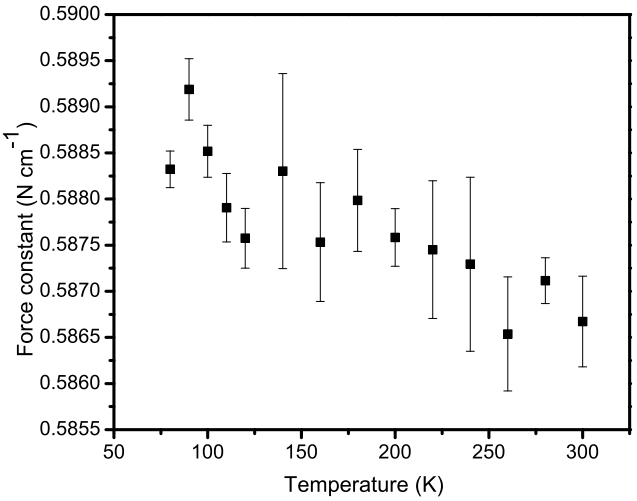

Figure 5.13: The force constants variation with temperature for C_{70}–O interaction.

are observed to be 5.8(3) and 5.7(1) cm^{-1} for the corresponding peaks. From Figure 5.14, it is evident that their line-widths are weakly temperature dependent suggesting negligible anharmonic phonon contribution in line broadening.

5.4 Effect of laser power on Raman spectra

5.4.1 Effect of laser power on Raman spectra of $C_{60}O$

The laser-power-dependent Raman spectra of $C_{60}O$ are performed at room temperature using 514.5 nm excitation by varying the laser power between 0.1 mW and 0.5 mW. At 0.1 mW, $C_{60}O$ vibrational peaks are found at 256.2(4) cm^{-1}, 270.7(2) cm^{-1} and 488.8(8) cm^{-1}. Upon increasing the laser power to 0.5 mW, Raman peaks at 256.2 cm^{-1}, 270.7 cm^{-1} and 488.8 cm^{-1} shifted to 255.2 cm^{-1}, 270 cm^{-1} and 487 cm^{-1} respectively. With increase in the laser power, local temperature of fullerene thin films also increases resulting in the red-shift Raman peaks.

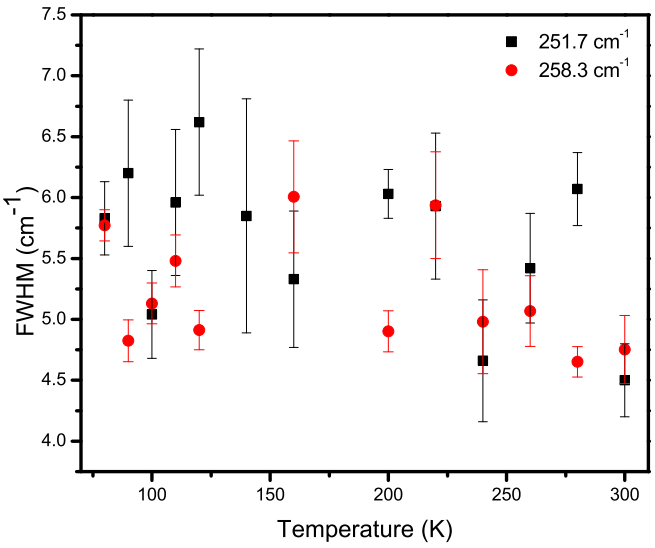

Figure 5.14: Temperature dependent FWHM of 251.7 and 258.3 cm^{-1} peak of $C_{70}O$.

Raman shift with the laser power was fitted with the Eq.4.10 and the respective χ_L is evaluated. The shift in the observed Raman frequencies as a function of laser power is shown in Figure 5.15. The evaluated fitting parameter χ_L for corresponding phonon frequencies are tabulated in Table 5.4. The change in the phonon vibrational frequencies with the laser power is associated to the heating effect of the laser which causes the red-shift in the peaks. Thus, laser power induced red-shift is attributed to the thermal expansion of the lattice.

5.4.2 Effect of laser power on Raman spectra of $C_{70}O$

Laser-power-dependent Raman spectra of $C_{70}O$ is performed at room temperature using 514.5 nm excitation and by varying the laser power between 0.1 mW and 0.5 mW. At 0.1 mW, $C_{70}O$ vibrational peaks are found at 251.5(6) cm^{-1} and 259.5(1) cm^{-1} and their variation with laser power is plotted in Figure 5.16. Upon increasing the laser power to 0.5 mW, Raman peaks at 251.5 cm^{-1} and 259.5 cm^{-1} shift to 251.1 cm^{-1} and 258.9 cm^{-1} respectively.

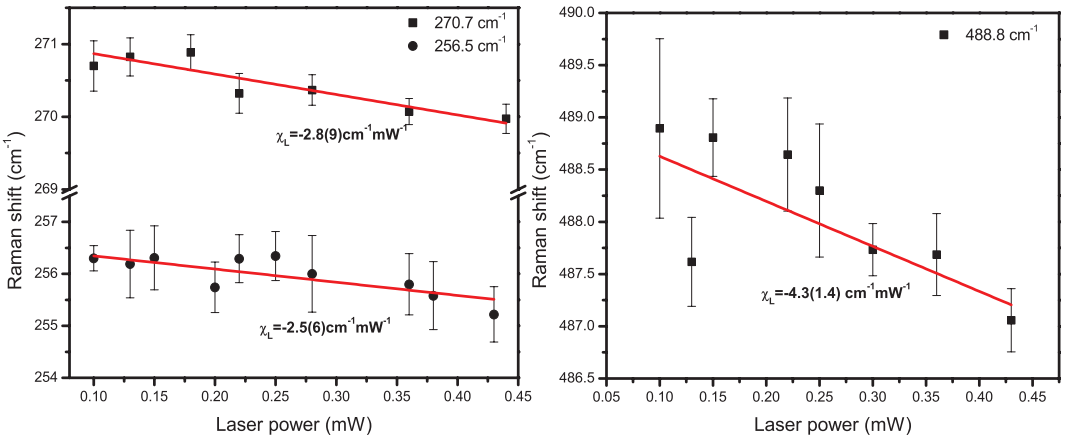

Figure 5.15: Laser power dependent Raman peak shift at 256.5 cm^{-1}, 270.7 cm^{-1} and 488.8 cm^{-1} of $C_{60}O$.

The shift in the observed Raman frequencies as a function of laser power with its linear fit is shown in Figure 5.16. It is evident from the figure that the increase in the laser power locally heats the fullerenes and leads to red-shift in the observed frequencies. The fitting parameter χ_L for corresponding phonon frequencies are tabulated in table 5.4.

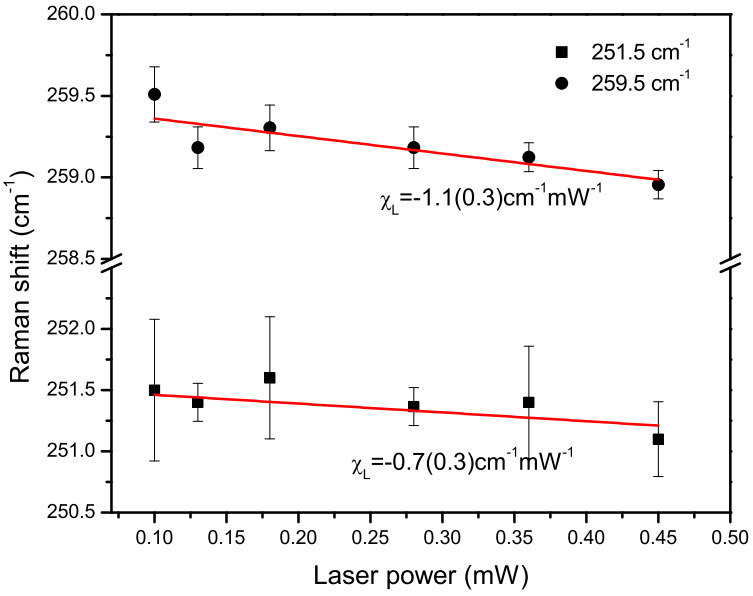

Figure 5.16: Laser power dependent Raman peak shift at 251.5 cm^{-1} and 259.5 cm^{-1} of $C_{70}O$.

Table 5.4: Power dependent frequency coefficients(χ_L) of different peaks of $C_{60}O$ and $C_{70}O$

Sample	Raman position(cm^{-1})	χ_L ($cm^{-1}mW^{-1}$)
$C_{60}O$	256.5	-2.8(9)
	270.7	-2.5(6)
	488.8	-4.3(1.4)
$C_{70}O$	251.5	-1.1(3)
	259.5	-0.7(3)

χ_L of $C_{60}O$ are found to be larger than that of $C_{70}O$. In addition, χ_L of $C_{60}O$ and $C_{70}O$ are also compared with the cage internal vibrations of $Gd@C_{82}$ and $Dy@C_{82}$. χ_L values are found to be decreasing with increase in no of atoms in the cages. As the number of atom increases from C60 to C82, the cage symmetry reduces which in turn enhances the heat dissipation in these fullerenes [26].

As laser beam causes local heating effect on the surface of the film, the local temperature of the sample under the laser spot can be estimated from the laser power used in Raman measurement. The collective effect of temperature and laser power on Raman frequencies are used for the thermal conductivity estimation.

5.5 Thermal conductivity

In this section, the thermal conductivity of photo-polymerized $C_{60}O$ and $C_{70}O$ films are estimated using Eq. 4.11 as mentioned in Chapter 4. Gaussian beam profile of 514.5 nm laser was shown in Chapter 3 where d_0 was obtained as 3.6 μm. In order to examine the spectral contributions to the thermal conductivity, all observed phonon frequencies of photo-polymerized $C_{60}O$ and $C_{70}O$ are considered. In $C_{60}O$, κ near room temperature and ΔT were calculated for 256.5 cm^{-1}, 270.7 cm^{-1} and 488.8 cm^{-1}. The estimated κ using Eq. 4.11 are tabulated in table 5.5. Similarly, κ near room temperature was determined

for 251.5 cm^{-1} and 259.5 cm^{-1} peak in $C_{70}O$ and the corresponding values are reported in table 5.5.

Table 5.5: Thermal conductivity(κ)at their corresponding temperatures (T) of different peaks of $C_{60}O$ and $C_{70}O$

Sample	Raman position (cm^{-1})	T_R (K) (K)	κ ($Wm^{-1}K^{-1}$)
$C_{60}O$	256.5	324	0.7(2)
	270.7	302	1.1(3)
	488.8	319	0.8(3)
$C_{70}O$	251.5	351	0.3(1)
	259.5	359	0.4(1)

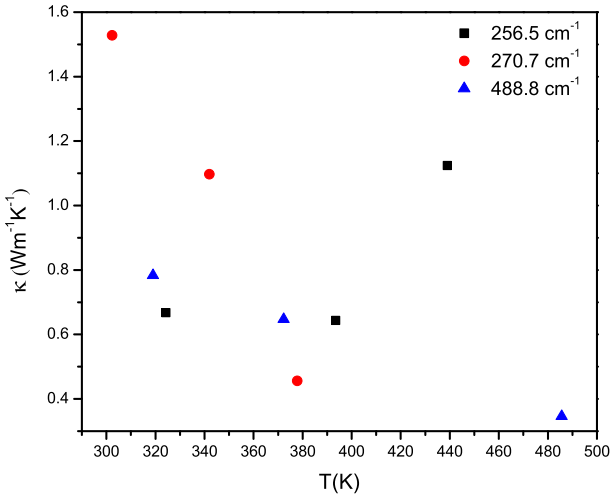

Figure 5.17: Thermal conductivity at different temperatures for 256.5 cm^{-1}, 270.7 cm^{-1} and 488.8 cm^{-1} peaks in $C_{60}O$.

We have also evaluated the thermal conductivity from C-O and C-C vibration for both the samples as shown in Figure 5.17 and 5.18. Thermal conductivity is found to be weakly dependent on phonon frequencies.

In pristine fullerenes, κ has mostly phonon contributions where the heat conduction occurs via lattice vibrations of covalently bonded carbon atoms. Tea *et al.* reported room temperature thermal conductivity of C_{60} and C_{70} was 0.4 $Wm^{-1}K^{-1}$ and 0.7 $Wm^{-1}K^{-1}$ respectively [180]. However, presence of

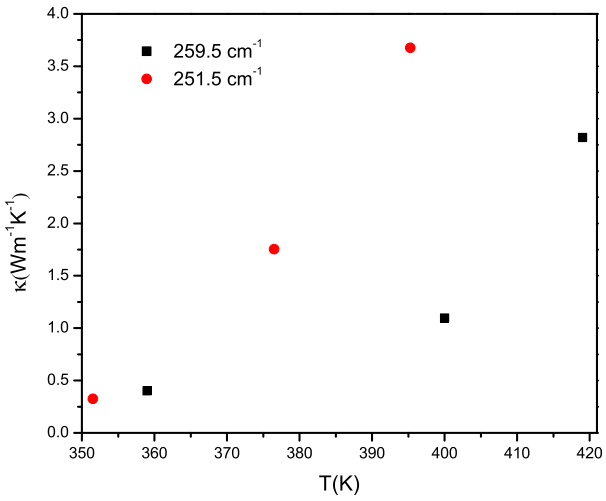

Figure 5.18: Thermal conductivity at different temperatures for 251.5 cm^{-1} and 259.5 cm^{-1} peaks in $C_{70}O$.

oxygen in fullerene cage contribute additional interaction between oxygen and cage which weakly modifies their thermal conductivity.

Thermal conductivities of $C_{60}O$ and $C_{70}O$ are found to be smaller than that of $M@C_{82}$ (Chapter 4). This could be attributed to Raman peaks considered for the evaluation of thermal conductivities of the endohedral fullerenes which are smaller (<200 cm^{-1}) than that of exohedral fullerene $C_{60}O$ (>200 cm^{-1}). κ value of $C_{60}O$ and $C_{70}O$ are comparable with amorphous carbon film (0.2 $Wm^{-1}K^{-1}$) and graphitic carbon nanosphere (GCNS) (0.9 $Wm^{-1}K^{-1}$) [197, 111].

Having high Seebeck coefficients and low thermal conductivities, the figure of merits (ZT) of fullerene molecules are large in comparison to graphene [10, 198]. In the previous reports, the Seebeck coefficient and electrical conductance of C_{60}, C_{82} and $M@C_{82}$ molecules have been discussed and are utilized for the comparison of their ZT [199, 21]. Their study suggest that power factor of $M@C_{82}$ is larger than the empty fullerene molecules. However, due to high thermal conductivity of $M@C_{82}$, their ZT value reduces. As thermal conductivity

of $C_{60}O$ and $C_{70}O$ are marginally greater than their empty fullerenes, fullerene oxides appear as potential candidates for the thermoelectric applications.

5.6 Conclusion

In this chapter, the thermal effect on photo-polymerized $C_{60}O$ and $C_{70}O$ films are examined. Room temperature UV-Vis and Raman spectra confirmed the formation of photo-polymerized $C_{60}O$ and $C_{70}O$(unpolymerized). The blue-shift with decrease in temperature in observed phonon frequencies for both materials can be explained in terms of thermal contraction in fullerene cages. Thermal expansion coefficient of $C_{60}O$ is evaluated at 80 K considering the change in C–O bond-length by incorporating DFT calculation with temperature dependent Raman shift. Positive Grüneisen parameter and thermal expansion coefficient at 80 K indicates positive volume expansion at 80 K. The low frequency phonon linewidths of $C_{60}O$ and $C_{70}O$ are found to be nearly independent of temperature indicating negligible anharmonic contributions. However, the temperature behavior of higher frequency phonon line-widths of $C_{60}O$ show anharmonic contributions.

Thermal conductivity of photo-polymerized $C_{60}O$ and $C_{70}O$ films are obtained using temperature and laser power dependent Raman spectra. Thermal conductivity is observed to be weakly dependent on phonon frequencies. κ of $C_{60}O$ and $C_{70}O$ films are found to be 0.7(2) $Wm^{-1}K^{-1}$ and 0.3(1) $Wm^{-1}K^{-1}$ which are marginally larger than their unoxidised cages. Their increased thermal conductivity could be originated from the additional interaction between oxygen and cage. However, TC of fullerene oxides are found to be much smaller than $M@C_{82}$ suggesting fullerene oxides as suitable dopant in thermoelectric devices.

Chapter 6

Effect of pressure on photo-polymerized $C_{60}O$

6.1 Introduction

Like temperature, pressure is one of the fundamental thermodynamic variables governing the lattice dynamics of materials. Under ambient conditions, solids exhibit a particular crystal structure for which the total energy is minimum. On application of high pressure, the atomic arrangement in the solid changes. As a result, the interatomic distance changes and consequently the crystal structure are expected to modify. The reduction in the intermolecular distance can be used to tune intermolecular forces in the materials. Thus, the high-pressure studies have great importance in visualizing the mechanism governing the structure formation and their properties. Under thermal and mechanical stress, the orientation of C_{60} cages and their interactions with the neighborhood vary due to the change in their lattice parameters [183, 200].

Effect of temperature on the vibrational frequencies of Gd@C_{82}, Dy@C_{82}, photo-polymerized $C_{60}O$ and $C_{70}O$ have been studied in Chapter 4 and 5. To examine the effect of extreme condition, high pressure behavior should be also

taken into account. In this chapter, we have discussed the effect of pressure on photo-polymerized $C_{60}O$ film by performing Raman measurements. When pressure changes, the structural and optical properties of photo-polymerized $C_{60}O$ are expected to modify which could be reflected in their vibrational spectra. The pressure dependent Raman spectroscopy of $C_{70}O$ is attempted in this section.

6.2 Pressure effects on Raman spectra of photo-polymerized $C_{60}O$

Pressure dependent Raman spectra of photo-polymerized $C_{60}O$ was performed using 514.5 nm laser excitation. Due to the strong intensity of 1332 cm^{-1} peak of diamond in the pressure cell, the frequency range from 1250 cm^{-1} to 1400 cm^{-1} was overshadowed. Due to this, the spectra are taken in two separate regions (i) 200-600 cm^{-1} and (ii)1400-1600 cm^{-1}. The observed spectra are illustrated in the Figure6.1. At ambient pressure, 256.3(4) cm^{-1} and 270.7(2) cm^{-1} peaks peak observed in the lower frequency region and at 1458.5(6) cm^{-1} and 1468.3(1) cm^{-1} are observed in higher frequency region.

To observe the change in the lattice vibration properties of photo-polymerized $C_{60}O$ under compression, Raman spectra is studied by varying pressure upto 5.5 GPa as shown in Figure 6.1. Both 270.7 cm^{-1} and 256.3 cm^{-1} peaks are red-shifted upon increasing the pressure upto 0.8 GPa. Above 1 GPa, both peaks disappear. The Raman peak at 1458.5 cm^{-1} shifts to higher frequencies whereas 1468.3 cm^{-1} peak is red-shifted upon increasing the pressure to 1.2 GPa. Above 1.2 GPa, two peaks appear as a single peak at 1463.8(2) cm^{-1} which shifts linearly to higher frequencies with the pressure up to 5.5 GPa. Upon releasing pressure, the reappearance of 1458.5 cm^{-1} and 1468.3 cm^{-1} peaks are observed whereas no noticable peaks are found in the lower frequency region (Figure 6.2).

The observed shift in these Raman peaks with the applied pressure is shown in Figure 6.3. Pressure induced Raman shift is defined as:

$$\nu_P = \nu_0 + \chi_P P \tag{6.1}$$

where ν_0 is the frequency at ambient condition and χ_P is the 1st order pressure coefficient. P is the applied pressure on the sample. χ_P for each peak is

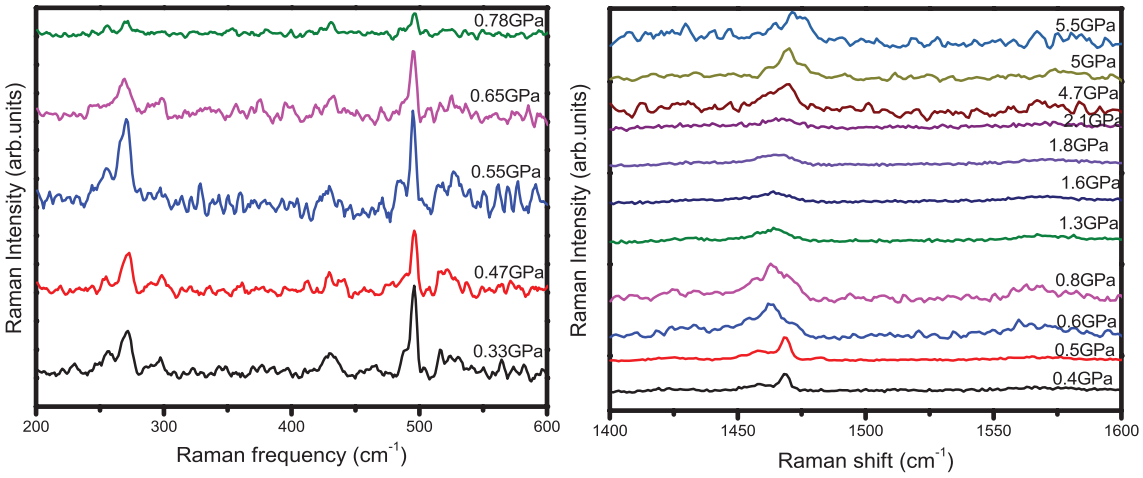

Figure 6.1: Pressure dependent Raman spectra of $C_{60}O$ measured between 0.3-5.5 GPa using 514nm laser excitation in the frequency range (a)200-600 cm^{-1} and (b)1400-1600 cm^{-1}

evaluated by linear fitting and is presented in Table 6.1. At 0.8 GPa, Raman peak at 256.2 cm^{-1} and 270.7 cm^{-1} are red-shifted by 8 cm^{-1} and 1.1 cm^{-1} respectively, as compared to that at atmospheric pressure. From the shift in both the Raman peaks it could be expected that C–O bond experiences more compression than C-C bond. Below 1.2 GPa, the reported linear compressibility of C_{60} is about 0.023 GPa^{-1} which is very similar to the interplanar interaction in graphite($\sim 0.026\ GPa^{-1}$)[201, 28]. The linear compressibility of a material at constant temperature is described as [202]:

$$K_a = -\frac{1}{l}\left(\frac{dl}{dp}\right)_T \tag{6.2}$$

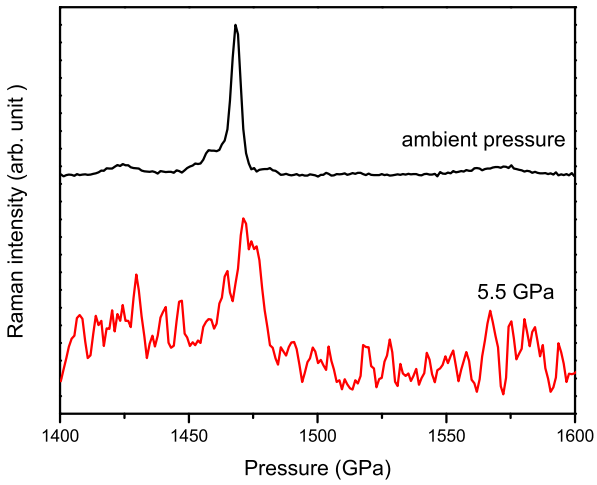

Figure 6.2: Pressure dependent Raman spectra of $C_{60}O$ measured upon releasing pressure to an ambient condition

where dl/l is the relative change in C–O bond length due to pressure change dP. From the calculated C–O bond length as a function of Raman shift, we have estimated the change in C–O bond at 1.2 GPa. 8 cm^{-1} shift in 256.2 cm^{-1} peak at 1.2 GPa is attributed to contraction in C–O bond by 0.313(2) $\AA$. Using Eq. 6.2, K_a of $C_{60}O$ is found to be 0.186 GPa^{-1} at 1.2 GPa. Due to the presence of oxygen, the symmetry of the cage is reduced which results in weak inter-atomic bonds in $C_{60}O$ and lead to increase in their compressibility as compared to C_{60}.

As the pressure below 1.2 GPa has negligible effects on C-C bonds, we consider that the observed red-shifts in C-C and C-O vibrations are due to decrease in inter-molecular spacing and compression in $C_{60}O$ cluster. The compression in the molecular cluster results in reduced lattice parameter and constraints in the rotational motion of the molecules. Fischer *et al.* reported FCC-to-SC transition of C_{60} structure above 1.2 GPa [28]. Hence, change in χ_P of 1468.3 cm^{-1} at 1.2 GPa is attributed to C_{60} orientational phase transition [200]. Above 1.2 GPa interaction between the neighboring molecules increases which leads to the formation of inter-molecular bonds and thus their polymerization [203]. From the obtained results it can be stated that above 1.2 GPa pressure, further

polymerization occurs in photo-polymerized $C_{60}O$. The pressure below 1.2 GPa is denoted as phase I and above 1.2 GPa it is denoted as phase II.

Table 6.1: Pressure coefficients(χ_P) of different peaks of $C_{60}O$.

Raman peaks (cm^{-1} at 1 atm)	χ_P (Phase I) (cm^{-1} GPa^{-1})	χ_P (Phase II) (cm^{-1} GPa^{-1})
1468.3	-3.9(2.1)	1.6(0.2)
1458.5	3.8(1.7)	–
270.7	-5.1(2.5)	–
256.2	-14.1(6.6)	–

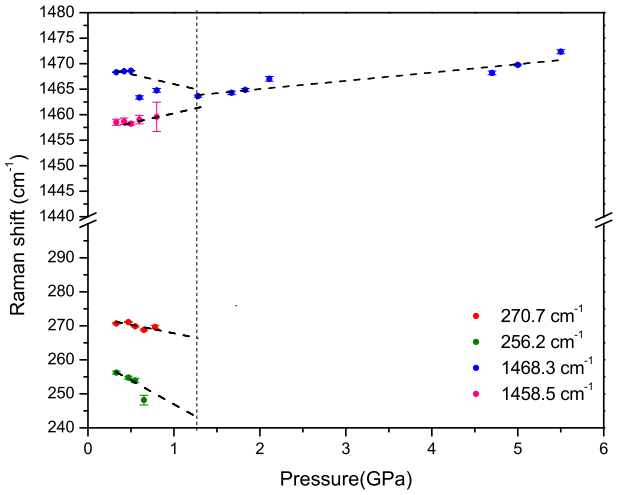

Figure 6.3: Pressure dependent Raman peak shifts observed for degenerated $H_g(1)$ mode (256.2 cm^{-1}, 270.7 cm^{-1}) and degenerated $A_g(2)$ mode(1458.5 cm^{-1}, 1468.3 cm^{-1}) of the C_{60} due to oxygen

6.2.1 Grüneisen parameter

The pressure dependence of the phonon frequency can be expressed through the isothermal mode Grüneisen parameter (γ_{iT}) defined as :

$$\begin{aligned} \gamma_{iT} &= \frac{B_T}{\nu_i}\left(\frac{d\nu_i}{dP}\right)_T \\ &= \frac{B_T}{\nu_i}\chi_P \end{aligned} \tag{6.3}$$

ν_i is the frequency of the i^{th} phonon peak and B_T is the bulk modulus. γ_{iT} can be estimated using the pressure coefficients χ_P for the phonon peaks and the reported B_T of C_{60} [204, 205]. At ambient pressure, Lundin *et al.* reported the room-temperature B_T as 6.8 GPa for the FCC phase of C_{60} and upon application of 1 GPa, the reported B_T was 9.5 GPa [205]. Whereas Ludwig *et al.* reported B_T as 13.4 GPa at 10 GPa applied pressure. In our work, γ_{iT} was calculated by considering B_T as 9.5 GPa up to 1.1 GPa while, B_T as 13.4 GPa was considered. The estimated γ_{iT} value for all the observed phonon peaks of $C_{60}O$ were compared with the reported γ_{iT} value of C_{60} and included in Table 6.2.

At 1.2 Gpa, γ_{iT} of all observed peak of $C_{60}O$ are found to be negative. Manghnani *et al.* reported negative Grüneisen parameter of cupric oxide (Cu_2O) which suggests crystal instability and impending phase transformation induced by pressure and/or temperature [206]. Instability of zirconium tungstate (ZrW_2O_8) crystal structure at 2.2 GPa also reported by its negative Grüneisen parameter [207]. It is known that FCC crystal structure of C_{60} is stable at ambient condition. However the presence of negative Grüneisen parameter in $C_{60}O$ infers structural instability upon application of pressure (<1.2 GPa). However, above 1.2 GPa, positive Grüneisen parameter explains structural stability in its SC structure(FCC-to-SC) like C_{60}. Above 1.2 GPa, positive γ_{iT} leads to expansion of crystal structure as intermolecular interaction increases. Meletov *et al.* reported their experimental data for pristine C_{60} by considering B_T as 14.4 GPa with 29 GPa applied pressure [208]. The comparison table (Table 6.2) indicated that above 1.2 GPa, γ_{iT} value of $C_{60}O$ cluster is smaller than pristine C_{60}. The effect of pressure on thermal conductivity can be explained by considering the contribution of Grüneisen parameter (discussed in Chapter 2). Lower the Grüneisen parameter, higher is the thermal conductivity. pressure induced polymerization in C_{60} films influences its thermal conductivity due to

Table 6.2: Phonon frequencies, pressure coefficients, and the Grüneisen parameters for $C_{60}O$ and pristine C_{60}.

$C_{60}O$						Pristine C_{60} [208]	
Phase I (P <1.2 GPa)			Phase II (1.2< P <5.5 GPa)			0.4< P <2.4 GPa	
ν_i (cm^{-1})	χ_P ($cm^{-1}GPa^{-1}$)	γ_{iT}	ν_i (cm^{-1})	χ_P ($cm^{-1}GPa^{-1}$)	γ_{iT}	ν_i (cm^{-1})	γ_{iT}
256.3	-14	-0.606	1463.8	1.6	0.015	272	0.165
270.7	-5	-0.205				1467	0.053
1458.5	4	0.031					
1468.3	-4	-0.030					

its modified Grüneisen parameter. It is reported that when C_{60} clusters are compressed above 0.3 GPa, its thermal conductivity increases [209]. The interaction potential of covalent bonds between neighboring fullerene cages may modify upon applied pressure that attributes to increase in Debye temperature and heat transport [107]. During polymerization of fullerene cage, the phonon density of states increases and hence its thermal conduction increases. The difference in thermal conductivity between the polymerized and unpolymerized state of C_{60} was reported to be about 10% [107]. The compressed fullerene molecules inside the carbon nanotube peapod structures increase their conductivities [101]. Thus, pressure induced polymerization in $C_{60}O$ films influences its thermal properties and the conductivity.

6.3 Pressure effects on Raman spectra of $C_{70}O$

Pressure dependent Raman spectroscopy of $C_{70}O$ was attempted by using 632.8 nm laser excitation. The observed spectra are illustrated in the Figure 6.4. At ambient pressure the peaks are observed at 226.7(1), 259.5(1) and 1564.6 cm^{-1}. As the split in 259.5(1) cm^{-1} peak was not observed using 632.8 nm excitation we could not examine the effects of pressure in C–O bond. However, pressure effect was examined on the observed peaks assigned to C_{70}. Raman spectra was studied by varying pressure up to 5.3 GPa shown

in Figure6.4.

Upon increasing the pressure to 5.3 K, all Raman peaks of $C_{70}O$ are found to be blue-shifted. 259.5 cm^{-1} peak is blue-shifted to 272.2 cm^{-1} at 1.4 GPa. At that amount of applied pressure, a new peak is observed at 290.1 cm^{-1}. Both 259.5 cm^{-1} and 290.1 cm^{-1} peaks are observed to be shifted linearly to higher frequencies with pressure up to 5.3 GPa. The observed shift in these Raman peaks with applied pressure is shown in Figure 6.5. The pressure induced shift of corresponding peaks are fitted by Eq.3.13 and the fitting parameters ν_0 and χ_P are tabulated in Table 6.3. The reported X-ray diffraction confirmed FCC-to-RH phase transition of C_{70} at 1.2 GPa which is also evident from our study [34, 35]. However, when pressure is increase up to 5.3 GPa, no further phase transition was observed. Nonexistence of splitting in 1564.6 peak indicated no polymerization in $C_{70}O$ up to 5.3 GPa. The pressure below 1.4 GPa is denoted as phase I and above 1.4 GPa it is denoted as phase II.

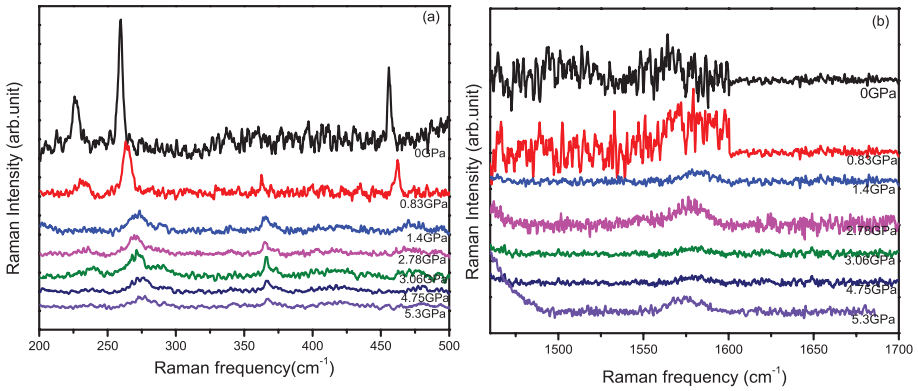

Figure 6.4: Pressure dependent Raman spectra of $C_{70}O$ measured up to 5.3 GPa using 632.8 nm laser excitation in the frequency range (a)200-500 cm^{-1} and (b)1450-1700 cm^{-1}

6.4 Conclusion

In this chapter, the pressure effect on lattice vibration of photo-polymerized $C_{60}O$ is examined. Pressure dependent red-shift in the low frequency Raman

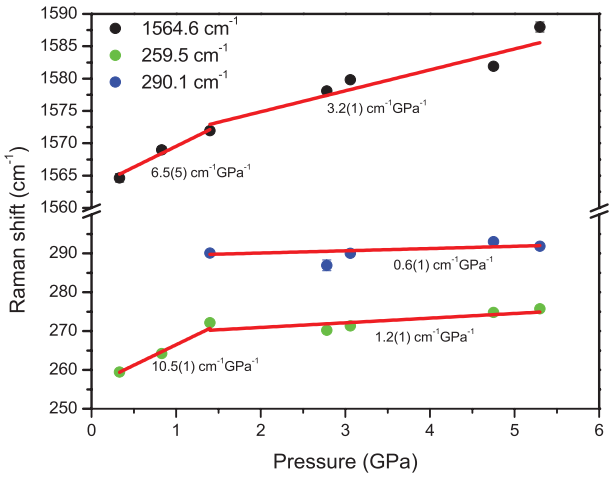

Figure 6.5: Pressure dependent Raman peak shifts observed for 259.5 cm^{-1} and 1564.6 cm^{-1}) of $C_{70}O$

Table 6.3: Pressure coefficients(χ_P) of different peaks of $C_{70}O$

Raman peaks (cm^{-1} at 1 atm)	χ_P (Phase I) (cm^{-1} GPa^{-1})	χ_P (Phase II) (cm^{-1} GPa^{-1})
259.5	10.5(1)	1.2(1)
290.1	–	0.6(1)
1564.6	6.5(5)	3.2(1)

peaks are ascribed to the reduced intra-molecular spacing and compression of the cluster. Above 0.3 GPa freezing in the rotational motion of the molecules is found. Above 1.2 GPa, the orientational phase transition of the cage occurred which lead to the polymerization of $C_{60}O$. This phase transition is found to be reversible with release of pressure. Pressure dependent Raman study of $C_{70}O$ is attempted although no peak assigned to C–O bond is observed.

Further, Grüneisen parameter is estimated for all observed phonon peaks of $C_{60}O$. Positive linear compressibility indicates contraction in single $C_{60}O$ molecule at 1.2 GPa. Negative γ_{iT} implies instability of crystal structure and the phase transformation of $C_{60}O$ up to 1.2 GPa. Whereas, positive γ_{iT} confirmed its stable struture above 1.2 GPa.

Both electronic as well as phononic interactions contribute to higher thermal conductivities of C_{60} dimers [210]. Having large Seebeck coefficients and

thermal conductivity, C_{60} dimers and their derivatives show smaller ZT as compared to single C_{60} molecule [210, 211]. Above 1.2 GPa, γ_{iT} value of $C_{60}O$ cluster is smaller than pristine C_{60}. Reduced γ_{iT} of $C_{60}O$ due to compression and polymerization indicates towards its increased thermal conductivity. Hence, the pressure induced structural changes in $C_{60}O$ molecules influences the thermal conductance which in turn may affects their thermoelectric efficiency.

Part IV

CONCLUSIONS

Chapter 7

Concluding remarks and future prospects

In this chapter, I have summarized the findings of my research work. Based on the conclusion drawn in this work, future prospects are also listed.

7.1 Concluding remarks

In the thrust to find potential material for thermoelectric applications under extreme condition, we investigated the thermal conductivity of $Gd@C_{82}$, $Dy@C_{82}$,$C_{60}O$ and $C_{70}O$ in this thesis. The effect of thermal and mechanical stress on lattice dynamics of these doped fullerenes and fullerene oxides are studied.

In this thesis magnetic and vibrational properties of two EMFs,$Gd@C_{82}$ and $Dy@C_{82}$ under thermal variation have been studied to understand the charge distribution between metal ion and the cage and their intra-molecular interactions (**Chapter 4**). Brillouin function approximation in magnetometry studies of $Gd@C_{82}$ and $Dy@C_{82}$ provides variation in the total angular momentum J of the incarcerated ion as function of temperature which helps in understanding the thermal variation in its oxidation state inside the fullerene cage. The

oxidation states of Gd and Dy ion are obtained to be invariant above 15 K and 40 K respectively suggesting no change in free electron transfer between the ion and cage above the corresponding temperatures. However, the thermal stress and associated anharmonicity are seen to modify the intra-molecular bonds which is noted from the low temperature and laser power induced Raman studies. Blue-shifts in Raman frequencies while decreasing the temperature in both metal-cage and cage internal vibrations of EMFs describe thermal contraction and anharmonic effect in the molecules. The increase in force constant of metal–cage vibration while lowering the temperature also confirms the contraction in intra-molecular bonds. Although, the linewidth of cage internal vibrations show minimal anharmonic interaction, metal-cage vibration linewidths are found to be strongly sensitive to temperature. Gd-cage line broadening is purely influenced by phonon-phonon interaction at low temperatures whereas, the contribution of electron-phonon interaction is dominant at low temperature in Dy-cage line broadening.

Two exohedral fullerenes, $C_{60}O$ (photo-polymerized) and $C_{70}O$ (unpolymerized) showed thermal contraction in their intra and inter-molecular bonds at low temperature (**Chapter 5**). By incorporating DFT calculation with the temperature dependent Raman shifts, the change in C-O bond-length of $C_{60}O$ was examined and its thermal expansion coefficient of $C_{60}O$ is found to be 30×10^{-6} K^{-1} which is larger than that of C_{60}. Positive isobaric mode Grüneisen parameter and thermal expansion coefficient suggest the positive volume expansion at 80 K in $C_{60}O$.

The effect of pressure on photo-polymerized $C_{60}O$ film is also performed to understand change in lattice vibrational properties due to intra and inter-molecular interactions (**Chapter 6**). The observed red-shift in the low frequency Raman peaks while increasing the pressure is ascribed to the reduced intra-molecular spacing and compression of the cluster. The positive linear

compressibility (0.186 GPa^{-1}) of $C_{60}O$ also suggests contraction in the cage at 1.2 GPa. The polymerization of $C_{60}O$ is further enhanced above 1.2 GPa. Negative γ_{iT} implies instability of crystal structure and the impending phase transformation of $C_{60}O$ below 1.2 GPa whereas, stable structure of the molecule is confirmed above 1.2 GPa by its positive γ_{iT}.

Thermal conductivity of Gd@C_{82}, Dy@C_{82}, $C_{60}O$ and $C_{70}O$ films are estimated by using the combinational effect of temperature and laser power on observed phonon frequencies (**Chapter 4 and 5**). Thermal conductivity of Gd@C_{82} and Dy@C_{82} are found to be weakly dependent on their phonon frequencies. Considering metal-cage vibration, thermal conductivity of Gd@C_{82} and Dy@C_{82} are observed to be 4.8 $Wm^{-1}K^{-1}$ and 2.3 $Wm^{-1}K^{-1}$. Thermal conductivity of $C_{60}O$ and $C_{70}O$ are found to be 0.7(2) $Wm^{-1}K^{-1}$ and 0.3(1) $Wm^{-1}K^{-1}$ which is nearly independent of their frequencies. Thermal conductivity of fullerene oxides are smaller than that of EMFs as they have mostly phonon contributions to the heat conduction which occurs via lattice vibrations of covalently bonded atoms. However, Gd@C_{82} and Dy@C_{82} have additional electron contribution to thermal conductivity due to the presence of free charge carriers on both ion as well as the cage which results in their higher thermal conductivity than that of undoped fullerenes.

7.2 Future prospects

In this work, temperature dependent lattice vibration was reported down to 80 K. As below 40 K, change in oxidation states of the ion inside the EMFs are observed. In future, one can explore the study down to 2 K by using liquid helium cooling system to understand the charge transfer between encaged ion and cage.

This work confirms low thermal conductivity of both $C_{60}O$ and $C_{70}O$ which

is prerequisite for higher figure of merit in thermoelectrics. Further exploration of their Seebeck coefficient and electrical conductance can be utilized to use these fullerene oxides as potential candidates in the thermoelectric devices.

This work provided an idea on Room and high temperature behaviour of thermal conductivity of the doped fullerenes and fullerene oxides. One can also explore the low temperature thermal conductivity behaviour in the fullerenes.

Due to pressure when fullerene cage gets compressed or polymerized, the phonon density of states increases and hence their thermal conduction increases. Here, it is proposed that the pressure induced structural changes in $C_{60}O$ molecules may modulate the carriers contribution to the thermal conductance which in turn affects their thermoelectric efficiency.

Appendix A

Appendix

Magnetic study of $C_{60}O$

In addition of this work, magnetometry study was performed on $C_{60}O$ and $C_{70}O$ dried powder. Samples of C_{60} (0.013 g) and $C_{60}O$ (0.006 g) were enclosed in a capsule. The centering of sample positions was carried out by sweeping the field from 0 to 100 Oe with a very small step. The magnetic measurements were performed by sweeping the field from 0 to 20000 Oe with 1000 Oe step.

To eliminate the error in the measured magnetic moment of the fullerenes due to the magnetic contribution from the background, the magnetisation of an empty capsule sealed with teflon tape was measured. Figure A.1 shows the magnetization of the empty capsule with the teflon tape at 300 K. The magnetization was found to be negative. The accurate magnetisation of C_{60} powder at 300 K is shown in Figure A.1 where the magnetic contribution of the empty capsule with the teflon tape was eliminated from the sample inside the capsule. For the pristine C_{60} powder, negative moment is observed throughout the temperature range 2-300 K shown in Figure A.2 revealing its diamagnetic

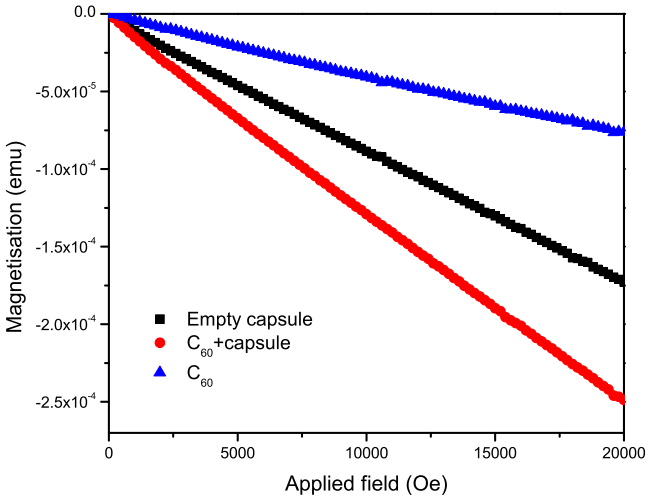

Figure A.1: Magnetization of C_{60} powder at 300 K as a function of applied magnetic field with and without background subtraction. The magnetization of the empty capsule is also shown on the graph for the comparison.

behaviour. The magnetic susceptibility of a material is defined as:

$$\chi = \frac{dM}{dH} \tag{A.1}$$

χ of C_{60} is found to be -3.8$\times$ 10^{-7} emu/g at 20000 Oe. The obtained value agrees with previous report [57]. At room temperature, $C_{60}O$ shows diamagnetic behavior. As obtained product consists of some traces of C_{60}, the magnetic contribution of C_{60} needs to be subtracted from $C_{60}O$. After eliminating the diamagnetic contribution of C_{60}, susceptibility of $C_{60}O$ is found to be -0.3 $\times$ 10^{-7} emu/g. The magnetization *M(H)* curve measured at 2 K and 300 K are shown in Figure A.3(a) for photo-polymerized $C_{60}O$. Magnetic hysteresis is observed for $C_{60}O$ with coercive field H_c=550 Oe and remanent magnetization M_r=3.22$\times 10^{-4}$ emu/g at 2 K. The presence of non-zero but small H_c indicates that $C_{60}O$ exhibit long-range and weak ferromagnetic interactions in the cluster.

temperature-dependent magnetizatic suseptibility of $C_{60}O$ was studied by

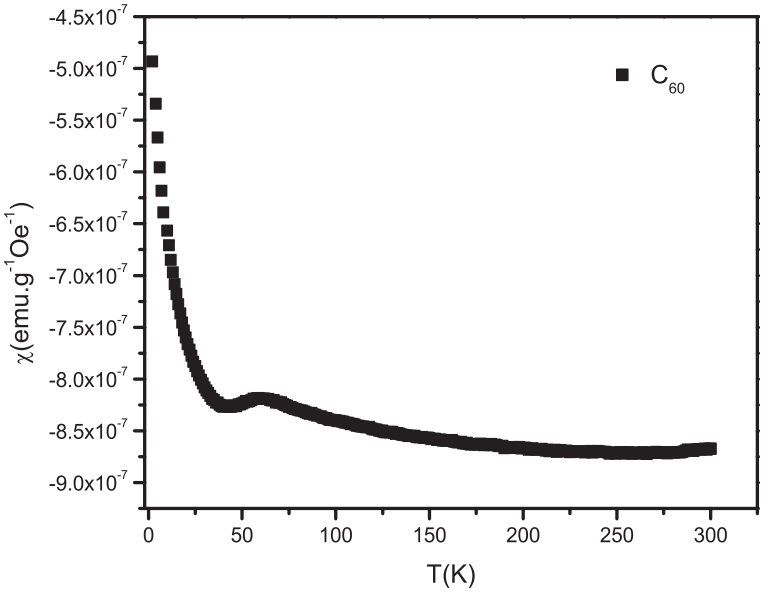

Figure A.2: Magnetic susceptibility of C_{60} as a function of temperature.

lowering the temperature to 2 K in zero-field cooled(ZFC) process at 1000Oe. It is found that below 50 K, magnetic moment becomes positive and increases gradually.

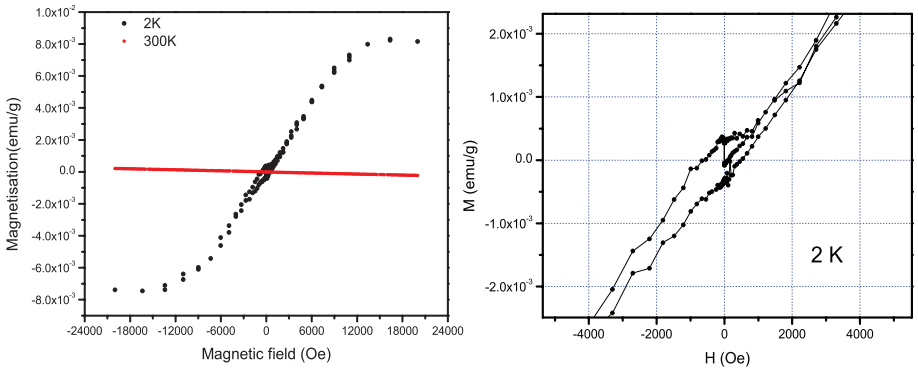

Figure A.3: Magnetization(M) as a function of the applied magnetic field (H) at T=2 K and 300K for $C_{60}O$.

Magnetic study of $C_{70}O$

Samples of C_{70} (0.003 g) and $C_{70}O$ (0.004 g) were enclosed in a capsule. The magnetic measurements were performed by sweeping the field from 0 to 30000 Oe with 1000 Oe step. Magnetic contribution of the capsule was ruled

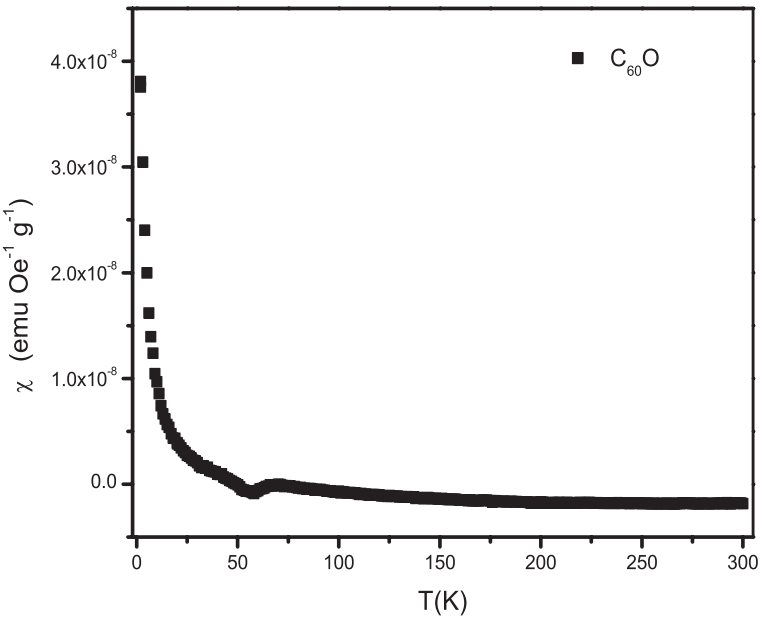

Figure A.4: Magnetic susceptibility of $C_{60}O$ as a function of temperature.

out from the samples by eliminating its diamagnetic susceptibility. The measurements were taken at 300 K and 2 K. Like pristine C_{60}, C_{70} also show diamagnetic behaviour. The diamagnetic susceptibility of C_{70} is found to be -6.1$\times$ 10^{-7} emu/g. The obtained value is comparable with the previously reported data [58]. After eliminating diamagnetic contribution of C_{70}, susceptibility of $C_{70}O$ is obtained to be -2.5 $\times$ 10^{-7} emu/g at 20000 Oe. The *M(H)* curve mea-

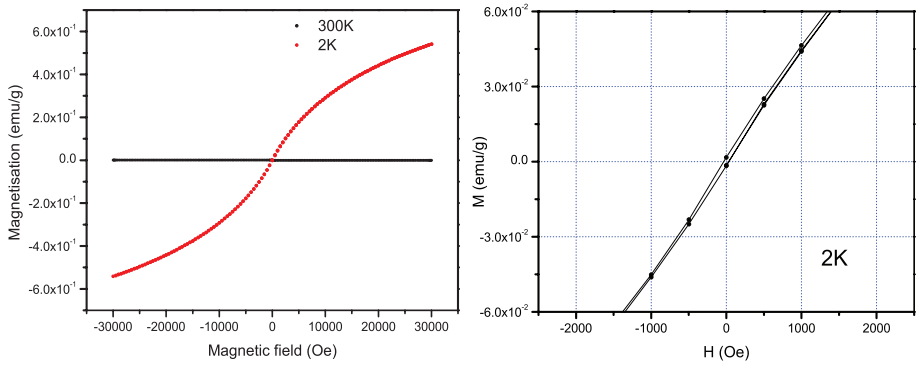

Figure A.5: Magnetization(M) as a function of the applied magnetic field (H) at T=2 K and 300K for $C_{70}O$.

sured at 2 K and 300 K are shown in Figure A.5 for $C_{70}O$. Magnetic hysteresis is observed for $C_{70}O$ with H_c=35 Oe and M_r=1.8$\times$$10^{-3}$ emu/g at 2 K. The

presence of non-zero but small H_c indicates that $C_{70}O$ exhibit weak long-range magnetic interactions in the cluster. To understand the magnetic behavior,

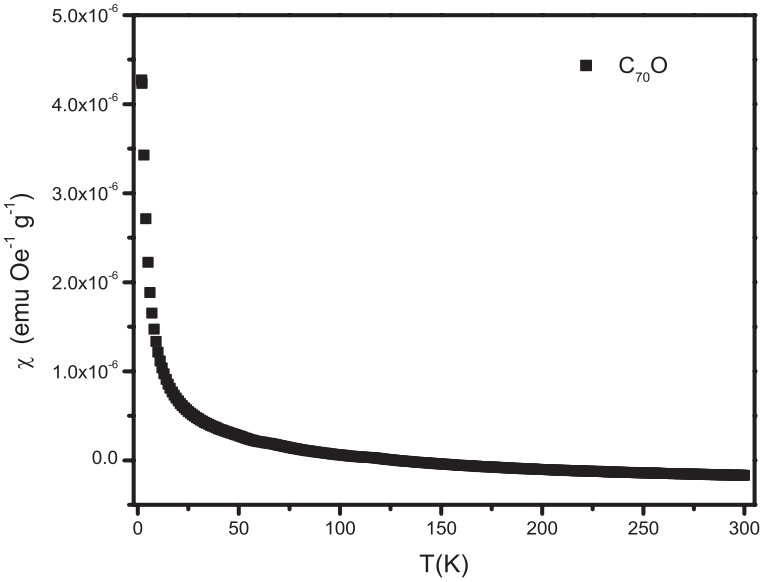

Figure A.6: Magnetic susceptibility of $C_{70}O$ as a function of temperature.

the temperature-dependent magnetization of $C_{70}O$ was studied by lowering the temperature to 2 K in a zero-field cooled(ZFC) process. Magnetic moment was found to be positive below 120 K and increased gradually down to 2 K. It is thus quite obvious that some magnetic interaction is growing in the system below 120 K.

Bibliography

[1] L Chen, X Wang, and S Kumar. Thermal transport in fullerene derivatives using molecular dynamics simulations. *Scientific Reports*, 5:12763, 2015.

[2] R Koeppe and NS Sariciftci. Photoinduced charge and energy transfer involving fullerene derivatives. *Photochemical & Photobiological Sciences*, 5(12):1122–1131, 2006.

[3] Raman spectroscopy. accessed 10th Jan. 2018.

[4] AM Welsch. *High-pressure Raman scattering of pure and doped* $PbSc_{0.5}Ta_{0.5}O_3$ *and* $PbSc_{0.5}Nb_{0.5}O_3$ *single crystals*. PhD thesis, University of Hamburg, 2009.

[5] G Cardini, R Bini, P R Salvi, V Schettino, M L Klein, R M Strongin, L Brard, and A B Smith III. Infrared spectrum of two fullerene derivatives: $C_{60}O$ and $C_{61}H_2$. *The Journal of Physical Chemistry*, 98(40):9966–9971, 1994.

[6] R Miletich, DR Allan, and WF Kuhs. High-pressure single-crystal techniques. *Reviews in Mineralogy and Geochemistry*, 41(1):445–519, 2000.

[7] RJ Angel, M Bujak, J Zhao, GD Gatta, and SD Jacobsen. Effective hydrostatic limits of pressure media for high-pressure crystallographic studies. *Journal of Applied Crystallography*, 40(1):26–32, 2007.

[8] S Klotz, JC Chervin, P Munsch, and G Le Marchand. Hydrostatic limits of 11 pressure transmitting media. *Journal of Physics D: Applied Physics*, 42(7):075413, 2009.

[9] GA Slack. New materials and performance limits for thermoelectric cooling. *CRC handbook of thermoelectrics*, pages 407–440, 1995.

[10] K Zhang, Y Zhang, and S Wang. Enhancing thermoelectric properties of organic composites through hierarchical nanostructures. *Scientific Reports*, 3:3448, 2013.

[11] LD Hicks and MS Dresselhaus. Thermoelectric figure of merit of a one-dimensional conductor. *Physical Review B*, 47(24):16631, 1993.

[12] A Shakouri. Nanoscale thermal transport and microrefrigerators on a chip. *Proceedings of the IEEE*, 94(8):1613–1638, 2006.

[13] CJ Vineis, A Shakouri, A Majumdar, and MG Kanatzidis. Nanostructured thermoelectrics: big efficiency gains from small features. *Advanced Materials*, 22(36):3970–3980, 2010.

[14] MS Dresselhaus, G Chen, MY Tang, RG Yang, H Lee, DZ Wang, ZF Ren, JP Fleurial, et al. New directions for low-dimensional thermoelectric materials. *Advanced Materials*, 19(8):1043–1053, 2007.

[15] VD Blank, SG Buga, VA Kulbachinskii, VG Kytin, VV Medvedev, M Yu Popov, PB Stepanov, and VF Skok. Thermoelectric properties of $Bi_{0.5}Sb_{1.5}Te_3/C_{60}$ nanocomposites. *Physical Review B*, 86(7):075426, 2012.

[16] X Shi, LD Chen, SQ Bai, XY Huang, XY Zhao, Q Yao, and C Uher. Influence of fullerene dispersion on high temperature thermoelectric prop-

erties of $Ba_yCo_4Sb_{12}$-based composites. *Journal of Applied Physics*, 102(10):103709, 2007.

[17] M Popov, S Buga, P Vysikaylo, P Stepanov, V Skok, V Medvedev, E Tatyanin, V Denisov, A Kirichenko, V Aksenenkov, et al. C_{60}-doping of nanostructured Bi–Sb–Te thermoelectrics. *Physica Status Solidi (a)*, 208(12):2783–2789, 2011.

[18] D Zhao, J Ning, S Li, and M Zuo. Synthesis and thermoelectric properties of C_{60}/Cu_2GeSe_3 composites. *Journal of Nanomaterials*, 2016:1–7, 2016.

[19] Z Chen, X Zhang, S Lin, L Chen, and Y Pei. Rationalizing phonon dispersion for lattice thermal conductivity of solids. *National Science Review*, 5(6):888–894, 2018.

[20] A Giri and PE Hopkins. Spectral contributions to the thermal conductivity of C_{60} and the fullerene derivative PCBM. *The Journal of Physical Chemistry Letters*, 8(10):2153–2157, 2017.

[21] C Evangeli, K Gillemot, E Leary, MT Gonzalez, G Rubio-Bollinger, CJ Lambert, and N Agrait. Engineering the thermopower of C_{60} molecular junctions. *Nano Letters*, 13(5):2141–2145, 2013.

[22] HW Kroto, JR Heath, SC O'Brien, RF Curl, and RE Smalley. C_{60}: Buckminsterfullerene. *Nature*, 318(6042):162, 1985.

[23] R Taylor and DRM Walton. The chemistry of fullerenes. *Nature*, 363(6431):685, 1993.

[24] HW Kroto. The stability of the fullerenes C_n, with n= 24, 28, 32, 36, 50, 60 and 70. *Nature*, 329(6139):529, 1987.

[25] TG Schmalz, WA Seitz, DJ Klein, and GE Hite. Elemental carbon cages. *Journal of the American Chemical Society*, 110(4):1113–1127, 1988.

[26] BL Zhang, CZ Wang, KM Ho, CH Xu, and CT Chan. The geometry of large fullerene cages: C_{72} to C_{102}. *Journal of chemical physics*, 98(4):3095–3102, 1993.

[27] PA Heiney, JE Fischer, AR McGhie, WJ Romanow, AM Denenstein, JP McCauley Jr, et al. Orientational ordering transition in solid C_{60}. *Physical Review Letters*, 66(22):2911, 1991.

[28] JE Fischer, PA Heiney, AR McGhie, WJ Romanow, AM Denenstein, JP McCauley, and AB Smith. Compressibility of solid C_{60}. *Science*, 252(5010):1288–1290, 1991.

[29] MS Dresselhaus, G Dresselhaus, and PC Eklund. *Science of fullerenes and carbon nanotubes: their properties and applications*. Elsevier, 1996.

[30] W David, RM Ibberson, TJS Dennis, JP Hare, and K Prassides. Structural phase transitions in the fullerene C_{60}. *Europhysics Letters*, 18(3):219, 1992.

[31] M Álvarez-Murga and JL Hodeau. Structural phase transitions of C_{60} under high-pressure and high-temperature. *Carbon*, 82:381–407, 2015.

[32] RM Fleming, AR Kortan, B Hessen, T Siegrist, FA Thiel, P Marsh, RC Haddon, R Tycko, G Dabbagh, ML Kaplan, et al. Pseudotenfold symmetry in pentane-solvated C_{60} and C_{70}. *Physical Review B*, 44(2):888, 1991.

[33] GBM Vaughan, PA Heiney, DE Cox, JE Fischer, AR McGhie, AL Smith, et al. Structural phase transitions and orientational ordering in C_{70}. *Chemical physics*, 178(1-3):599–613, 1993.

[34] H Kawamura, M Kobayashi, Y Akahama, H Shinohara, H Sato, and Y Saito. Orientational ordering in solid C_{70} under high pressure. *Solid state communications*, 83(8):563–565, 1992.

[35] A Lundin, A Soldatov, and B Sundqvist. Compressibility and structure of C_{70}. *Europhysics Letters*, 30(8):469, 1995.

[36] H Kawada, Y Fujii, H Nakao, Y Murakami, T Watanuki, H Suematsu, K Kikuchi, Y Achiba, and I Ikemoto. Structural aspects of C_{82} and C_{76} crystals studied by X-ray diffraction. *Physical Review B*, 51(14):8723, 1995.

[37] H Shinohara and N Tagmatarchis. *Endohedral metallofullerenes: Fullerenes with metal inside*. John Wiley & Sons, 2015.

[38] JI Aihara. Correlation found between the HOMO–LUMO energy separation and the chemical reactivity at the most reactive site for isolated-pentagon isomers of fullerenes. *Physical Chemistry Chemical Physics*, 2(14):3121–3125, 2000.

[39] DE Manolopoulos, JC May, and SE Down. Theoretical studies of the fullerenes: C_{34} to C_{70}. *Chemical Physics Letters*, 181(2-3):105–111, 1991.

[40] M Sola, J Mestres, and M Duran. Molecular size and pyramidalization: two keys for understanding the reactivity of fullerenes. *The Journal of Physical Chemistry*, 99(27):10752–10758, 1995.

[41] Y Yang, F Arias, L Echegoyen, LPF Chibante, S Flanagan, A Robertson, and LJ Wilson. Reversible fullerene electrochemistry: correlation with the HOMO-LUMO energy difference for C_{60}, C_{70}, C_{76}, C_{78}, and C_{84}. *Journal of the American Chemical Society*, 117(29):7801–7804, 1995.

[42] KM Creegan, JL Robbins, WK Robbins, JM Millar, RD Sherwood, PJ Tindall, DM Cox, JP McCauley Jr, and DR Jones. Synthesis and characterization of $C_{60}O$, the first fullerene epoxide. *Journal of the American Chemical Society*, 114(3):1103–1105, 1992.

[43] AM Rao, P Zhou, KA Wang, GT Hager, JM Holden, Y Wang, WT Lee, XX Bi, PC Eklund, DS Cornett, et al. Photoinduced polymerization of solid C_{60} films. *Science*, pages 955–957, 1993.

[44] RB Weisman, D Heymann, and SM Bachilo. Synthesis and characterization of the "missing" oxide of C_{60}:[5,6]-open $C_{60}O$. *Journal of the American Chemical Society*, 123(39):9720–9721, 2001.

[45] R Dattani, KF Gibson, S Few, AJ Borg, PA DiMaggio, J Nelson, SG Kazarian, and J Cabral. Fullerene oxidation and clustering in solution induced by light. *Journal of colloid and interface science*, 446:24–30, 2015.

[46] D Heymann. Ozonides and oxides of C_{60} and C_{70}: A review. *Fullerenes, Nanotubes and Carbon Nanostructures*, 12:715–729, 2004.

[47] S Saito and A Oshiyama. Cohesive mechanism and energy bands of solid C_{60}. *Physical Review Letters*, 66(20):2637, 1991.

[48] K Raghavachari. Structure of $C_{60}O$: unexpected ground state geometry. *Chemical physics letters*, 195(2-3):221–224, 1992.

[49] WY Sohn, TW Kim, and JS Lee. Structure and energetics of $C_{60}O$: a theoretical study. *The Journal of Physical Chemistry A*, 114(4):1939–1943, 2010.

[50] BC Wang, L Chen, and YM Chou. Theoretical studies of C_{60}/C_{70} fullerene derivatives: $C_{60}O$ and $C_{70}O$. *Journal of Molecular Structure: THEOCHEM*, 422(1-3):153–158, 1998.

[51] D Heymann, SM Bachilo, and RB Weisman. Ozonides, epoxides, and oxidoannulenes of C_{70}. *Journal of the American Chemical Society*, 124(22):6317–6323, 2002.

[52] D S Bethune, G Meijer, Wade C Tang, and Hal J Rosen. The vibrational raman spectra of purified solid films of C_{60} and C_{70}. *Chemical Physics Letters*, 174(3-4):219–222, 1990.

[53] V Schettino, M Pagliai, and G Cardini. The infrared and raman spectra of fullerene C_{70}. DFT calculations and correlation with C_{60}. *The Journal of Physical Chemistry A*, 106(9):1815–1823, 2002.

[54] M Krause, L Dunsch, G Seifert, P W Fowler, A Gromov, W Krätschmer, R Gutierez, D Porezag, and T Frauenheim. Vibrational signatures of fullerene oxides. *Journal of the Chemical Society, Faraday Transactions*, 94(16):2287–2294, 1998.

[55] DS Bethune, G Meijer, WC Tang, HJ Rosen, WG Golden, H Seki, CA Brown, and MS de Vries. Vibrational raman and infrared spectra of chromatographically separated C_{60} and C_{70} fullerene clusters. *Chemical Physics Letters*, 179(1-2):181–186, 1991.

[56] RC Haddon, LF Schneemeyer, JV Waszczak, SH Glarum, R Tycko, G Dabbagh, AR Kortan, AJ Muller, AM Mujsce, MJ Rosseinsky, et al. Experimental and theoretical determination of the magnetic susceptibility of C_{60} and C_{70}. *Nature*, 350(6313):46, 1991.

[57] RS Ruoff, D Beach, J Cuomo, T McGuire, RL Whetten, and F Diederich. Confirmation of a vanishingly small ring-current magnetic susceptibility

of icosahedral buckminsterfullerene. *The Journal of Physical Chemistry*, 95(9):3457–3459, 1991.

[58] J Heremans, CH Olk, and DT Morelli. Magnetic susceptibility of carbon structures. *Physical Review B*, 49(21):15122, 1994.

[59] Y Murakami and H Suematsu. Magnetism of C_{60} induced by photo-assisted oxidation. *Pure and Applied Chemistry*, 68(7):1463–1467, 1996.

[60] TL Makarova, KH Han, P Esquinazi, RR Da Silva, Y Kopelevich, IB Zakharova, and B Sundqvist. Magnetism in photopolymerized fullerenes. *Carbon*, 41(8):1575–1584, 2003.

[61] FJ Owens, Z Iqbal, L Belova, and KV Rao. Evidence for high-temperature ferromagnetism in photolyzed C_{60}. *Physical Review B*, 69(3):033403, 2004.

[62] A Kumar, DK Avasthi, JC Pivin, A Tripathi, and F Singh. Ferromagnetism induced by heavy-ion irradiation in fullerene films. *Physical Review B*, 74(15):153409, 2006.

[63] H Shinohara. Endohedral metallofullerenes. *Reports on Progress in Physics*, 63(6):843, 2000.

[64] AA Popov. Metal-cage bonding, molecular structures and vibrational spectra of endohedral fullerenes: bridging experiment and theory. *Journal of Computational and Theoretical Nanoscience*, 6(2):292–317, 2009.

[65] JR Heath, SC O'brien, Q Zhang, Y Liu, RF Curl, FK Tittel, and RE Smalley. Lanthanum complexes of spheroidal carbon shells. *Journal of the American Chemical Society*, 107(25):7779–7780, 1985.

[66] Y Chai, T Guo, C Jin, R E Haufler, LP F Chibante, J Fure, L Wang, J M Alford, and R E Smalley. Fullerenes with metals inside. *The Journal of Physical Chemistry*, 95(20):7564–7568, 1991.

[67] EG Gillan, C Yeretzian, KS Min, MM Alvarez, RL Whetten, and RB Kaner. Endohedral rare-earth fullerene complexes. *The Journal of Physical Chemistry*, 96(17):6869–6871, 1992.

[68] FD Weiss, JL Elkind, SC O'Brien, RF Curl, and RE Smalley. Photophysics of metal complexes of spheroidal carbon shells. *Journal of the American Chemical Society*, 110(13):4464–4465, 1988.

[69] M Takata, B Umeda, E Nishibori, M Sakata, Y Saitot, M Ohno, and H Shinohara. Confirmation by X-ray diffraction of the endohedral nature of the metallofullerene Y@C_{82}. *Nature*, 377(6544):46, 1995.

[70] K Kobayashi and S Nagase. Structures and electronic states of M@C_{82} (M= Sc, Y, La and lanthanides). *Chemical physics letters*, 282(3-4):325–329, 1998.

[71] T Watanuki, A Fujiwara, K Ishii, Y Matuoka, H Suematsu, K Ohwada, H Nakao, Y Fujii, T Kodama, K Kikuchi, et al. Structural phase transitions of endohedral metallofullerene La@C_{82} studied by single crystal x-ray diffraction. *Molecular Crystals and Liquid Crystals Science and Technology. Section A. Molecular Crystals and Liquid Crystals*, 340(1):639–642, 2000.

[72] Y Kubozono, Y Takabayashi, K Shibata, T Kanbara, S Fujiki, S Kashino, A Fujiwara, and S Emura. Crystal structure and electronic transport of Dy@C_{82}. *Physical Review B*, 67(11):115410, 2003.

[73] E. Nishibori, K. Iwata, and M Sakata. Anomalous endohedral structure of Gd@C_{82} metallofullerenes. *Physical Review B*, 69:113412, 2004.

[74] BY Sun, T Sugai, E Nishibori, K Iwata, M Sakata, M Takata, and H Shinohara. An anomalous endohedral structure of Eu@C_{82} metallofullerenes. *Angewandte Chemie International Edition*, 44(29):4568–4571, 2005.

[75] A Bartl, L Dunsch, J Fröhner, and U Kirbach. New electron spin resonance and mass spectrometric studies of metallofullerenes. *Chemical physics letters*, 229(1-2):115–121, 1994.

[76] A Bartl, L Dunsch, and U Kirbach. Preparation, mass spectrometry and solid state ESR spectroscopy of endohedral fullerenes. *Solid state communications*, 94(10):827–831, 1995.

[77] A Bartl, L Dunsch, and U Kirbach. Electron transfer at lanthanum endohedral fullerenes. *Applied Magnetic Resonance*, 11(2):301–314, 1996.

[78] J Lu, X Zhang, X Zhao, S Nagase, and K Kobayashi. Strong metal-cage hybridization in endohedral La@C_{82}, Y@C_{82} and Sc@C_{82}. *Chemical Physics Letters*, 332(3-4):219–224, 2000.

[79] M Takata, E Nishibori, M Sakata, and H Shinohara. Synchrotron radiation for structural chemistryendohedral natures of metallofullerenes found by synchrotron radiation powder method. *Structural Chemistry*, 14(1):23–38, 2003.

[80] X Dai, Y Gao, M Xin, Z Wang, and R Zhou. The ground state and electronic structure of Gd@C_{82}: A systematic theoretical investigation of first principle density functionals. *The Journal of chemical physics*, 141(24):244306, 2014.

[81] L Senapati, J Schrier, and K B Whaley. Electronic transport, structure, and energetics of endohedral Gd@C_{82} metallofullerenes. *Nano Letters*, 4(11):2073–2078, 2004.

[82] S. Lebedkin, B. Renker, R. R.Heid, H. Schober, and H. Rietschel. A spectroscopic study of M@C_{82} metallofullerenes: Raman, far-infrared, and neutron scattering results. *Appl. Phys. A*, 66:273280, 1998.

[83] M Krause, M Hulman, H Kuzmany, TJS Dennis, M Inakuma, and H Shinohara. Diatomic metal encapsulates in fullerene cages: a Raman and infrared analysis of C_{84} and $Sc_2@C_{84}$ with D 2d symmetry. *The Journal of Chemical Physics*, 111(17):7976–7984, 1999.

[84] K Kobayashi and S Nagase. Theoretical calculations of vibrational modes in endohedral metallofullerenes: La@C_{82} and $Sc_2@C_{84}$. *Molecular Physics*, 101(1-2):249–254, 2003.

[85] H Funasaka, K Sugiyama, K Yamamoto, and T Takahashi. Magnetic properties of rare-earth metallofullerenes. *The Journal of Physical Chemistry*, 99(7):1826–1830, 1995.

[86] HJ Huang, SH Yang, and XX Zhang. Magnetic properties of heavy rare-earth metallofullerenes M@C_{82} (M =Gd, Tb, Dy, Ho, and Er). *J. Phys. Chem. B*, 104:1473–1482, 2000.

[87] BA Weinstein and R Zallen. Pressure-Raman effects in covalent and molecular solids. In *Light Scattering in Solids IV*, pages 463–527. Springer, 1984.

[88] G Lucazeau. Effect of pressure and temperature on Raman spectra of solids: anharmonicity. *Journal of Raman Spectroscopy*, 34(7-8):478–496, 2003.

[89] Z Zhao, J Elwood, and MA Carpenter. Phonon anharmonicity of PdO studied by Raman spectrometry. *The Journal of Physical Chemistry C*, 119(40):23094–23102, 2015.

[90] PG Klemens. Anharmonic decay of optical phonons. *Physical Review*, 148(2):845, 1966.

[91] I Chatzakis, H Yan, D Song, S Berciaud, and TF Heinz. Temperature dependence of the anharmonic decay of optical phonons in carbon nanotubes and graphite. *Physical Review B*, 83(20):205411, 2011.

[92] M Krause, M Hulman, H Kuzmany, TJS Dennis, M Inakuma, and H Shinohara. Diatomic metal encapsulates in fullerene cages: a raman and infrared analysis of C_{84} and $Sc_2@C_{84}$ with D_{2d} symmetry. *The Journal of Chemical Physics*, 111(17):7976–7984, 1999.

[93] A Debernardi, C Ulrich, M Cardona, and K Syassen. Pressure dependence of Raman linewidth in semiconductors. *Physica status solidi (b)*, 223(1):213–223, 2001.

[94] Z Yao, J Zhang, MG Yao, SL Chen, and BB Liu. Effect of high pressure on the transformations of ferrocene-filled, single-wall, carbon nanotubes: Density functional theory and Raman spectroscopy studies. *The Journal of Physical Chemistry C*, 120(40):23189–23196, 2016.

[95] SH Tolbert, AP Alivisatos, HE Lorenzana, MB Kruger, and R Jeanloz. Raman studies on C_{60} at high pressures and low temperatures. *Chemical physics letters*, 188(3-4):163–167, 1992.

[96] GP Srivastava. *The physics of phonons*. CRC press, 1990.

[97] M Shamsa, S Ghosh, I Calizo, V Ralchenko, A Popovich, and AA Balandin. Thermal conductivity of nitrogenated ultrananocrystalline diamond films on silicon. *Journal of Applied Physics*, 103(8):083538, 2008.

[98] L Braginsky, N Lukzen, V Shklover, and H Hofmann. High-temperature phonon thermal conductivity of nanostructures. *Physical Review B*, 66(13):134203, 2002.

[99] J Hone, M Whitney, C Piskoti, and A Zettl. Thermal conductivity of single-walled carbon nanotubes. *Physical Review B*, 59(4):R2514, 1999.

[100] Y Gao and B Xu. Probing thermal conductivity of fullerene C_{60} hosting a single water molecule. *The Journal of Physical Chemistry C*, 119(35):20466–20473, 2015.

[101] T Kodama, M Ohnishi, W Park, T Shiga, J Park, T Shimada, H Shinohara, J Shiomi, and K E Goodson. Modulation of thermal and thermoelectric transport in individual carbon nanotubes by fullerene encapsulation. *Nature materials*, 16(9):892, 2017.

[102] GA Slack. The thermal conductivity of nonmetallic crystals. In *Solid state physics*, volume 34, pages 1–71. Elsevier, 1979.

[103] ZH Fang. Pressure dependence of Grüneisen parameter in solids. *Physica Status Solidi (b)*, 197(1):39–43, 1996.

[104] GL Cui and RL Yu. Volume and pressure dependence of Grüneisen parameter γ for solids at high temperatures. *Physica B: Condensed Matter*, 390(1-2):220–224, 2007.

[105] XC Peng, LL Xing, and ZH Fang. Comparing research on the pressure or volume dependence of Grüneisen parameter. *Physica B: Condensed Matter*, 394(1):111–114, 2007.

[106] Q Liu, L Chen, et al. Pressure dependence of the Grüneisen parameter and thermal expansion coefficient of solids. *Indian Journal of Pure and Applied Physics*, 55(5):368–371, 2017.

[107] A Soldatov and O Andersson. Thermal conductivity of pressure polymerized C_{60}. *Applied Physics A*, 64(3):227–229, 1997.

[108] DG Cahill, SK Watson, and RO Pohl. Lower limit to the thermal conductivity of disordered crystals. *Physical Review B*, 46(10):6131, 1992.

[109] R Yan, JR Simpson, S Bertolazzi, J Brivio, M Watson, X Wu, A Kis, T Luo, et al. Thermal conductivity of monolayer molybdenum disulfide obtained from temperature-dependent Raman spectroscopy. *ACS Nano*, 8(1):986–993, 2014.

[110] S Sahoo, VR Chitturi, R Agarwal, JW Jiang, and RS K. Thermal conductivity of freestanding single wall carbon nanotube sheet by Raman spectroscopy. *ACS applied materials & interfaces*, 6(22):19958–19965, 2014.

[111] R Agarwal, S Sahoo, VR Chitturi, and RS Katiyar. Graphitic carbon nanospheres: A Raman spectroscopic investigation of thermal conductivity and morphological evolution by pulsed laser irradiation. *Journal of Applied Physics*, 118(21):214301, 2015.

[112] S Perichon, V Lysenko, B Remaki, D Barbier, and B Champagnon. Measurement of porous silicon thermal conductivity by micro-Raman scattering. *Journal of Applied Physics*, 86(8):4700–4702, 1999.

[113] M Nonnenmacher and HK Wickramasinghe. Scanning probe microscopy of thermal conductivity and subsurface properties. *Applied Physics Letters*, 61(2):168–170, 1992.

[114] S Huang, XD Ruan, X Fu, and HY Yang. Measurement of the thermal transport properties of dielectric thin films using the micro-Raman method. *Journal of Zhejiang University-SCIENCE A*, 10(1):7–16, 2009.

[115] B Stoib, S Filser, J Stötzel, A Greppmair, N Petermann, H Wiggers, G Schierning, M Stutzmann, and MS Brandt. Spatially resolved determination of thermal conductivity by Raman spectroscopy. *Semiconductor Science and Technology*, 29(12):124005, 2014.

[116] H Malekpour and AA Balandin. Raman-based technique for measuring thermal conductivity of graphene and related materials. *Journal of Raman Spectroscopy*, 49(1):106–120, 2018.

[117] V Lysenko, S Perichon, B Remaki, D Barbier, and B Champagnon. Thermal conductivity of thick meso-porous silicon layers by micro-Raman scattering. *Journal of Applied Physics*, 86(12):6841–6846, 1999.

[118] W Krätschmer, LD Lamb, K Fostiropoulos, and DR Huffman. Solid C_{60}: a new form of carbon. *Nature*, 347(6291):354, 1990.

[119] H Shinohara, M Takata, M Sakata, T Hashizume, and T Sakurai. Metallofullerenes: their formation and characterization. In *Materials Science Forum*, volume 232, pages 207–232, 1996.

[120] N Tagmatarchis and H Shinohara. Production, separation, isolation, and spectroscopic study of dysprosium endohedral metallofullerenes. *Chemistry of Materials*, 12(10):3222–3226, 2000.

[121] H Shinohara, H Yamaguchi, N Hayashi, H Sato, M Ohkohchi, Y Ando, and Y Saito. Isolation and spectroscopic properties of scandium fullerenes ($Sc_2@C_{74}$, $Sc_2@C_{82}$, and $Sc_2@C_{82}$). *The Journal of Physical Chemistry*, 97(17):4259–4261, 1993.

[122] X Lu, H Li, B Sun, Z Shi, and Z Gu. Selective reduction and extraction of $Gd@C_{82}$ and $Gd_2@C_{80}$ from soot and the chemical reaction of their anions. *Carbon*, 43(7):1546–1549, 2005.

[123] `http://winter.group.shef.ac.uk/chemputer/isotopes.html`. Accessed April 4, 2017.

[124] D Heymann and LPF Chibante. Photo-transformations of C_{60}, C_{70}, $C_{60}O$, and $C_{60}O_2$. *Chemical Physics Letters*, 207(4-6):339–342, 1993.

[125] WB Ko and KN Baek. The oxidation of fullerenes (C_{60}, C_{70}) with various oxidants under ultrasonication. *Physics of the Solid State*, 44(3):424–426, 2002.

[126] G Tojo and MI Fernández. *Oxidation of alcohols to aldehydes and ketones: a guide to current common practice*. Springer Science & Business Media, 2006.

[127] DJ Dumin. Measurement of film thickness using infrared interference. *Review of Scientific Instruments*, 38(8):1107–1109, 1967.

[128] S Jitian. The determination of thickness and optical constants for PbSe film from IR reflectance spectra. *Annals of the Faculty of Engineering Hunedoara*, 9(3):153, 2011.

[129] Some properties of carbon and C_{60}. `http://www.creative-science.org.uk/propc60.html`. Accessed April 4, 2016.

[130] CV Raman and KS Krishnan. A new type of secondary radiation. *Nature*, 121(3048):501–502, 1928.

[131] DA Skoog, FJ Holler, and SR Crouch. *Principle of Instrumental analysis*. Brooks/Cole, Cengage Learning Belmont, 2006.

[132] E Smith and G Dent. *Modern Raman spectroscopy: a practical approach*. John Wiley & Sons, 2013.

[133] K Venkateswarlu. Relative intensities of stokes and anti-stokes Raman lines in crystals. In *Proceedings of the Indian Academy of Sciences-Section A*, volume 13, pages 64–67. Springer, 1941.

[134] Renishaw inVia Raman microscope. Acessed 16th Sept. 2018.

[135] CA Palmer and EG Loewen. *Diffraction grating handbook*. Newport Corporation New York, 2005.

[136] D Tuschel. Selecting an excitation wavelength for Raman spectroscopy. *Spectroscopy*, 31.

[137] Gaussian beam optics. `www.cvilaseroptics.com`. Acessed 28th Sept. 2018.

[138] H Sun. Thin lens equation for a real laser beam with weak lens aperture truncation. *Optical Engineering*, 37(11):2906–2914, 1998.

[139] THMS600 heating and freezing stage. Acessed 18th Sept., 2017.

[140] DJ Dunstan and IL Spain. Technology of diamond anvil high-pressure cells: I. principles, design and construction. *Journal of Physics E: Scientific Instruments*, 22(11):913, 1989.

[141] MI Eremets. *High pressure experimental methods*. Oxford University Press, 1996.

[142] MI Eremets, IA Trojan, P Gwaze, J Huth, R Boehler, and VD Blank. The strength of diamond. *Applied Physics Letters*, 87(14):141902, 2005.

[143] CD Esposti and L Bizzocchi. Absorption and emission spectroscopy of a lasing material: Ruby. *Journal of Chemical Education*, 84(8):1316, 2007.

[144] K Syassen. Ruby under pressure. *High Pressure Research*, 28(2):75–126, 2008.

[145] AD Chijioke, WJ Nellis, A Soldatov, and IF Silvera. The ruby pressure standard to 150 GPa. *Journal of Applied Physics*, 98(11):114905, 2005.

[146] HK Mao, J-A Xu, and PM Bell. Calibration of the ruby pressure gauge to 800 kbar under quasi-hydrostatic conditions. *Journal of Geophysical Research: Solid Earth*, 91(B5):4673–4676, 1986.

[147] GJ Piermarini, S Block, JD Barnett, and RA Forman. Calibration of the pressure dependence of the R1 ruby fluorescence line to 195 kbar. *Journal of Applied Physics*, 46(6):2774–2780, 1975.

[148] HK Mao. *Simple molecular systems at very high density*. Plenum Press, New York, 1989.

[149] N Sata, G Shen, ML Rivers, and SR Sutton. Pressure-volume equation of state of the high-pressure B2 phase of NaCl. *Physical Review B*, 65(10):104114, 2002.

[150] L Dubrovinsky, N Dubrovinskaia, S Saxena, and T LiBehan. X-ray diffraction under non-hydrostatic conditions in experiments with diamond anvil cell: wüstite (FeO) as an example. *Materials Science and Engineering: A*, 288(2):187–190, 2000.

[151] H Kuzmany, R Pfeiffer, M Hulman, and C Kramberger. Raman spectroscopy of fullerenes and fullerene–nanotube composites. *Philosophical Transactions of the Royal Society of London A: Mathematical, Physical and Engineering Sciences*, 362(1824):2375–2406, 2004.

[152] H Nakai, T Ebihara, S Tsutsui, M Mizumaki, N Kawamura, S Michimura, T Inami, T Nakamura, et al. Temperature and magnetic field dependent Yb valence in $YbRh_2Si_2$ observed by X-ray absorption spectroscopy. *Journal of the Physical Society of Japan*, 82(12):124712, 2013.

[153] V Svitlyk, W Hermes, B Chevalier, SF Matar, E Gaudin, D Voßwinkel, D Chernyshov, et al. Change of the cerium valence with temperature–structure and chemical bonding of HT-CeRhGe. *Solid State Sciences*, 21:6–10, 2013.

[154] Y Zhang, AA Popov, and L Dunsch. Endohedral metal or a fullerene cage based oxidation? redox duality of nitride clusterfullerenes $Ce_xM_{3-x}N@C_{78-88}$ (x= 1, 2; M= Sc and Y) dictated by the encaged metals and the carbon cage size. *Nanoscale*, 6(2):1038–1048, 2014.

[155] T Wågberg, P Launois, R Moret, HJ Huang, SH Yang, IL Li, and ZK Tang. Study by X-ray diffraction and raman spectroscopy of a $Dy@C_{82}$ single crystal. *The European Physical Journal B-Condensed Matter and Complex Systems*, 35(3):371–375, 2003.

[156] H Giefers, F Nessel, SI Györy, M Strecker, G Wortmann, YS Grushko, EG Alekseev, and VS Kozlov. Gd–LIII EXAFS study of structural and dynamic properties of $Gd@C_{82}$ between 10 and 300 k. *Carbon*, 37(5):721–725, 1999.

[157] L Song, W Ma, Y Ren, W Zhou, S Xie, P Tan, and L Sun. Temperature dependence of Raman spectra in single-walled carbon nanotube rings. *Applied Physics Letters*, 92(12):121905, 2008.

[158] H Herchen and M A Cappelli. First-order Raman spectrum of diamond at high temperatures. *Physical Review B*, 43(14):11740, 1991.

[159] D Yamashita, Y Takahashi, T Asano, and S Noda. Raman shift and strain effect in high-q photonic crystal silicon nanocavity. *Optics Express*, 23(4):3951–3959, 2015.

[160] S Mann and VK Jindal. Blue and red shifted temperature dependence of implicit phonon shifts in graphene. *Materials Research Express*, 4(7):075038, 2017.

[161] BG Burke, J Chan, KA Williams, J Ge, C Shu, W Fu, HC Dorn, JG Kushmerick, et al. Investigation of $Gd_3N@C_{2n}$ ($40 \leqslant n \leqslant 44$) family by raman and inelastic electron tunneling spectroscopy. *Physical Review B*, 81(11):115423, 2010.

[162] SD Pandey, J Singh, K Samanta, ND Sharma, and AK Bandyopadhyay. Temperature dependent variations of phonon interactions in nanocrystalline cerium oxide. *Journal of Nanomaterials*, 16(1):154, 2015.

[163] MS Liu, LA Bursill, S Prawer, and KW Nugent. Temperature dependence of Raman scattering in single crystal GaN films. *Applied Physics Letters*, 74(21):3125–3127, 1999.

[164] MS Liu, LA Bursill, and S Prawer. Temperature dependence of the first-order Raman phonon line of diamond. *Physical Review B*, 61(5):3391–3395, 2000.

[165] M Lazzeri, S Piscanec, F Mauri, AC Ferrari, and Robertson J. Phonon linewidths and electron-phonon coupling in graphite and nanotubes. *Physical Review B*, 73:155426, 2006.

[166] N Bonini, M Lazzeri, N Marzari, and F Mauri. Phonon anharmonicities in graphite and graphene. *Physical Review Letters*, 99:176802, 2008.

[167] C Cong and T Yu. Enhanced ultra-low-frequency interlayer shear modes in folded graphene layers. *Nature communications*, 5, 2014.

[168] AC Ferrari. Raman spectroscopy of graphene and graphite: disorder, electron–phonon coupling, doping and nonadiabatic effects. *Solid State Communications*, 143(1-2):47–57, 2007.

[169] PH Tan, WP Han, WJ Zhao, ZH Wu, K Chang, H Wang, YF Wang, N Bonini, N Marzari, N Pugno, et al. The shear mode of multilayer graphene. *Nature Materials*, 11(4):294, 2012.

[170] I Calizo, S Ghosh, W Bao, F Miao, CN Lau, and AA Balandin. Raman nanometrology of graphene: Temperature and substrate effects. *Solid State Communications*, 149(27-28):1132–1135, 2009.

[171] GSR Raju, E Pavitra, and JS Yu. Pechini synthesis of lanthanide (Eu^{3+}/Tb^{3+} or Dy^{3+}) ions activated $BaGd_2O_4$ nanostructured phosphors: an approach for tunable emissions. *Physical Chemistry Chemical Physics*, 16(34):18124–18140, 2014.

[172] YQ Jia. Crystal radii and effective ionic radii of the rare earth ions. *Journal of Solid State Chemistry*, 95(1):184–187, 1991.

[173] BP Sobolev. *The Rare Earth Trifluorides: The high temperature chemistry of the rare earth trifluorides*, volume 124. Institut d'Estudis Catalans, 2000.

[174] FX Alvarez and D Jou. Size and frequency dependence of effective thermal conductivity in nanosystems. *Journal of Applied Physics*, 103(9):094321, 2008.

[175] MR Abel, S Graham, JR Serrano, SP Kearney, and LM Phinney. Raman thermometry of polysilicon microelectro-mechanical systems in the presence of an evolving stress. *Journal of Heat Transfer*, 129(3):329–334, 2007.

[176] G Fugallo, A Cepellotti, L Paulatto, M Lazzeri, N Marzari, and F Mauri. Thermal conductivity of graphene and graphite: collective excitations and mean free paths. *Nano Letters*, 14(11):6109–6114, 2014.

[177] KT Regner, DP Sellan, Z Su, CH Amon, AJH McGaughey, and JA Malen. Broadband phonon mean free path contributions to thermal conductivity measured using frequency domain thermoreflectance. *Nature Communication*, 4:1640, 2013.

[178] G Xie, Y Guo, X Wei, K Zhang, L Sun, J Zhong, G Zhang, and YW Zhang. Phonon mean free path spectrum and thermal conductivity for $Si_{1-x}Ge_x$ nanowires. *Applied Physics Letters*, 104(23):233901, 2014.

[179] TY Kim, CH Park, and N Marzari. The electronic thermal conductivity of graphene. *Nano Letters*, 16(4):2439–2443, 2016.

[180] NH Tea, RC Yu, MB Salamon, DC Lorents, R Malhotra, and RS Ruoff. Thermal conductivity of C_{60} and C_{70} crystals. *Applied Physics A*, 56(3):219–225, 1993.

[181] X Wang, CD Liman, ND Treat, ML Chabinyc, and DG Cahill. Ultralow thermal conductivity of fullerene derivatives. *Physical Review B*, 88(7):075310, 2013.

[182] AA Balandin. Thermal properties of graphene and nanostructured carbon materials. *Nature Materials*, 10(8):569, 2011.

[183] B Chase, N Herron, and E Holler. Vibrational spectroscopy of fullerenes (C_{60} and C_{70}). temperature dependant studies. *The Journal of Physical Chemistry*, 96(11):4262–4266, 1992.

[184] GBM Vaughan, PA Heiney, DE Cox, AR McGhie, DR Jones, RM Strongin, MA Cichy, and AB Smith III. The orientational phase transition in

solid buckminsterfullerene epoxide ($C_{60}O$). *Chemical Physics*, 168(1):185–193, 1992.

[185] S Lebedkin, A Gromov, S Giesa, R Gleiter, B Renker, H Rietschel, and W Krätschmer. Raman scattering study of C_{120}, a C_{60} dimer. *Chemical Physics Letters*, 285(3):210–215, 1998.

[186] AV Talyzin, A Dzwilewski, and T Wågberg. Temperature dependence of C_{60} raman spectra up to 840 K. *Solid State Communications*, 140(3-4):178–181, 2006.

[187] I Calizo, AA Balandin, W Bao, F Miao, and CN Lau. Temperature dependence of the Raman spectra of graphene and graphene multilayers. *Nano Letters*, 7(9):2645–2649, 2007.

[188] P Tan, Y Deng, Q Zhao, and W Cheng. The intrinsic temperature effect of the Raman spectra of graphite. *Applied Physics Letters*, 74(13):1818–1820, 1999.

[189] M Menon and KR Subbaswamy. Optimized structures of $C_{60}O$ and $C_{60}O_2$ calculated by a damped molecular dynamics optimization scheme. *Chemical Physics Letters*, 201(1-4):321–325, 1993.

[190] F Gugenberger, R Heid, C Meingast, P Adelmann, M Braun, H Wühl, M Haluska, and H Kuzmany. Glass transition in single-crystal $C_{60}O$ studied by high-resolution dilatometry. *Physical Review Letters*, 69(26):3774, 1992.

[191] AT Pugachev, NP Churakova, NI Gorbenko, Kh Saadli, and ES Syrkin. Thermal expansion of thin C_{60} films. *Journal of Experimental and Theoretical Physics*, 87(5):1014–1018, 1998.

[192] AT Pugachev, NP Churakova, and NI Gorbenko. Dilatometric size effect in thin C_{60} films. *Low Temperature Physics*, 23(8):642–643, 1997.

[193] PK Schelling and P Keblinski. Thermal expansion of carbon structures. *Physical Review B*, 68(3):035425, 2003.

[194] NA Aksenova, AP Isakina, AI Prokhvatilov, and MA Strzhemechny. Analysis of thermodynamic properties of fullerite C_{60}. *Low Temperature Physics*, 25(8):724–731, 1999.

[195] F Diederich, R Ettl, Y Rubin, RL Whetten, R Beck, M Alvarez, S Anz, Dilip Sensharma, F Wudl, et al. The higher fullerenes: isolation and characterization of C_{76}, C_{84}, C_{90}, C_{94}, and $C_{70}O$, an oxide of D_{5h}-C_{70}. *Science*, 252(5005):548–551, 1991.

[196] RA Jishi, MS Dresselhaus, G Dresselhaus, KA Wang, P Zhou, AM Rao, and PC Eklund. Vibrational mode frequencies in C_{70}. *Chemical Physics Letters*, 206(1-4):187–192, 1993.

[197] AJ Bullen, KE OHara, DG Cahill, O Monteiro, and A von Keudell. Thermal conductivity of amorphous carbon thin films. *Journal of Applied Physics*, 88(11):6317–6320, 2000.

[198] JH Seol, I Jo, AL Moore, L Lindsay, ZH Aitken, MT Pettes, X Li, Z Yao, R Huang, et al. Two-dimensional phonon transport in supported graphene. *Science*, 328(5975):213–216, 2010.

[199] SK Lee, M Buerkle, R Yamada, Y Asai, and H Tada. Thermoelectricity at the molecular scale: a large seebeck effect in endohedral metallofullerenes. *Nanoscale*, 7(48):20497–20502, 2015.

[200] SJ Jeon, D Kim, SK Kim, and IC Jeon. High-pressure Raman study of fullerite c_{60}. *Journal of Raman spectroscopy*, 23(5):311–313, 1992.

[201] M Hanfland, H Beister, and K Syassen. Graphite under pressure: Equation of state and first-order Raman modes. *Physical Review B*, 39(17):12598, 1989.

[202] AB Cairns and AL Goodwin. Negative linear compressibility. *Physical Chemistry Chemical Physics*, 17(32):20449–20465, 2015.

[203] B Sundqvist. The structures and properties of C_{60} under pressure. *Physica B: Condensed Matter*, 265(1-4):208–213, 1999.

[204] HA Ludwig, WH Fietz, FW Hornung, K Grube, B Wagner, and GJ Burkhart. C_{60} under pressure-bulk modulus and equation of state. *Zeitschrift für Physik B Condensed Matter*, 96(2):179–183, 1994.

[205] A Lundin and B Sundqvist. Compressibility of C_{60} in the temperature range 150–335 K up to a pressure of 1 GPa. *Physical Review B*, 53(13):8329, 1996.

[206] MH Manghnani, WS Brower, and HS Parker. Anomalous elastic behavior in Cu_2O under pressure. *Physica Status Solidi (a)*, 25(1):69–76, 1974.

[207] TR Ravindran, Akhilesh K Arora, and TA Mary. High pressure behavior of ZrW_2O_8: Grüneisen parameter and thermal properties. *Physical Review Letters*, 84(17):3879, 2000.

[208] KP Meletov, J Arvanitidis, S Assimopoulos, GA Kourouklis, and B Sundqvist. Pressure-induced transformations and optical properties of the two-dimensional tetragonal polymer of C_{60} at pressures up to 30 GPa. *Journal of Experimental and Theoretical Physics*, 95(4):736–747, 2002.

[209] O Andersson, A Soldatov, and B Sundqvist. Thermal conductivity of C_{60} at pressures up to 1 GPa and temperatures in the 50–300 K range. *Physical Review B*, 54(5):3093, 1996.

[210] JC Klöckner, R Siebler, JC Cuevas, and F Pauly. Thermal conductance and thermoelectric figure of merit of C_{60}-based single-molecule junctions: electrons, phonons, and photons. *Physical Review B*, 95(24):245404, 2017.

[211] N Almutlaq, Q Al-Galiby, S Bailey, and CJ Lambert. Identification of a positive-seebeck-coefficient exohedral fullerene. *Nanoscale*, 8(28):13597–13602, 2016.